Micro/Nanomechanical Sensing for Monitoring Biological Processes

by

Keren Jiang

A thesis submitted in partial fulfillment of the requirements for the degree of

Doctor of Philosophy

In
Chemical Engineering

Department of Chemical and Materials Engineering
University of Alberta

Abstract

Developing miniature instrumentation for biosensing has attracted an extensive interest due to the demand for selective and sensitive detection of multiple targets at extremely low concentrations with exceedingly small sample volumes. Micro/nano mechanical sensors, such as microcantilevers (MCL), are highly sensitive to mechanical interactions such as force, stress and mass change. Mechanical forces originated from physical and chemical interactions are fundamental in biological process from cellular to molecular scale. MCL sensors with comparable size with cells and biomacromolecules, are sensitive, rapid and reliable transducer platforms for biosensing applications. However, the challenge in developing biosensors lies the specificity and reproducibility. Thus, we focus on optimizing the interfaces of the micro/nanomechanical sensors and exploring new detection methodologies, aiming to reduce non-specific surface binding, improve intrinsic sensor performance and monitor biological process in real-time. By monitoring the micro/nanomechanical property variations using microelectromechanical (MEMs) devices, the thermodynamic and nanomechanical properties of biological processes can be determined.

In this thesis, we have developed MCL-based biosensors for various applications including whole cell recognition, protein folding detection, neurotransmitter monitoring and DNA melting measurement. With optimized sensing layers, the MCL-based sensors are capable to distinguish targets with varied dimensions from micrometers to sub-nanometers. Surface stress induced via cell binding, conformational change, and molecular displacement are observed and quantified. With a microfluidic cantilever, the mechanical property of biofluid can be monitored with confined

sample volume. Other sensor platforms such as electrical impedance spectroscopy (EIS) and surface plasmon resonance (SPR) are also used for sensing layer optimization and validation.

We reviewed and compared MEMs systems which allow measurement of stress/force, mass change/displacement for fluidic samples. We have developed pathogen sensors with a limit of detection (LOD) of 1 cell per μL with high selectivity based on antimicrobial peptides (AMPs) functionalized micromechanical devices. The protonation/deprotonation induced protein conformational change with different pH condition is also analyzed using MCL sensor. A conjugated polymer system is designed for dopamine detection with LOD down to the picomolar range and this system is capable to recognized dopamine from coexisting molecules and structural analogs. We also employed a microfluidic cantilever for measuring the melting temperature of DNA samples and the viscosity change with the melting process. This study provides a novel approach for monitoring micromechanical properties change of biological interactions in real-time with confined sample volume. By monitoring the mechanical property change, the thermodynamic and micromechanical variation of the DNA melting process has been analyzed.

Mechanical interactions as one of the fundamental physical properties of biology can be quantified with MCL sensor platforms. Interfacial optimization and novel sensor design such as hollow channel microfluidic cantilevers can improve the selectivity and sensitivity of the sensors and providing further understanding of the micromechanical properties involved in biological processes. Future work will be continued on continued understanding of analyte-sensor interactions; improving the selectivity of the sensor in complexed samples; increasing the sensor stability under harsh sensing environment and minimizing the sensor volume.

Preface

This thesis is an original work by Keren Jiang (Jiang, K.) under the supervision of Dr. Thomas Thundat (Thundat, T.).

Chapter 3 of this thesis has been published as Azmi, S., Jiang, K., Stiles, M., Thundat, T., and Kaur, K., "Detection of *Listeria monocytogenes* with short peptide fragments from class IIa bacteriocins as recognition elements", *ACS Combinatorial Science*, **2015**, 17(3), 156-163. I was responsible for the data collection and analysis as well as manuscript composition. Azmi, S. also contributed in data collection, analysis and manuscript composition. Stiles, M. assisted with sample preparation. Thundat, T., and Kaur, K. were the supervisory author and were involved with research design and manuscript composition.

Chapter 4 of this thesis has been published as Thakur, G., Jiang, K., Lee, D., Prashanthi, K., Kim, S., Thundat, T. "Investigation of pH-induced protein conformation changes by nanomechanical deflection", *Langmuir*, **2014**, 30(8), 2109-2116. Thakur, G. and I collected and analyzed the data and composed the manuscript. Lee, D., Prashanthi, K. and Kim, S. helped with experimental design and results discussion. Thundat, T. was the supervisory author and was involved with research design and manuscript composition.

Chapter 5 of this thesis has been published as Jiang, K., Wang, Y., Thakur, G., Kotsuchibashi, Y., Naicker, S., Narain, R., Thundat. T., "Rapid and Highly Sensitive Detection of Dopamine Using Conjugated Oxaborole-Based Polymer and Glycopolymer Systems", ACS *Applied Materials and Interfaces*, **2017**, 9(18), 15225-15231. I was responsible for data collection and analysis as well as

the manuscript composition. Wang, Y. assisted with sample preparation and experimental design. Thakur, G. and Kotsuchibashi, Y. and Naicker, S. helped with results discussion. Narain, R. and Thundat. T. were supervisory author and were involved in research design and manuscript composition.

Chapter 6 of this thesis is being prepared for publishing as Jiang, K., Phani, A., Thomas, J., Khan, F., Thundat, T., "Nanomechanical Manifestation of DNA Melting in a Microfluidic Cantilever". I was responsible for experimental design, data collection and analysis. Phani, A. also contributed in analyzing the data. Thomas, J. assisted with data collection and sample preparation. Khan, F. assisted with experimental setup and device fabrication. Thundat. T. was supervisory author and were involved in research design and manuscript composition. All authors were involved in manuscript composition.

"Stay Hungry. Stay Foolish."

--Steve Jobs

DEDICATED TO

MY DEAR FRIEND DR. YINAN WANG (1986-2017)

Acknowledgements

First of all, I would like to express my sincere thanks to my supervisor, Dr. Thomas Thundat, for giving me an opportunity to explore various topics in material sciences and nanotechnology at University of Alberta. Without his continuous encouragements, guidance, and suggestions, I could not have pursued this degree. His solid fundamental knowledge in natural science and creative ideas for innovations have inspired me chasing and exploring the fundamentals and applications of our theories and techniques. Dr. Thundat is also an outstanding role model in working attitude and a great mentor in the philosophy of life. It is my honor to spend this journey with Dr. Thundat and learn from him.

My heartfelt appreciation goes to Dr. Kamaljit Kaur, who guided and supported me to initiate my research into the new field of biochemistry and biosensing. Whenever I ran into confusions or difficulties, she was always there. Without her support, my research would not have been possible.

I also appreciate Dr. Ravin Narain who introduced smart polymer and biocompatible materials to me. I thank him for his knowledge and ideas in materials science, and deep discussions with me in the smart polymer sensing project.

I would also thank Dr. Hyun-Joong Chung, Dr. Vinay Prasad and the other members of my supervisory committee for viewing my thesis and giving me comments and suggestions. Also, your inspiring work gives me hints and ideas for my research.

I would also like to express my gratitude to previous lab members, collaborators who helped me with my work: Dr. Garima Thakur, Dr. Sarfuddin Azmi, Dr. Sangwan Kim, Dr. Donkyu Lee, and Dr. Yohei Kotsuchibashi.

I am grateful to my collaborators, lab mates and also great friends, especially Dr. Selvaraj Naicker, Dr. Zhi Li, Dr. Faheem Khan, Dr. Hashem Etayesh, Dr. Parmiss Shaibani, Dr. Amir Sohrabi, Dr. Ankur Goswami, Dr. Javix Thomas, Dr. Arindam Phani and Mr. Jun Liu, for all your knowledge and collaboration helping me finish my research.

I would thank nanoFAB stuff members and facilities for helping fabrication and characterization. My gratitude also goes to Dr. Vishwa Somayaji from Faculty of Pharmacy and Pharmacutical Sciences and Ms. Ni Yang from Department of Chemical and Materials Engineering for assisting with sample characterizations.

Many thanks to my friends in Edmonton, especially Dr. Yinan Wang, Mr. Sheng Tian, Dr. Tianfu Yang, Mr. Tianxin Bao, Mr. Tianbo Liu and his wife Ms. Shuning Li, and Miss Jing Ji. Friends in other parts of the world, especially Mr. Liudong Gu, Dr. Tengfei Miao, Dr. Kai He, Dr. Hui Li, Dr. Linda Wu, Dr. Chang Guo, Dr. Yinyan Tangsun, Dr. Dameng Guo, Mr. Chonghui Li and Ms. Yingzhi Yue. Thank you for all your support and company.

I would like to thank Department of Chemical and Materials Engineering, Faculty of Pharmacy and Pharmacutical Sciences and Faculty of Graduate Studies and Research for providing me the opportunity persueing my PhD degree. Also, I would thank financial support from Canada Excellent Research Chair (CERC) program, Natural Sciences and Engineering Research Council (NSERC), and Alberta Innovates Technology Futures (AITF) Graduate Student Scholarship.

Last, but most importantly, I would like to thank my family and my girlfriend Miss Tianyi Jin, for their love, understanding, encouragements, support, care and sacrifice in the past 30 years/15years in my life.

Table of Contents

List of Figures

List of Publications

1. Jiang, K., Wang, Y., Thakur, G., Kotsuchibashi, Y., Naicker, S., Narain, R., Thundat. T., Rapid and Highly Sensitive Detection of Dopamine Using Conjugated Oxaborole-Based Polymer and Glycopolymer Systems, *ACS Applied Materials and Interfaces*, **2017**, 9(18), 15225-15231.

2. Li, Z., Ahadi, K., Jiang, K., Behzad, A., Li, P., Anyia, A., Cadien, K., Thundat, T., Freestanding hierarchical porous carbon film derived from hybrid nanocellulose for high-power supercapacitors, *Nano Res*. **2017**, 10(5), 1847-1860.

3. Li, Z., Liu, J., Jiang, K., Thundat, T., Carbonized nanocellulose sustainably boosts the performance of activated carbon in ionic liquid supercapacitors, *Nano Energy*, **2016**, 25, 161-169.

4. Shaibani, P., Jiang, K., Haghighat, G., Hassanpoufard, M., Etayash, H., Naicker, S., Thundat, T., The detection of *Escherichia coli (E. coli)* with the pH sensitive hydrogel nanofiber-light addressable potentiometric sensor (NF-LAPS)", *Sensors and Actuators B: Chemical*, **2016**, 226, 176-183.

5. Jiang, K., Etayash, H., Azmi, S., Naicker, S., Hassanpourfard, M., Shaibani, P., Thakur, G., Kaur, K., Thundat, T., Rapid label-free detection of *E. coli* using antimicrobial peptide assisted impedance spectroscopy, *Analytical Methods*, **2015**, 7 (23), 9744-9748. **(Cover Feature)**

6. Etayash, H., Jiang, K., Azmi, S., Thundat, T., Kaur, K., Real-time detection of breast cancer cells using peptide-functionalized microcantilever arrays, *Scietific Reports*, **2015**, 5, 13967-13967.

7. Jiang, K., Etayash, H., Azmi, S., Thakur, G., Naicker, S., Kaur, K., Thundat, T., Label-Free Rapid Detection of Pathogens with Antimicrobial Peptide Assisted Impedance Spectrometry, *MRS Proceedings,* **2015**, 1793, mrss15-2095895.

8. Azmi, S., Jiang, K., Stiles, M., Thundat, T., Kaur, K., Detection of Listeria monocytogenes with short peptide fragments from class IIa bacteriocins as recognition elements, *ACS Combinatorial Science,* **2015**, 17(3), 156-163. **(Cover Feature)**

9. Thakur, G., Jiang, K., Lee, D., Prashanthi, K., Kim, S., Thundat, T. Investigation of pH-induced protein conformation changes by nanomechanical deflection, *Langmuir*, **2014**, 30(8), 2109-2116.

10. Etayash, H.R., Jiang, K., Thundat, T., Kaur, K., Impedimetric Detection of Pathogenic Gram-Positive Bacteria Using an Antimicrobial Peptide from Class IIa Bacteriocins, *Analytical Chemistry*, **2014**, 86(3), 1693-1700.

Chapter 1. Introduction

The biosensor has been used by humans for a long time. The first biosensors were small animals, whose behavior was observed as a sign of climate change or earthquakes or, in the case of a canary in a coalmine, to warn of the existence of toxic gas. Many of today's biosensor applications are similar; they use bioagents to respond to substances or a physical characteristic like vibration or electrical charges at much lower concentrations than humans can sense.

A biosensor is an analytical device that combines a biological component with a physicochemical detector.[1] There are three major elements for a biosensor (**Figure 1.1**). The first is a layer of biomolecules which can bind or interact with sample molecules and which serves as the recognition element. This sensing layer defines the specificity of the sensor. These sensing layers can respond specifically to targets ranging from peptides and enzymes up to whole cells and microorganisms.[2] The second element is a physical transducer, a solid-state device which is able to detect the interaction between the sensing layer and the sample molecules. The biological interaction is then transduced into a convenient electronic signal for further processing. The third element is a biosensor reader device which usually processes the signal from the sensing layer and transducer and presents it in a user-friendly way. The readers are usually custom-designed and manufactured to suit the different working principles of biosensors.[3,4]

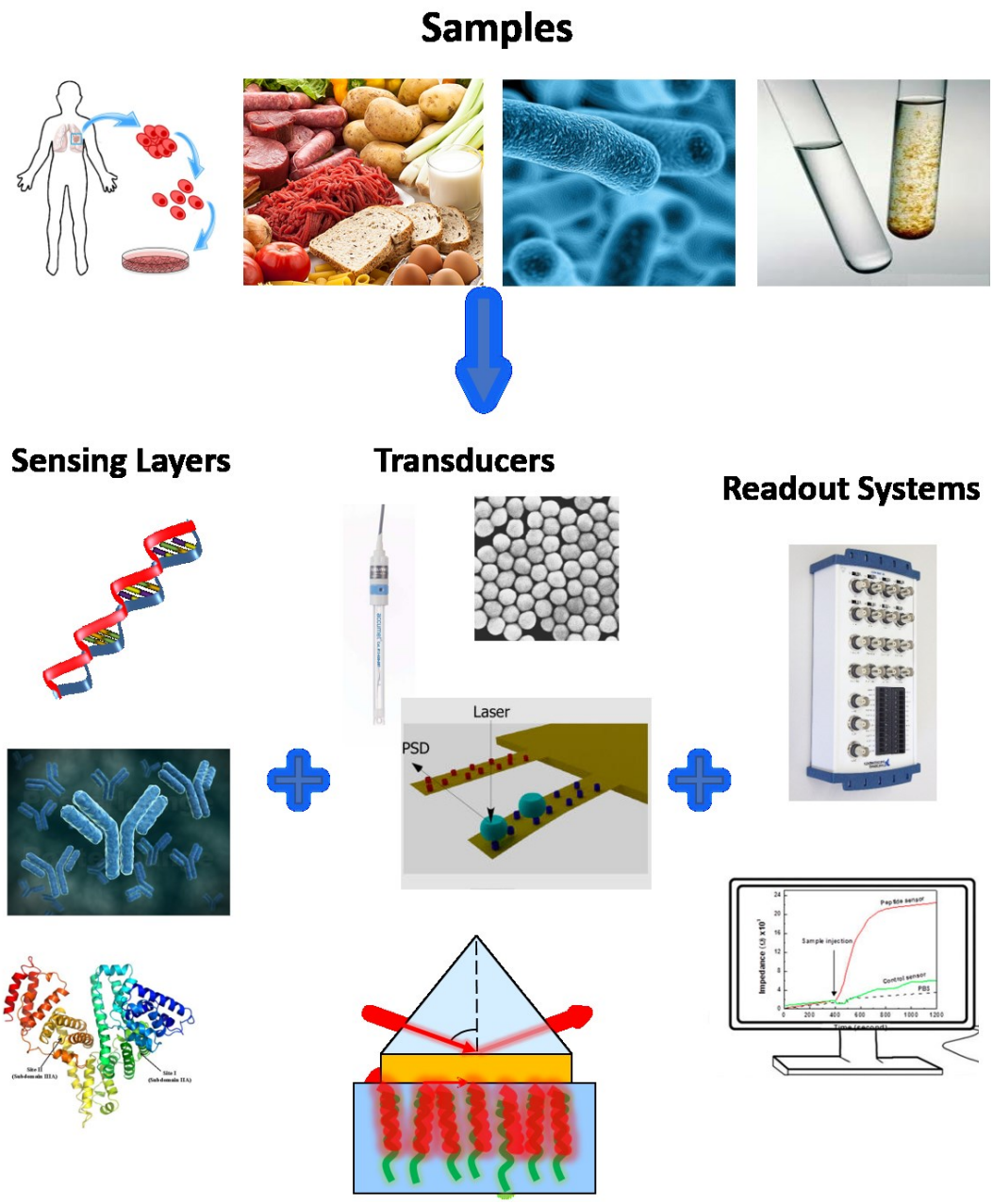

Figure 1.1 Schemes of biosensors: an analytical device combines a biological component with a physicochemical detector. There are three major elements of a biosensor: a sensing layer, a physical transducer and a readout system.

There have been urgent requirements to develop new types of sensors with high specificity, sensitivity, efficiency and reliability, among which specificity is the most important. In order to achieve novel sensor design and development, we are committed to understanding the history of biosensor development, the three components of biosensor systems, and the current limits of biosensors. In this way, novel biosensors with specified targets will be designed and developed. Moreover, the understanding of the interfaces between biosensor components will lead to a renovative biosensing revolution.

1.1 Biosensing: Background, Development and Overview

Biosensor research is a rapidly progressing field which provides devices for the detection of various molecules with lower concentrations and minimized volume. Biosensors are used in health care, medical diagnostics, environmental screening, process control in industry, harmful substances detection for military and regulatory inspection, and most importantly, in fundamental research in the life sciences. An ideal biosensor should be real-time, nondestructive to samples and able to perform tasks from single molecule detection to high concentrations of molecules. It should also identify the composition of a sample. To achieve this goal, the sensor should be reliable, portable, relatively cheap and user-friendly. Biosensor research is a highly interdisciplinary field which requires physics and engineering for hardware developing, and chemistry and biology for sensor surface functionalization, label synthesis and biotechnological processes.[5]

Since the first classical biosensor from Clark and Lyons in 1962 (an amperometric sensor detecting glucose level in blood),[6] many different biosensors have been developed.

However, only a limited number of the sensors meet the requirements to be considered reliable commercial sensors for applications outside research labs. Traditional sensors, like electrochemical sensors, require well-trained personnel to operate and have limited working range and selectivity. One attractive group of optical biosensors is based on the phenomenon of surface plasmon resonance (SPR). This technique is based on the electron waves (surface plasmon) created on the metal layer coated (commonly gold coated) on a high refractive index glass surface after the absorption of laser light.[7] However, SPR occurs only at a specific angle determined by incident light wavelength, which restricts the types of targets it can detect and working range. As a result, there is a need for SPR-based sensors with higher specificity and limit of detection (LOD).

A biosensor is defined as a device that uses biological components to detect the presence or activity of analytes. The sensitive element is a biologically derived material or biomimetic component that reacts with the analytes under detection conditions. The sensitive element can also be created using biological engineering. This biological sensing layer, which defines the specificity of the sensor, can bind or interact with analyte molecules and act as the recognition element. The physical transducer detects the interaction between the sensing layer and the analyte and then transfers the biological signals into conventional physical signals, which are either mechanical, electrical or optical, for example, the fluorescence signal from dyes, an electric signal from molecular charges or refractive index changes from the surface adsorption of analytes onto sensor interfaces. The physical transducer determines the sensitivity of the sensor system. The readout systems need to be perfectly matched with the physical transducers. For example, fluorescence microscopy or fluorescence spectroscopy is used for observing and

quantifying the labeled analytes, giving two different aspects of information. The readout system converts the physical (e.g. mechanical, optical, electrical) signals from transducers into readable information such as color change, voltage/current variation or most commonly, the digital signal. Usually, a suitable readout system can improve the data acquisition process and the user's experience with the sensors.

As mentioned previously, a biosensing system is a combination of three elements. Integrating them and creating compatible and efficient interfaces between these elements is one key factor for success in designing and developing biosensors. With the development of semiconductor industry, the micro/nanoelectromechanical (MEM/NEM) sensor has attracted much attention in recent decades. The LOD has been improved or enhanced to sub pico molar (pM) or even near femtor molar (fM) or parts per trillion (ppt) range,[8] which is lower than most of the bio targets' physiology level. However, the selectivity or recognition of specific targets from coexisting molecules/bio-species remains as one of the biggest challenges.

There are two major types of biosensors, label-free and labeled (**Figure 1.2**). They are classified based on the detection principle: label-free biosensors detect original and unmodified molecules and can be used for on-line monitoring or fast-scan detection. Most of the molecules are easier to detect when first tagged with a molecular label. The presence of the label acts as an indicator for the presence of the molecule, such as the fluorescent labels attached to molecules in fluorescence microscopy. One obvious disadvantage of this method is that the target molecules are chemically modified before investigation. With labeled detection, LOD of 1 fM has been achieved with the assistance of MEMs sensors.[9,10]

However, labeling will interfere with the function of the molecules and labeling is time-consuming and expensive.[5] Thus, in many cases, labeling should be avoided.

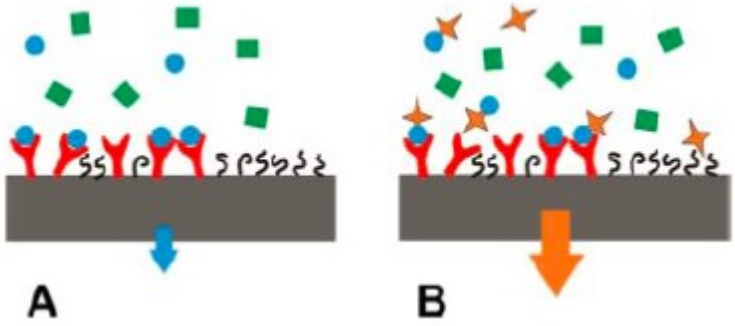

Figure 1.2 Scheme of biosensing principle. A biomolecular layer of receptor molecules (red) bind to the analyte (blue dots) but does not respond to the other molecules (green). A protection layer (black lines) prevents the unspecific absorption to the transducer surface (gray). A. Label-free detection. B. A label is attached to the target analyte. Figure from Ref 5.

Our first goal is to advance the development of real-time, label-free biosensors with high sensitivity, selectivity and low cost for applications in biomedical diagnostics and pathogen detection. We aim to study such devices by devising new biomolecules for the sensing layer design and integration. Moreover, we aim to understand the mechanisms of the device development and the interfaces between elements of biosensor systems. Another aim is to provide technological innovation and develop sensors with the potential to be commercialized or applied in clinical use.

1.2 Bioactive sensing layers

In a biosensing system, the bioactive sensing layer is designed to interact with specifically with the target analyte and produce a reliable and measurable effect to which the physical transducer will respond. The key requirement of the bioactive sensing layer is high selectivity, as the analytes are usually accompanied by coexisting compounds, structural analogs, and other interfering factors in their natural/physiology environment. The sensing layer can consist of a wide range of bio receptors involving: antibody/antigen, nucleic acids/DNA/RNA, enzymes, cells, peptides, or biomimetic/biocompatible materials.

1.2.1 Antibody-based sensing layers

The antibody-based sensing layer emerged from immunosensors utilizes antibody-antigen specific binding. The key-lock fitting nature of the antibody-antigen interaction leads to the high specificity (**Figure1.3**). In a traditional immunosensor, the antibody-antigen binding triggers a label such as fluorophore or radioisotopes to generate a signal. In novel MEMs or optical sensors,[11–13] antibodies are usually pre-functionalized onto the transducer surfaces and mechanical, electrical or optical signals are generated with the specific binding, without the requirement of labeling. The antibody-based sensing layers have limitations such as: the binding is irreversible and highly dependent on the surrounding conditions. In addition, antibodies usually a have short shelf life which makes them suitable mostly for laboratory scale research.

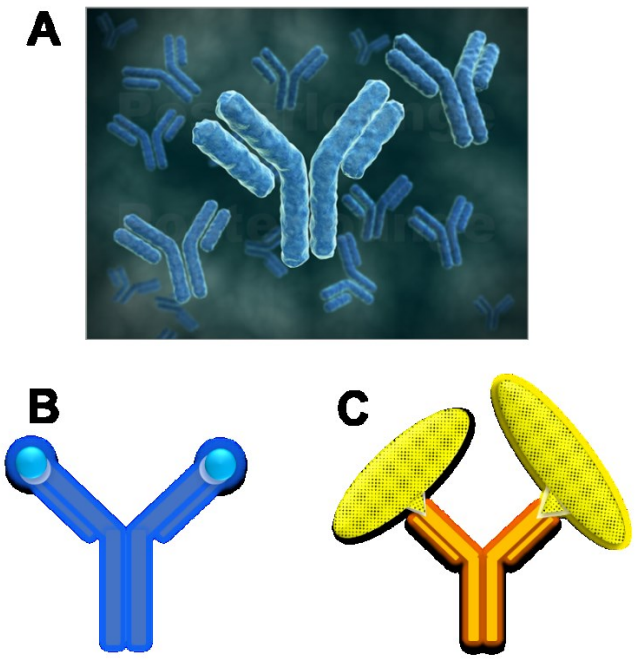

Figure 1.3 (A) An illusion of antibodies, and schemes showing specific antibody binding (B) to antigen directly; (C) to an antigen on a larger target (e.g. a cell).

1.2.2 Enzyme-based sensing layers

Enzymes are another class of bioreceptors with very high specificity.[14] There are several possible mechanisms by which enzymes can be used to recognize analytes: 1) converting the analyte into a detectable product; 2) detecting enzyme activation/inhibition by the analyte; 3) monitoring enzyme properties caused by interacting with analytes (**Figure 1.4).** Enzymes, as biocatalysts, can easily be used to detect substrates, products, inhibitors and so on through different transduction methods. Enzymes are not consumed during the detection process, so that the enzyme sensor can be used continuously. However, due to the catalytic reactions, enzyme sensors are usually destructive to analytes. Also, similar to the antibody-based sensing layer, enzyme layer stability and lifetime is also highly

depended on its surroundings. The most widely used enzyme sensor is enzyme-linked immunosorbent assay (ELISA).[15,16] Enzymes have also been used on MEMs sensors[17], nanoparticles[18] and electrical sensors[19,20] for chemical and biological targets.

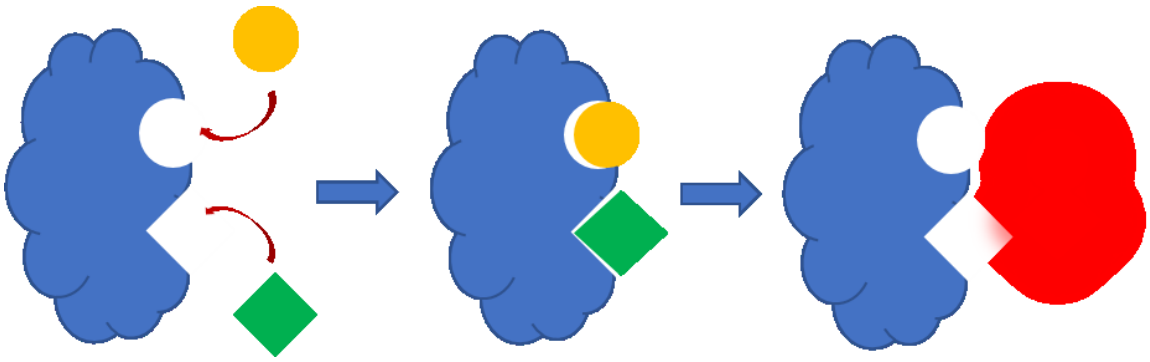

Figure 1.4 A scheme illustrating a typical enzymatic reaction: the enzyme converts the analytes into detectable products.

1.2.3 Peptide-based sensing layers

Antibodies and enzymes have significant impact on biosensing. But their high cost and low reliability at harsh environmental conditions limit their wide spread applications as sensors. In contrast to these molecules, antimicrobial peptides (AMPs) are intrinsically more stable in harsh environmental conditions, easier to synthesize, and exhibit a broadband of activities and affinities against wide range of Gram-positive and Gram-negative strains of bacteria.[21] Recent studies have shown AMPs as molecular recognition elements in biosensor platforms and demonstrated the ability of naturally occurring AMPs to serve as robust biosensing elements.[22,23]

Bacteriocin is one group of AMPs which are proteinaceous toxins produced by bacteria to inhibit the growth of similar or closely related bacterial strains.[24] Bacteriocins were first discovered by A. Gratia in 1925.[25] Bacteriocin can be classified according to their origin. Bacteriocins from Gram-positive bacteria include Class I, Class II, Class III and Class IV bacteriocins. Those from Gram-negative bacteria include Microcins, Colicin-like bacteriocins, and Tailocins. The class II bacteriocins are small (<10 kDa) heat-stable proteins. This class is subdivided into five subclasses. The class IIa bacteriocins (pediocin-like bacteriocins) are the largest subgroup and contain an N-terminal consensus sequence -Tyr-Gly-Asn-Gly-Val-Xaa-Cys across the group. The C-terminal is responsible for the species-specific activity, causing cell-leakage by permeabilizing the target cell wall. Class IIa bacteriocins have a large potential for use in food preservation as well as medical applications, due to their strong anti-listerial activity, and a broad range of activity.[26,27,28] Although the exact mechanism of specificity of class IIa bacteriocins remains a matter of controversy, there is a consensus that they exert their antimicrobial specificity and activity by binding to invariant components of microbial surfaces through specific membrane-located proteins of the mannose phosphotransferase system (man-PTS).[29,30,31] Different expression levels of this mannose receptor on the surface of the bacterial cells from one to another lead to the bacteriocins' various sensitivities and activities.[31]

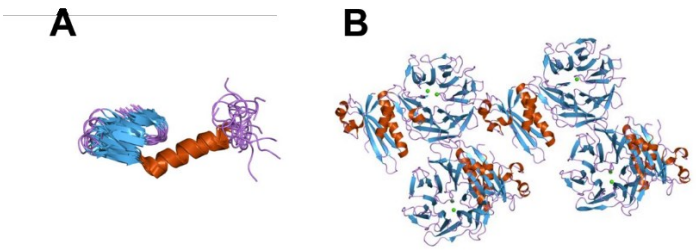

Figure 1.5 Schematics of typical bacteriocins: A) Class II bacteriocin and B) Colicin-like bacteriocin. Figures from Protein Data Base (PDB).

Bacteriocins from Gram-negative strains, such as colicins, are from *E. coli* strains. They are the first studied bacteriocins. Colicin V (ColV) is an 88-amino-acid, linear unmodified AMP.[32] It is a type of bacteriocin produced by *E. coli* which acts against *E. coli* strains by binding to the outer membrane receptors and using them to translocate the cytoplasmic membrane, leading to the depolarization of the membrane, which ultimately kills the cell.[32,33] According to World Health Organization (WHO) guidelines, the value of *E. coli* or thermotolerant coliform bacteria in drinking water is *0 cfu* per 100 mL.[34] The *E. coli* level is commonly used as a water pathogen standard. As a result, it is important to monitor *E. coli* species in the water system, especially in rural area and developing countries.

To sum up, the AMPs are ideal sensing layers for real-time detection of whole cells in solutions. AMPs functionalized sensors are selected for the initial study of this biosensing project. From this platform, other sensing probes and physical transducers combination can be studied and developed.

1.2.4 DNA/nucleic acid-based sensing layers

DNA sensing layers are based on the principle of complementary base pairing: adenine-thymine (A-T) and cytosine-guanine (C-G). DNA carries unique biological information of each bio organism, which makes it highly specified. The sensing probe DNA can be synthesized according to the target DNA sequence, and then labeled and immobilized on the sensor surface. Hybridization will take place when the matching target DNA introduced into the system (**Figure 1.6**). Favored transduction methods include UV-vis spectroscopy, using the 260 nm absorption peak from DNA strains or conjugated DNA with other nanoparticles to enhance the signal.[35] Novel MEMS transducers can increase the sensitivity and detection mismatches down to single base-pair level.[36,37] There have also been studies about using the advantages of DNA and other sensing molecules like enzymes or hydrogels to improve the specificity and efficiency.[38–40] DNA is one of the most intensively-studied sensing molecules. There have also been researchers using biosensors for studying the physicochemical character of DNA.[41]

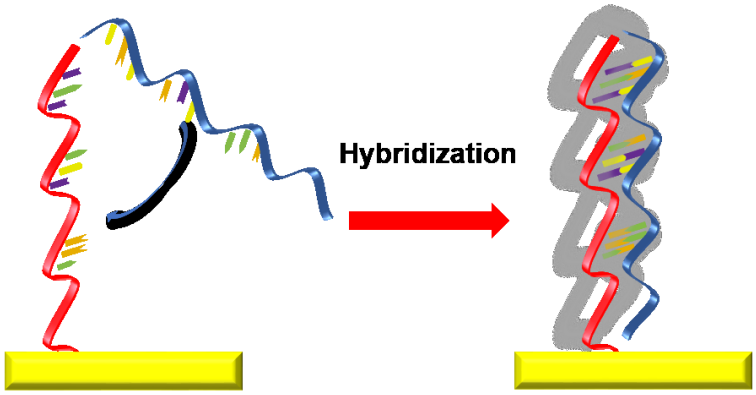

Figure 1.6 DNA hybridization on a sensor surface.

1.2.5 Biocompatible polymer-based sensing layers

Biocompatible polymers are synthetic or natural polymers that can be used to replace part of living systems or to function in intimate contact with living tissues. Aimed to interact with biological systems, these types of polymers can be used to detect, evaluate, treat or replace tissues, organs or their functions in live bodies. Synthesized polymers can be designed to respond to specific stimuli, showing various property changes such as conformation, color or shape. Usually, small changes in the environment can cause significant changes in the property of the polymers, making these polymers ideal sensing layer material for biosensing systems. Polymer-based sensing layers have been utilized in multiple areas such as pH/ion strength sensing[42,43], drug delivery[44,45], glucose monitoring[46,47].

1.3 Physical Transducers

Physical transducers convert the biological signals generated from target analyte binding onto bioactive sensing layers into a physical response that can be processed, record and analyzed by the readout system. Biosensors are usually classified by their transducer type (**Figure 1.7**). Traditional biosensors that have been studied extensively include: 1) electrochemical sensors, 2) optical sensors, 3) electronic sensors. Novel transducer platforms have emerged from the microfabrication industry. With the sensor scale minimized to micro/nanometer range, sensitivity and LOD are promoted significantly. In this thesis, we focus on microcantilever (MCL) sensors which are highly sensitive to minimized surface stress change. With a comparable scale of the targets (e.g. cells,

proteins), MCL sensors showed outstanding sensitivity and reliability in pathogen detection and protein folding study with optimized sensing molecules. By using a displacement conjugated polymer system, detection of small molecule (e.g. dopamine) is also achieved. We also employed other well-developed microfabricated transducer platforms such as electrochemical impedance spectroscopy (EIS) and surface plasmon resonance (SPR) for comparing and understanding the sensing layer-transducer interfaces.

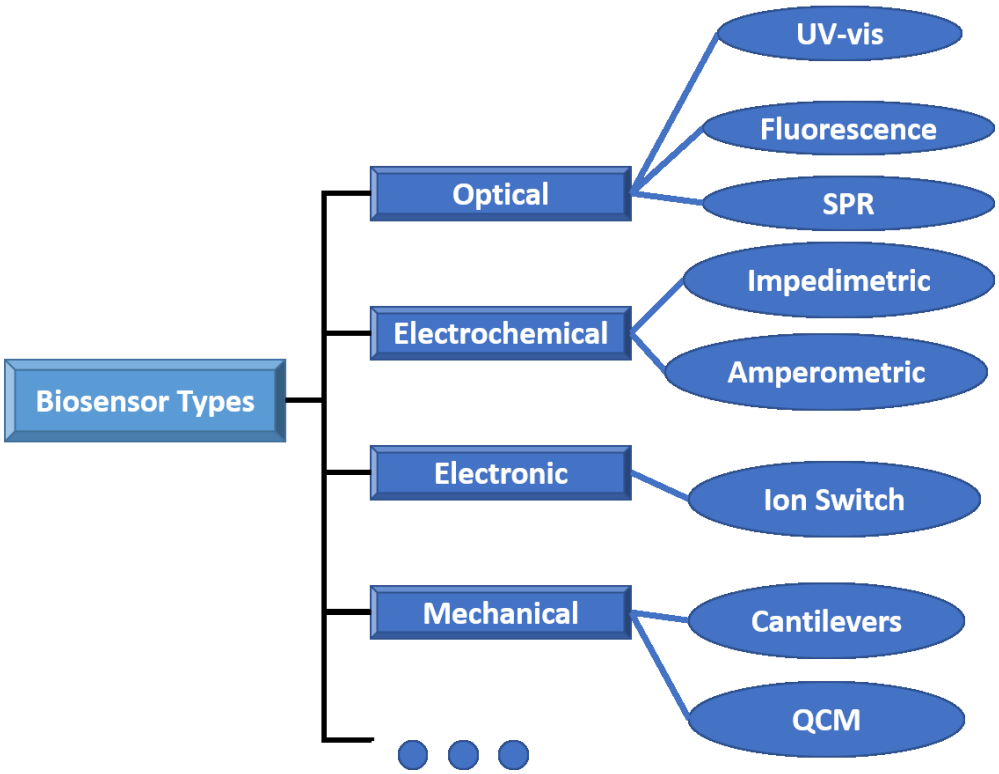

Figure 1.7 A brief summary of biosensor types based on transducers.

1.3.1 Electrochemical Transducer

Electrochemical sensors are among the first developed biosensor platforms. Obviously, an electrical signal will be generated once the analytes are detected. Usually, the signal will be proportional to the analyte concentration; thus, it can be quantified. Generally, there are several parameters that electrochemical sensors can detect, including: current (amperometric), potential (potentiometric), impedance and conductance (conductometric).[20,48–52] Amperometric transducers detect the change in current as a result of electrochemical redox. Potentiometric sensors measure the potential or charge accumulation in an electrochemical cell. Usually, a reference electrode with constant half-cell potential irrelevant from the analyte concentration is included. Conductometric sensors measure the change in sample solution's conductivity. The ionic strength change due to sensing layer-analyte binding will cause a measurable conductivity change. EIS is a methodology that measures resistance and capacitance change during the analyte binding to the sensing layer[53,54]. Typically, a sinusoidal stimulus is applied, providing current flow through the sensor system. The frequency is varied over a range to obtain impedance spectrum. Conventionally, a three-electrode system is used. Novel EIS is minimized and micro-sized interdigitate electrodes (IDEs) are fabricated on a sensor chip, performing as a lab-on-a-chip device. This kind of novel EIS will be further discussed in the following sections.

1.3.2 Fluorescent Biosensor

A fluorescent biosensor is one of the most important and widely used biosensors in laboratories and industry. It belongs to the category of optical sensors, which utilize photons to collect information about analytes. These sensors are highly sensitive, specific and accurate, providing either qualitative or quantitative results. The LOD of fluorescence spectroscopy is in the nano molar range but it usually requires labeled analytes[55–57]. Other limitations include stability (quenching) and large instrumentation size. A reagentless fluorescent sensor has been developed using a solvatochromic fluorophore which is sensitive to its local environment in a macromolecule.[58] When the sensing layer molecule binds to the analyte, the emission from this extrinsic fluorophore can be detected and quantified immediately. However, this method is still limited to certain compounds, and is typically applied with the antibody-antigen sensing layer-analyte group.

1.3.3 Electrochemical Impedance Spectroscopy (EIS)

As mentioned in previous sections, electrochemical impedance spectroscopy is a powerful tool measuring the resistance and capacitance change in a sensing system. Impedance is usually measured by applying a small AC potential excitation. The response of this potential, an AC current, is measured. This current signal can be analyzed as a sum of sinusoidal functions. The impedance (Z_ω) refers to the frequency dependent resistance to current flow of a circuit element (e.g. resistor, capacitor, inductor, etc.). It can be expressed as follows:

$$Z_\omega = \frac{E_\omega}{I_\omega} = \frac{E_0 \sin(\omega t)}{I_0 \sin(\omega t + \varphi)} = Z_0 \frac{\sin(\omega t)}{\sin(\omega t + \varphi)} \qquad (1-1)$$

E_ω and I_ω stand for the frequency-dependent potential and current. Compared with resistance sensors using DC voltage/current, there is more information content with EIS: it may be able to distinguish between two or more electrochemical reactions taking place; it can identify diffusion-limited reactions like diffusion through a passive film; it can also provide information about the electron transfer rate of reaction[53,59–62]. Several factors will affect the EIS measurement including: electrolyte resistance, double layer capacitance, polarization resistance, charge transfer resistance, diffusion and coating capacitance. EIS has been applied in studying metal corrosion, adsorption/desorption on the electrode surface, catalytic reaction kinetics and label-free sensing. EIS sensors have been used in bacteria detection[63,64], DNA hybridization detection[65,66] and so on.

1.3.4 Surface Plasmon Resonance (SPR)

SPR is an optoelectronic phenomenon occurring at the interface between a negative and positive permittivity material stimulated by incident light. At a specific incident angle (resonance angle), the polarized light can resonantly excite the delocalized electrons (surface plasmon) of the metal film, resulting in a minimum in the reflected light intensity[67–69]. This angle is recorded as the SPR sensorgram. This electromagnetic surface wave propagates in a direction parallel to the negative permittivity (metal)-dielectric material interface. Since this surface wave is on the boundary of metal and the medium,

the resonance is highly sensitive to any changes on the surface such as a refractive index variation[70]. Surface plasmon obeys the following dissipation relationship:

$$K_{sp} = \frac{\omega}{c}\left(\frac{1}{\varepsilon_1\mu_1} + \frac{1}{\varepsilon_2\mu_2}\right)^{-1/2} \qquad (1-2)$$

where ε is the relative permittivity, and μ is the relative permeability of the glass prism and the metal. The resonance angle strongly depends on the refractive index of the medium in close proximity of the metal surface[71]. Moreover, the local refractive index change is synchronous with the surface adsorption/desorption events. SPR sensors have been used to detect many target like DNAs[72], enzymatic reactions[73], antibody-antigen reactions[74], drug delivery[75] and small chemical molecules[70].

1.3.5 Microcantilever (MCL)

In recent years, microcantilever sensors have attracted much attention because of their potential as platforms for the development of myriad physical, chemical, and biological sensors.[76–79] Cantilever sensors emerged from atomic force microscopy (AFM), which is an offspring from the scanning tunneling microscope (for which the 1986 Nobel Prize was awarded, together with the inventor of electron microscopy). AFMs can image surfaces, nanosystems or single molecules with Angstrom resolution, manipulate molecules, or measure forces between individual molecules.[80] In particular, their operation under physiological buffer conditions makes them well suited to the investigation of biomolecular systems in their native environment with molecular resolution. The sensing element of an AFM is the flexible cantilever beam with a sharp tip. When the tip comes close or into

contact with a sample surface, a force is applied to the cantilever, which then bends.[81] Compared to AFM cantilevers, the microcantilever sensors are free-standing beams without sharp tips, which bend in response to different stimuli from the environment. Microcantilevers made of silicon or silicon nitride are usually fabricated with micrometer dimensions.[82] Microcantilevers can be excited to resonance by a number of methods including Brownian motion.[83] The resonance frequency of cantilevers changes with molecular adsorption. In addition, microcantilevers also undergo bending due to molecular adsorption. For a bi-material cantilever (e.g. gold coated silicon), differential molecular adsorption will induce a differential surface stress between the top and bottom surfaces. The differential surface stress between cantilever surfaces due to the molecular adsorption can be observed as the change of deflection.

Cantilevers bend when a force is applied to their end. This can be described by Hooke's law:

$$F = -k\Delta z \qquad (1-3)$$

where F is the applied force, k is the spring constant and Δz is the deflection of the free end of the cantilever beam. The spring constant determines the flexibility and the sensitivity of a cantilever and it is defined by the cantilever's dimension and material constants:

$$k = \frac{Ewt^3}{4L^3} \qquad (1-4)$$

where E is Young's modulus (Si, 155.8 GPa), w is the cantilever width, t is the thickness, and L is the length. The resonance frequency (f) of an oscillating cantilever can be expressed as:

$$f = \frac{1}{2\pi}\sqrt{\frac{k}{m^*}} \qquad (1-5)$$

where k is the spring constant and m^* is the effective mass of the microcantilever.[76] In some cases, adsorption of molecules on the cantilever surface can change the cantilever's spring constant and the resonance frequency can change due to changes in mass as well. Consequently, the shift in frequency can be expressed as:

$$\mathrm{d}f(m^*,k) = \left(\frac{\partial f}{\partial m^*}\right)\mathrm{d}m^* + \left(\frac{\partial f}{\partial k}\right)\mathrm{d}k = \frac{f}{2}\left(\frac{\mathrm{d}k}{k} - \frac{\mathrm{d}m^*}{m^*}\right) \qquad (1-6)$$

Changes in spring constant are related to changes in differential surface stress.[76] The spring constant, however, can also change during molecular adsorption if it results in amalgamation (changes in E) or swelling (changes in thickness). By designing cantilevers with localized adsorption areas at the terminal end of the cantilever (end loading), the contribution from differential surface stress ($\mathrm{d}k/k$ term in Eq. 1-6) can be minimized. In that case, the changes in resonance frequency can be mostly attributed to mass loading.

However, the resonance frequency of a cantilever decreases by a factor five when operated under solution.[83] Although mass detection using resonance frequency is attractive for

vapor-based sensing, increased damping renders the resonance frequency variation is not sensitive for operation under solution.

Microcantilevers also undergo bending due to mechanical forces involved in molecular adsorption. Such force was observed as early as 1858. Stoney derived a relationship between adsorption-induced surface stress and the radius of curvature of the substrate.[84] It was reported that adsorption-induced forces can be easily detected on so called "real surfaces" such as the surface of a microcantilever. Using Stoney's formula, the radius of curvature of the cantilever bending due to adsorption can be written as:

$$\frac{1}{R} = \frac{6(1-\nu)}{Et^2}\Delta\sigma \qquad (1-7)$$

where R is the radius of curvature, ν is the Poisson's ratio (Si, 0.28) and E is Young's modulus of the cantilever, t is the thickness of the cantilever beam and $\Delta\sigma$ is the stress change. The radius of the curvature of the cantilever bending is related to the cantilever beam deflection, z, and the length of the beam L. The relationship between the cantilever deflection and the differential surface stress is obtained as follows:

$$\Delta z = \frac{3L^2(1-\nu)}{Et^2}\Delta\sigma \qquad (1-8)$$

Therefore, the deflection of the cantilever is directly proportional to the adsorption-induced differential surface stress.

Adsorption-induced cantilever bending is ideal for liquid based applications. In addition, the adsorption-induced cantilever bending method has a sensitivity that is orders of magnitude higher than the resonance frequency variation based on adsorbed mass when operated under solution.

A typical MCL biosensor is modified on one side with a specific receptor which exhibits affinity for the analyte of interest. A surface stress differential will be introduced as a result of the specific interactions between the analyte and functionalized sensing molecules. The micromechanical bending caused by the surface absorption can be tracked. An MCL designed for sensing applications is generally modified in such a way that one side exhibits a strong affinity for the target analyte, whereas the other side is relatively passivated.[46] In this way, microcantilever beams are capable of detecting extremely small changes in forces, surface stress, and mass additions caused by the target analyte. A gradient in mechanical stress develops between the two sides of a cantilever as a result of interfacial processes governed primarily by changes in the Gibbs free energy associated with chemisorptive processes occurring on the active side.[85] Applying this concept, a diverse family of cantilever-based sensors have been developed, including environmental stimuli, endocrine disrupting chemicals, and various other vapor-phase analytes. Using surface modification on the cantilever surface with selectively sensitive layers, self-assembled monolayers (SAMs), or other functional groups/ligands, researchers demonstrated sensors with high selectivity and sensitivity based on the micromechanical silicon cantilever arrays.[86,87]

Besides the exquisite sensitivity in mass, stress and force, MCL sensors also offer many advantages including the easy fabrication of multi-element sensor arrays and the integration of micromechanical components with on-chip electronic circuitry. In addition, MCL sensors can exhibit comparable response time with other sensors like SPR and EIS. This allows monitoring the nanomechanical variation during the biological process on the timescales of milliseconds. All the advantages make research of the microcantilever based biosensor is a promising field. A novel, portable, real-time biosensor is expected to be developed.

1.3.6 Microfluidic Cantilever

It is critical to create a selective sensing layer in order to have a microcantilever sensor with specificity. Surface functionalization, as a result, is a key step in biosensor design. The formation of a uniform SAM is one of the most common methods promoting the selectivity of the cantilever sensors. However, immobilization of receptors generally results in the formation of sub-monolayers or discontinued layers and that results in large variations in the reproducibility in the sensor response. Unlike large area sensors such as QCM and SPR, cantilever sensors have an extremely small surface area. The typical surface area of a cantilever sensor is 10^{-2} mm^2. Therefore, the probability of defects forming in the monolayer is much higher than that for other conventional sensors with large areas.[88]

Hollow channel microfluidic cantilevers are developed to solve the dissipation problem for liquid sample detection. By fabricating microfluidic channels on top of a plain cantilever surface, analytes in an extremely small volume (in the picoliter range) of a liquid sample

can be detected with extremely high sensitivity[89–91]. This sensor offers a platform for samples detection with fundamental physical properties such as mass and density. Understanding the unique physical properties involved in biological processes will make it possible to develop novel biosensors. With the inner surface functionalized, the hollow channel cantilevers can also selectively bind to target analytes.[92]

By integrating with other techniques, such as infrared (IR) spectroscopy, molecular recognition can be achieved with a method called photothermal spectroscopy. With the mid-IR exciting the target molecules inside the finite microfluidic channel, target molecules can be determined without the surface functionalization.[93] In photothermal spectroscopy, the amplitude of the cantilever deflection (as a function of an illumination wavelength) has a linear relationship to the concentrations of the molecules absorbing the IR light. This makes cantilever-based IR spectroscopy an excellent method for molecular recognition on a small scale.

In summary, a hollow channel microfluidic cantilever is a sensor platform with extremely high sensitivity that needs a very finite sample amount. It is ideal for studying the micromechanical property change involved in bioreactions.

1.4 Surface Functionalization Methodology

As discussed before, the selectivity of the microfabricated sensor comes from the sensing layer anchored on the sensor surface. By immobilizing a monolayer of a molecular recognition reagent (i.e. a polymer or a peptide) to the sensor surface, a bio-selective sensor

can be prepared. Adsorption of the analyte will change the electrical property, surface plasmon resonance, or surface stress on the surface. This will make it possible to detect the induced physical signal. Depending on the interaction between the receptor and the analyte, the reversible/irreversible absorption will produce instantaneous/dosimetric responses.[83] The challenge in this approach is to adapt known interaction chemistry to the transducer platform in a manner that maintains the required chemical selectivity and stability.

As we stated before, selectivity is one of the outstanding challenges in biosensor development. Immobilization of receptors to physical transducers is a critical factor for creating the selective sensing layer. Coating strategy needs to be simple, quick, homogeneous, and stable and should be used for immobilization of various sensing agents or specific receptors without leaching. There are three widely used methods to coat the sensor surface: (i) physisorption of receptors on the sensor surface, (ii) direct covalent attachment of the receptor to the sensor surface and, (iii) encapsulation or entrapment of the receptor in a polymeric matrix. A typical example is the functionalization of MCL sensors.

The adsorption of receptors on the MCL surface can be accomplished by immersing the cantilever in a solution of a specific concentration of receptors to form a SAM. For example, a convenient and widely used method to coat the MCL is by inserting the MCL into an array of dimension-matched disposable glass capillaries containing the sensing layer molecules.[94,95] Moreover adsorption of receptors can be achieved by electrochemical deposition. To measuring surface stress, it is important to keep sensing molecule density difference at a large scale. This can usually be achieved by a passive coating on the other

side of the cantilever.[96,97] Recent research shows that by controlling the ligand concentration, a significant surface density difference can be created between the top and bottom surface.[98,99] Thus, backside passivation can be avoided. Depending upon the material of the cantilever which is generally silicon, silane coupling chemistry is extensively used. Thiol coupling chemistry is often used to covalently bind receptors to the gold-coated cantilevers. For polymers like SU8, epoxy groups can be used for coupling to the surface.

Adsorption induced-stress in MCL depends upon the number of molecules adsorbed on the surface which in turn results in nanometer-scale deflection of the MCL. Molecular adsorption reactions on the surface are driven by free energy changes of the surface due to physisorption or chemisorption. Nonspecific binding of the receptor results in very weak binding of ligands or chemicals on the surface of MCL. These ligands and chemicals are subject to desorption.

Self-assembled monolayers: Adsorption of receptors on MCL is mostly carried out using a SAM formation.[100] SAMs can be formed both on gold as well as silicon cantilevers by immersing the cantilever in organic solvents or in aqueous solutions. The formation of a SAM on a planar MCL surface can be achieved by dipping the MCL in a dilute solution of organic ligand (approximately 1 mM) for a specified time followed by thorough washing with the same solvent and drying under nitrogen flow.[101]

SAM generation on silicon MCL: Strongly bound chemisorbed silanized SAMs on silicon cantilevers are most common. Alkylsiloxanes (R-Si-O-Si) are prepared by the simple self-

assembly of active silanes (e.g. alkyltrichloro- ($Cl_3Si(CH_2)_nR$) , alkyltrimethoxy- ($(MeO)_3Si(CH_2)_nR$), or alkyltriethoxy- ($(CH_3CH_2O)_3$ $Si(CH_2)_nR$)) onto the solid substrate.[102] The formation of SAM is simple as silanization reaction can be easily carried out; however, it is a challenge to form the reproducible monolayer.[103,104]

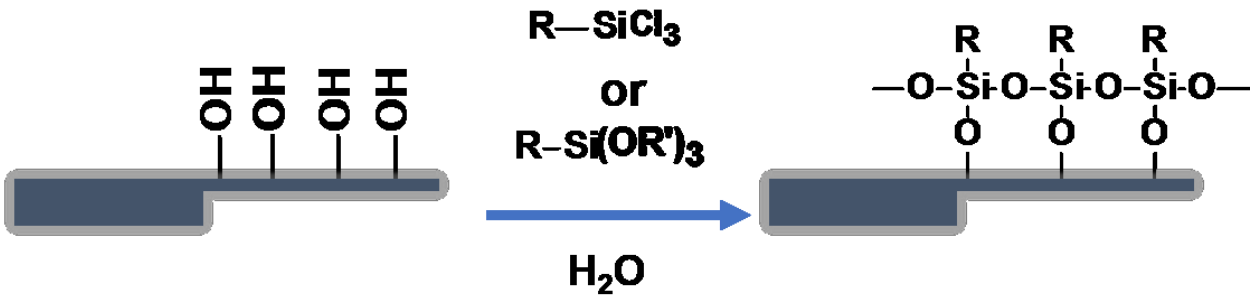

Figure 1.8 SAM functionalization on silicon MCL.

The most widely used amino functionalized silane for silicon cantilevers is (3-aminopropyl)triethoxy-silane (APTES). However, the amine groups of the aminosilanes can form hydrogen bonds with surface silanol or -OH groups during condensation, leading to a decrease in the effective amine density on the surface of the materials present.[105] **Figure 1.9** shows the different possibilities of surface interactions between aminopropylsilane and silica. The formation of uniform thin films of aminosilanes is most important and crucial step for their use as surface coupling agents.

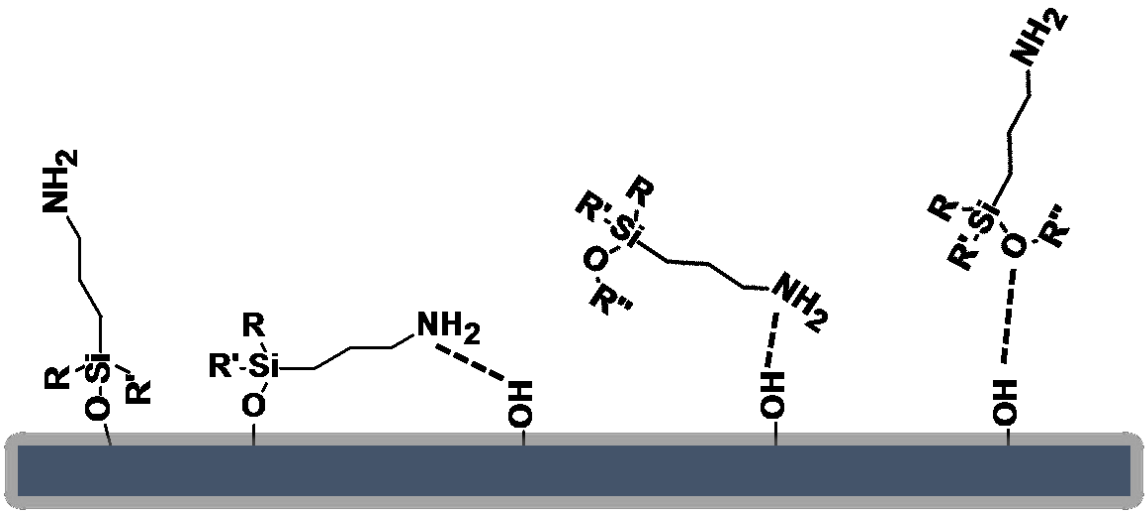

Figure 1.9 The different possibilities of surface interactions between aminopropylsilane and silanol or -OH groups on silicon surfaces.

SAM generation on gold MCL: The most popular ligands for SAM formation on Au MCL are alkanethiol (R-SH), as presented in **Figure 1.10**. The gold-sulphur binding is based on "soft" gold and sulfur atoms whereas other functional groups such as amines ($-NH_2$), carboxylates (CH_3COO^-), hydroxides (OH^-), alkoxides (^-OR), hydrazine (N_2H_4) and halogens (F^-, Cl^-) do not interact strongly with gold.[106] Hence, functionalized alkane thiols are used to connect different receptors to the gold MCL. **Figure 1.10** represents the self - assembly of alkanethiols and functionalized alkanethiols on the Au coated microcantilever surface. The mechanism of adsorption of thiols on the Au surface and nature of metal-thiolate bond is not clear and is an area of extensive debate. However, two mechanisms have been proposed one is oxidative adsorption mechanism[107], and the other is the electrochemically assisted formation of thiol SAMs on the Au surface.[108,109] Assuming that Au_n are the atoms in the bulk and Au_m are the atoms on the surface of cantilever, the

SAM can be indicated as Au_n $(Au\text{-}S\text{-}R)_m$ and the adsorption mechanism can be represented as shown in equation (1-11).

$$Au_{n+m} + mRSH \rightarrow Au_n\ (Au\text{-}S\text{-}R)_m + mH^+ + me^- \qquad (1\text{-}11)$$

Two distinct phases are indicated in the formation of the self-assembled monolayers in solution. The first phase is the adsorption of S-headgroups on the gold substrate, which takes a few minutes. The second phase corresponds to the arrangement of hydrocarbon chains in an all-trans-ordered fashion.[110,111]

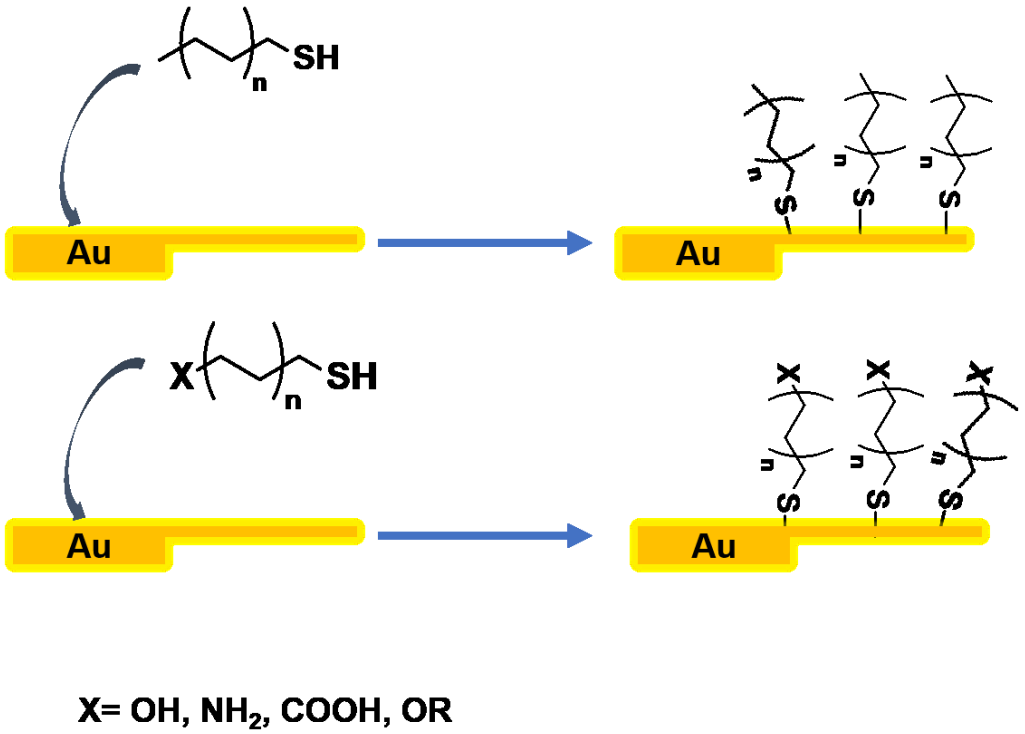

Figure 1.10 Self-assembled monolayer generation of alkanethiols on Au substrate.

1.5 Readout Systems

A readout system converts the physical signal from the transducer to signals can be recorded, stored and analyzed. Obviously, most of the current readout systems convert the mechanical, optical and electrical signals into digital signals. Thus, they can be processed and stored by computers. The readout system, in many cases, is the most expensive part of a biosensing system. The important characters of a readout system include but are not limited to readout accuracy, data acquisition rate, algorithm, and compatibility with transducers. When developing portable, or even wearable sensors, it is important to consider the physical dimension, energy consumption, reliability and cost of the readout system. Developing a readout system with high efficiency, low cost and condensed size will boost biosensor applications in various fields.

1.6 Thesis Proposal

The research objectives of this thesis are to (1) explore molecules suitable for the specific bio-analyte detection which can be assisted as the sensing layer; (2) optimize the surface functionalization in order to improve the selectivity, reliability and signal/noise ratio(SNR) of the mechanical sensors; (3) develop novel biosensors which can monitor the nanomechanical properties change involved in the biological process and by analyzing the thermodynamic and nanomechanical variations associated with biological process, new approaches for sensing and diagnostics will be designed.

The ultimate goal of this thesis is to develop portable, label-free biosensors with high selectivity and sensitivity. However, biosensor development is a never-ending field because of the demand of detecting a growing number of different molecules for everything from clinical analysis to environmental control and for monitoring many industrial processes. Our results proved the MCL assisted by the various sensing molecules can achieve quick-response and highly-selective detection of pathogen cells, protein conformation change, trace amount of neurotransmitter molecules and DNA melting process, covering the target scale from micrometer range to sub-nanometer range. Due to the compatible size with MEMs sensors and biological targets, nanomechanical devices are suitable for detecting and analyzing multiple biological processes. The proposed research in this thesis is significant because it will lay the foundation for reliable platforms of MEMs biosensors and also lead to portable, real-time detection for environmental monitoring and clinical analysis.

Furthermore, the proposed nanomechanical biosensor design and development will provide a platform and methodology for future sensor studies. Also, the interdisciplinary nature of the proposed work will provide state-of-the-art training in surface physics and chemistry, molecular biology and biochemistry, and device design and engineering.

Chapter 2. Methodology and Experimental Section

As we stated in the introduction part, our goal is to develop label-free, fast-scan biosensors for pathogen detection, biomedical diagnostics, and environmental monitoring. We aim to design and develop specific sensing layers for target analytes and combine them with highly-sensitive transducers. By understanding the principles of integrating the interfaces between the analyte-sensing layer and the sensing layer-transducer, novel sensors can be developed with high sensitivity and selectivity. In this chapter, we will state and discuss the methodology for developing the biosensing systems and experimental details.

2.1 Materials

All reagents and solvents were of analytical grade and used as received with no further purification. The water used in this work was from a MilliQ instrument (deionized, 18 MΩ cm^{-1}).

2.1.1 Antimicrobial peptides (AMPs) and short peptide fragments

In this thesis, we used several antimicrobial peptides for pathogenic bacteria detection study. It consists of 37 amino acid residues and similar to other class IIa bacteriocins, it is characterized by a conserved disulfide bond between Cys9 and Cys14 and a YGNGV sequence near the N-terminus and a C-terminal domain with an amphiphilic α-helix ending with a hairpin-like structure at the C-terminal tail (**Figure 2.1A**). LeuA was chemically synthesized using solid phase peptide synthesis as described previously.[112] Leucocin A

(LeuA) is a well-known, naturally existing AMP of class IIa bacteriocins.[113,114] LeuA exhibits very potent activity against *Listeria monocytogenes (L. monocytogenes)* in a nanomolar range [minimum inhibitory concentration (MIC) of 0.1 nM].[115]

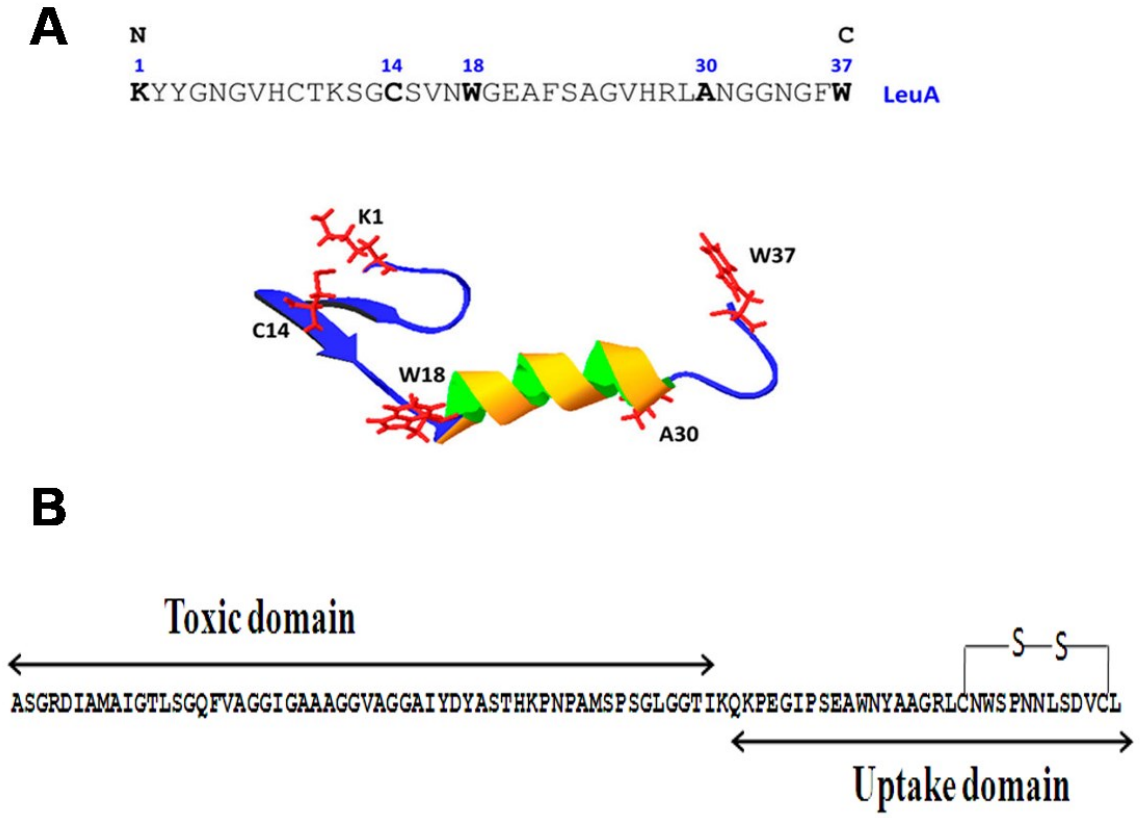

Figure 2.1 Sequence of Leucocin A (LeuA) and Colicin V (ColV).

We also used Colicin V (ColV) for *E. coli* detection. ColV is an 88-amino-acid, linear unmodified AMP (**Figure 2.1B**).[32] It is a type of bacteriocin produced by *E. coli* which acts against *E. coli* strains by binding to the outer membrane receptors and using them to translocate the cytoplasmic membrane, leading to membrane depolarization, which

ultimately kills the cell.[32,33] ColV was genetically expressed and purified from cultures of *E. coli* strain *MC410*0 as previously described.[33]

Based on class IIa bacteriocins (LeuA, PedPA1 and CurA), a peptide array library comprising 24 short peptide sequences (each 14 amino acids long) was synthesized in duplicate on a cellulose membrane using SPOT synthesis. 34 Short peptide sequences were derived from the sequence of full-length class IIa bacteriocins Leucocin A, Pediocin A, and Curvacin A. Briefly, from the full-length Leucocin A, 13 peptides of 14 amino acids in length, skipping two amino acids, were derived, and six and five peptides were derived from the central amphipathic α-helical region of Pediocin A and Curvacin A, respectively. The peptide array was synthesized on a PEG-500-derivatized cellulose membrane with a free amino terminal group using a semiautomatic robot AutoSpot ASP222 (Intavis AG, Germany). The three selected peptide fragments (Leu10, Leu13, and Ped3) were synthesized by an automated synthesizer (Tribute, Protein Technology Inc., USA) utilizing solid-phase methods.[116]

2.1.2 Bacteria Strains and culture

Bacterial strains, pathogenic (level II) and nonpathogenic, namely, *Listeria monocytogenes* (*L. monocytogenes* ATCC 19116 and ATCC 43256), *Listeria innocua* (*L. innocua* ATCC 33090), *L. mesenteroids* (UAL 280), *Staphylococcus aureus* (*S. aureus* ATCC 13565), *Escherichia coli* (*E. coli* ATCC 25922), *Samonella enteritidis* (*S. enteritidis* ATCC 13076), *Enterococcus faecalis* (*E. faecalis* ATCC 19433) and *Pseudomonas fluorescens* (*P. fluorescens* CHA0) were used in this study. All strains were obtained from the cell bank of

CanBiocin, Inc. (Edmonton, AB, Canada) and were subcultured in their respective appropriate media, like APT or LB broth. All related experiments were carried out in a level II biosafety cabinet.

2.1.3 Human serum albumin (HSA)

Human serum albumin (HSA) is a widely studied protein that accounts for more than 50 % of total plasma protein concentration with the molecular weight of 65 kD.[117–119] HSA is known to undergo pH-dependent conformational isomerization. At physiological pH of 7.4, the HSA is identified as a heart-shaped molecule existing in normal (N) form. However, at pH greater than 9, the transition takes place to basic (B) form, where it is believed that the heart shaped structure is changed into an ellipsoid. At acidic pHs below 6, it is believed to exist in fast (F) form (**Figure 2.2**).[120,121] Fresh HSA sample and denatured HSA were compared in this study to determine protein conformational change and surface stress induced during the process caused by variation of pH of the solution. Denatured HSA was prepared from 2mg/ml of HSA solution in PBS buffer heated at 60 °C for overnight. The HSA samples were then functionalized on to the sensor surface through a PEG_{12}-CL ligand via EDC chemistry before tests (will be discussed in following sections).

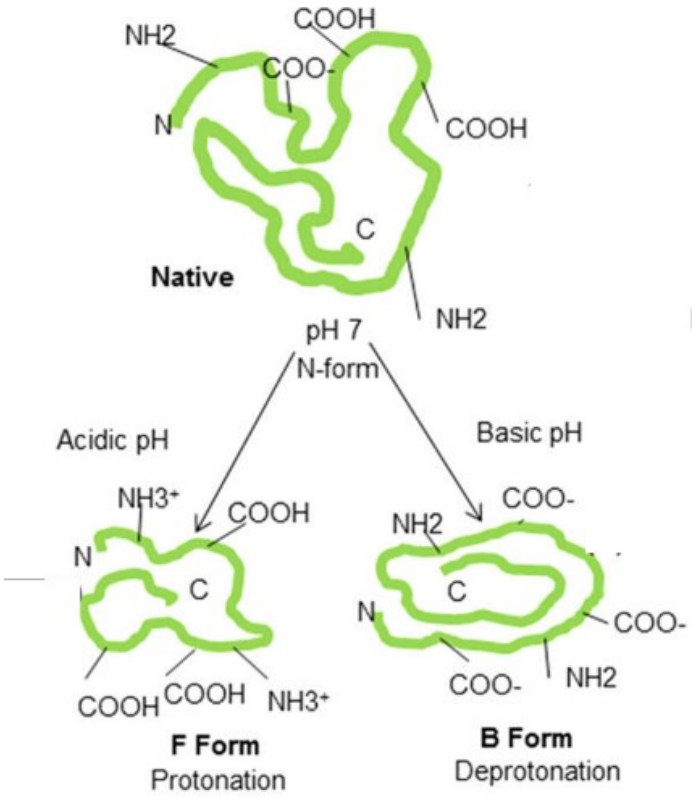

Figure 2.2 A scheme illustrating HSA at the normal form (N), basic form (B) and fast form (F).

2.1.4 Oxaborole based polymer and glycopolymer

Boronic acid is well known for its interaction with molecules having a cis-diol configuration to form stable cyclic esters[122]. A copolymer poly(*N*-isopropylacrylamide-*st*-5-methacrylamido-1,2-benzoxaborole) (P(NIPAAm-*st*-MAAmBO)) has been synthesized by reversible addition-fragmentation chain transfer (RAFT) polymerization by Narain and coworkers[123]. The conjugated polymer layer used in this work consisted of P(NIPAAm$_{149}$-*st*-MAAmBO$_{19}$) (MAAmBO content: 12 mol%, M_n: 13200 g mol^{-1}, M_w/M_n=1.27) and P(LAEMA$_{21}$) (M_n: 10000 g mol^{-1}, M_w/M_n=1.1)[123](**Figure 2.3**). All the polymers were

synthesized following previous work,[124–127] following a reversible addition-fragmentation chain transfer (RAFT) polymerization methodology.

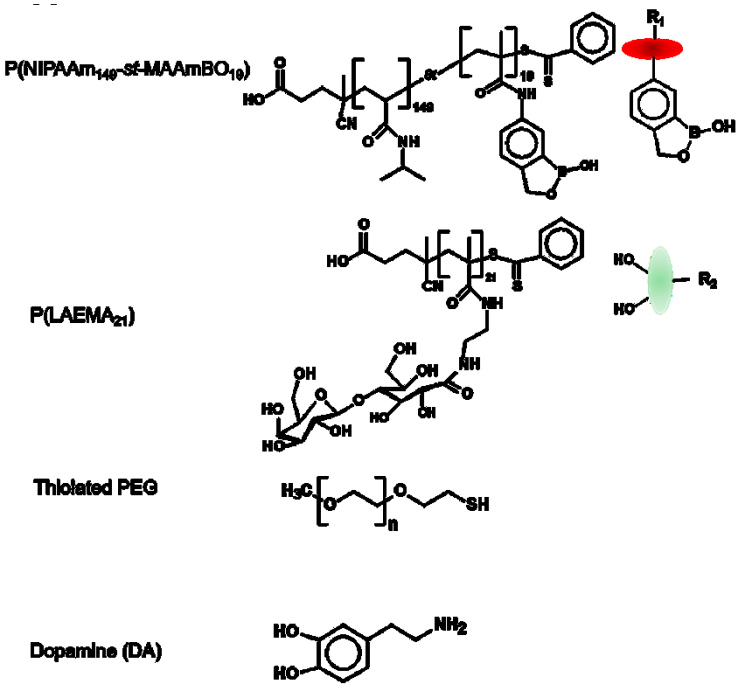

Figure 2.3 Formula, structure, and scheme of the polymers.

2.1.5 DNA samples from melting test

DNA samples (Integrated DNA Technologies) with designed sequence were used in this thesis for the study of DNA melting. ssDNA samples were incubated with 1× PBS at room temperature for hybridization before melting measurement. DNA samples with varied sequence length and GC content are designed to compared the physiochemical property change during the melting process.

2.2 Surface Functionalization

As we discussed in Introduction part, surface functionalization is the most important approach to enable the selectivity of biosensors. Many approaches can be used to immobilize the sensing molecules to the cantilever sensor. For a typical gold-coated silicon-based sensor surface, thiol chemistry and silane chemistry can be applied to functionalize the gold side and the silicon side.[128–130] For thiol self-assembled monolayers (SAMs) and organosilane modification, dip-coating is the preferred method for immobilization of recognition molecules with high density on cantilever surface. Thiol SAMs are self-limited to coverage of a monolayer or less of the thiol on a gold film[131–134]. Organosilane coatings can form multi-layer coatings depending on the exposure time and the concentration of the solution.[135–137] One key condition for both coating chemistry is keeping the experimental surface freshly prepared. Stability of the functionalized surface depends mostly on the reagent itself and can last from 24 h to several weeks.[138] For the various sensing layers and transducers we have studied, we developed specific protocols in order to create optimum sensing layer-transducer interfaces.

Gold coated sensor surface (MCL, SPR, IDEs, etc.) is usually used in this thesis unless stated separately. A typical gold coating protocol is as follows: The sensor chips cleaned using piranha (H_2SO_4: H_2O_2 (3:1)) for 10 min, washed with plenty of MilliQ water and rinsed in ethanol. The freshly cleaned sensor chips were coated with 5 nm titanium (Ti) adhesion layer followed by 50 nm gold (Au) using an electron beam (Ebeam) evaporator (Kurt J. Lesker, USA) at a deposition rate of 0.2 Å sec^{-1}. The gold coating process was

carried under high vacuum (below 10^{-6} Torr) with nitrogen as inert gas protection. The gold coated sensors chips will be kept in vacuum desiccators until functionalization.

2.2.1 Functionalization of AMPs

AMPs have relatively short sequence and less molecular weight comparing to proteins. We use short thiol linker to immobilize AMPs without thiol groups Surface functionalization with antimicrobial peptide was based on the covalent interaction between the accessible carboxylic group of the peptide and a free amine group of a thiol linker pre-attached to the gold surface. **Figure 2.4** shows schematic of a typical sensing platform revealing the immobilization approach (a gold coated interdigitated electrode sensor as in this example). First, the gold coated sensors were functionalized with a cysteamine linker ($HSCH_2CH_2NH_2$) by treatment with cysteamine hydrochloride (0.01 M) in concentrated buffer solution (8× PBS, pH 8.1) for 6 h.[139] The gold surface was then rinsed with 1× PBS (pH 7.4) to remove any unbound thiol linker. A stock solution of AMP (800 μg/mL) in 1× PBS (pH 7.4) containing EDC (0.2 M) as an activating agent was injected into the sensing chambers and incubated overnight at room temperature. The functionalized surface was then rigorously washed with 1× PBS to remove any unbound AMP, rinsed with deionized water, and dried with nitrogen flow. The functionalized sensor chips were used for bacterial cell screening.

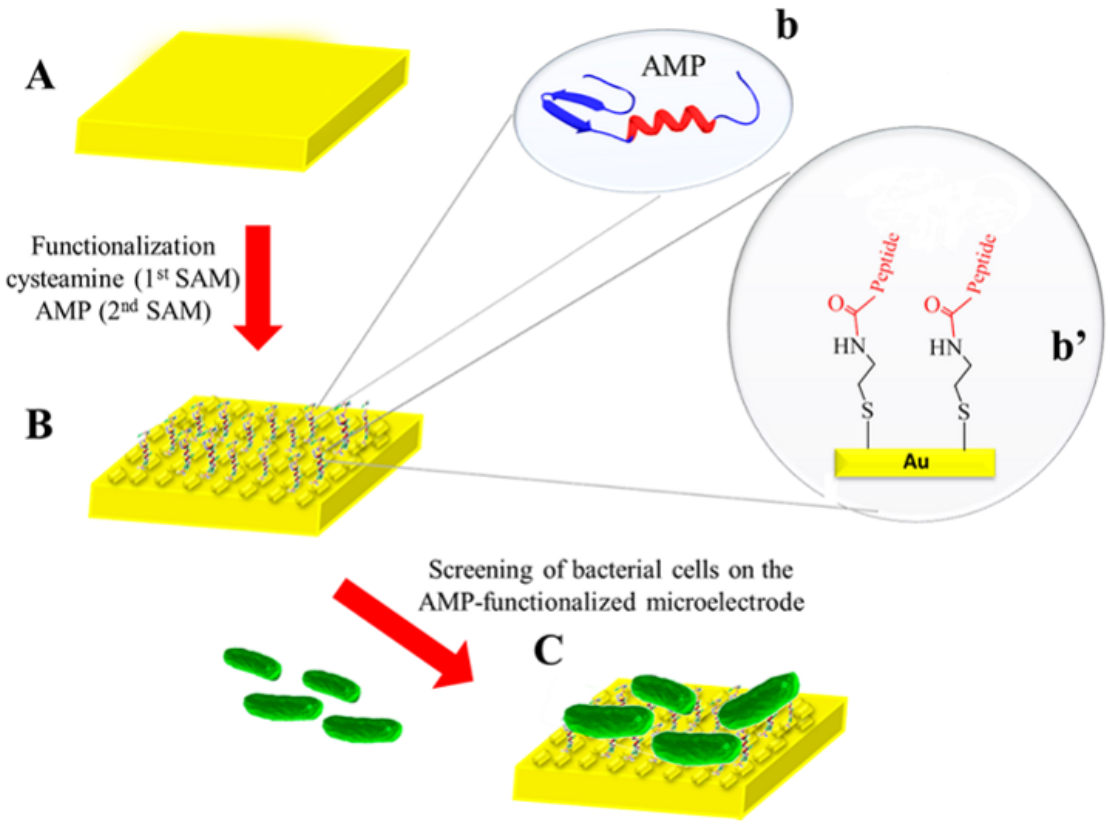

Figure 2.4 A typical AMP functionalization and detection approach on a gold coated sensor surface (electrode). A. gold coated sensor surface; B. immobilization of cysteamine as the linker and AMP as the sensing layer; b and b' shows a scheme of AMP structure and the final orientation on gold coated surface; C. the functionalized AMP detects bacterial cells.

On the other hand, AMPs with a thiol group on one terminal or thiolated AMPs can be directly functionalized on to gold coated sensor surface. For example, we also designed peptide 18-4 with a thiolated C-terminal which makes it possible to be immobilized on gold coated microcantilever surface without EDC chemistry.

2.2.2 Functionalization of HSA

HSA is a protein with 65 kDa molecular weight. Thus, a 12-carbon linker is used for HSA immobilization on microcantilever surface. The freshly coated microcantilevers were cleaned using UV-ozone cleaner for 3-5 hrs and rinsed with ethanol. Dried cantilevers were passivated with PEG-silane on the backside. Gold side of the cantilever was functionalized by immersing in 1mM PEG_{12}-CL solution in PBS buffer (20 mM Na_2PO_4, 0.15 M NaCl) at pH 7.4 for 3 hrs. After cleaning the microcantilevers and removing the excess reagent, activation of the carboxyl group was carried out by zero length crosslinking agent EDC and sulfo-NHS. The microcantilevers on the array were immersed in 0.2M EDC and 50 mM sulfo-NHS prepared in MES buffer (0.1M MES, 0.5M HCl) at pH 6 for at least 30 min and stirred at very low speed. Excess of the reagent was removed by washing the cantilevers in the buffer solution. Each of the activated microcantilevers was functionalized with HSA or denatured HSA for 2 hours leaving the rest of four cantilevers as references. Hydroxyl amine was used to block the active sites on the reference cantilevers and unreacted active carboxyl moieties on the protein immobilized cantilevers.

2.2.3 Conjugated polymer systems

The polymer functionalization was performed in a three-step manner. P(NIPAAm$_{149}$-*st*-MAAmBO$_{19}$) was first introduced to the gold coated surface and self-assembled monolayer (SAM) was formed via thiol-Au covalent bond through the dithioester group at the polymer terminal (red, **Figure 2.5A**). The second layer of P(LAEMA$_{21}$) was conjugated to the sensor substrate by the oxaborole-diol interaction described previously (green, **Figure**

2.5B). After rinsing with PBS, the chip was treated with thiolated poly(ethylene glycol) (PEG) to block any uncovered gold surface in order to avoid non-specific adsorption onto the gold surface (purple, **Figure 2.5C**). A PEG functionalized chip was also used as a blank control to eliminate noise and other systematic errors. All the surface functionalization steps were performed in pH 7.4 PBS solution at room temperature. The functionalized sensor chips were rinsed with PBS to remove any excess polymer molecules or physically adsorbed molecules before detection experiments.

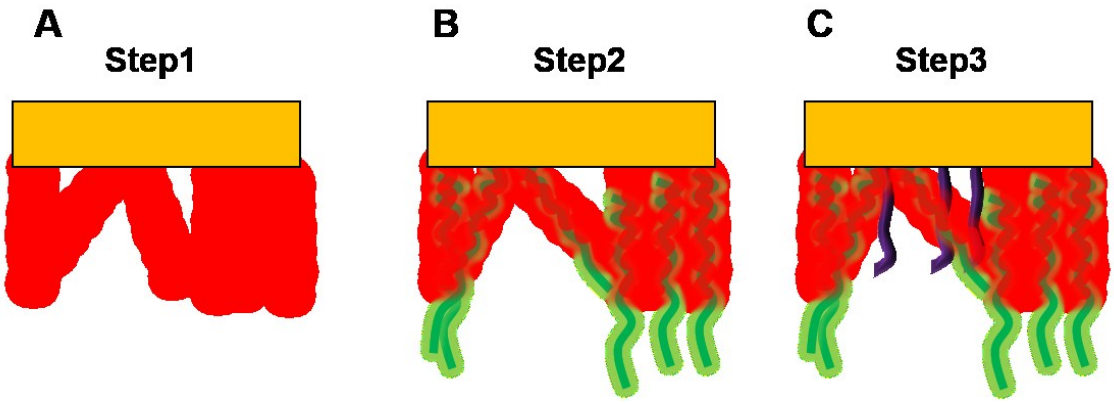

Figure 2.5 Structures of polymers and the three-step functionalization method for immobilizing the conjugated polymer system.

2.3 Biosensing Systems

2.3.1 Impedance analyzer

In this thesis, a SHARP IA-2 impedance biosensor (SHARP Laboratory of America, USA) was used to measure the impedance response caused by the affinity binding of the bacteria.

The impedance sensor array consists of three microfluidic reaction chambers with five pairs of gold interdigitated electrodes (IDEs) in each chamber. The dimensions of each electrode are 3350 µm/100 µm/150 nm and the spacing between each electrode is 40 µm (**Figure 2.6**). In order to avoid any interference and eliminate any signal as a result of non-specific adsorption and buffer effects, we used a blank reaction chamber with corresponding buffer/solution as a reference channel for differential readout.

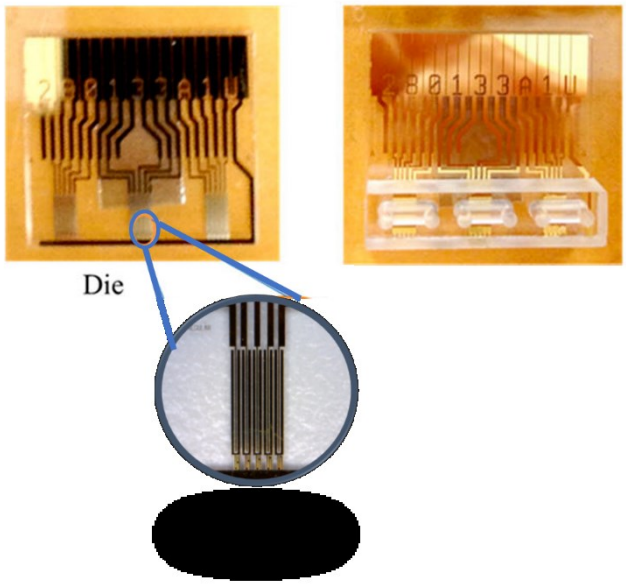

Figure 2.6 Images of the impedance sensor array and the zoomed-in image of the IDEs.

When the AMP captures its specific target biomolecules from the surrounding medium, the molecular interactions lead to changes in the sensor's impedance that are correlated to the type and amount of the bound analytes. The changes thereby are detected, measured, and analyzed by monitoring impedimetric parameters.

The data presented in this thesis were performed at 10−160 Hz and 100 mV stimulation signal for bacterial detection. The operation frequency was initially optimized by screening bacteria samples at various frequency. The frequency giving maximum net impedance change with sample injection will be used for the rest of the detection tests. The sensitivity, resolution, and selectivity of the sensor array were tested by injecting bacteria samples into the microreaction chambers separately. Samples were kept in the reaction chamber until the impedance variation reached an equilibrium state. PBS was used to rinse the microreaction chambers.

All the recorded results were analyzed using the Sharp BioZ software package. Impedance magnitude and variations in other parameters were compared to determine the sensor characteristics.

2.3.2 Surface plasmon resonance

In this thesis, we used Navi 200 (BioNavis, Finland) for the SPR measurement. The instrument is designed based on Kretchmann configuration (**Figure 2.7A**). The injection loop volume is 100 µL and injections are controlled by a 6-way valve. The flowcell has two separate channels, with 1 µL in volume each and 100 µm in height. The flow is switched to PBS after each injection to rinse the flowcell loop and the sensor chip surface. The laser wavelength used is 760 nm. SPR sensor chips were fabricated based on lime soda glass slides. The dimensions were fixed as 2 cm×1.2 cm×0.05 cm. The sensor chips can be coated with a series of metals such as gold, silver, copper, and other metal oxides (**Figure 2.7B**). The most commonly used are gold coated sensor chips.

The functionalized SPR chip was attached to the prism of SPR instrument through an elastomer layer. PBS was flowed continuously through the sensor chip surface and a typical flow rate is 10 L/min. Samples were injected through the 100 µL loop. This binding change was monitored by the variation in the resonance angular shift.

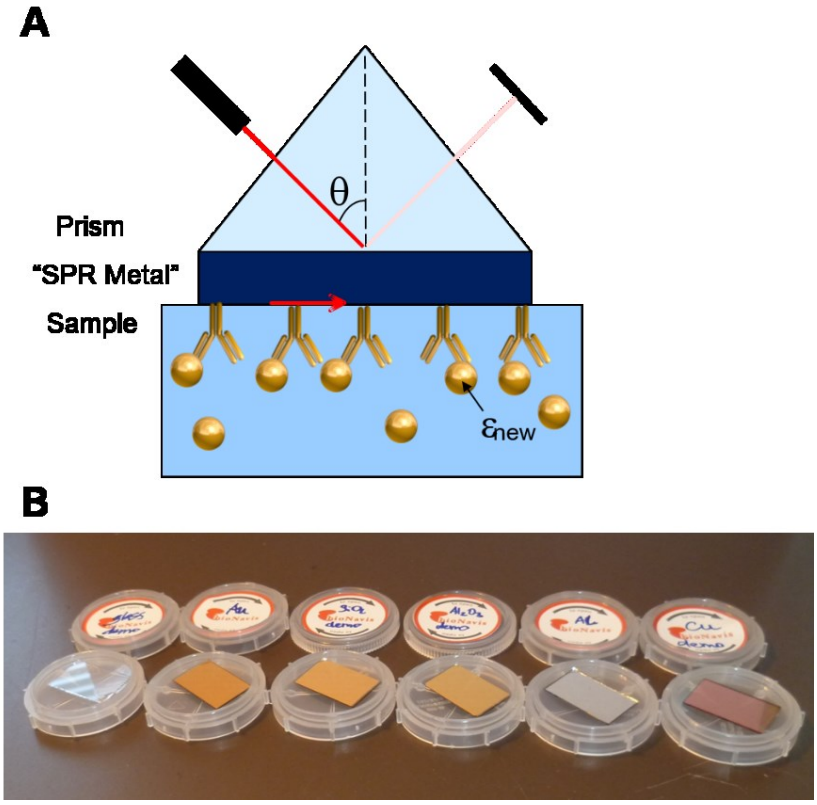

Figure 2.7 Scheme of SPR instrument and images of SPR sensor chips: A. Scheme of Navi 200 SPR instrument designed based on Kretchmann configuration; B. SPR sensor chips coated with metals and oxides.

By functionalized the SPR sensor chip surface with AMPs, we were able to detect circulating tumor cells (CTCs) in spiked samples. Conformational change of HSA was also

measured by functionalized SPR sensor. With designed conjugated polymer layers, we were able to detection neurotransmitter (dopamine, DA) to nanomolar range with high selectivity.

2.3.3 Microcantilever system

Deflection measurements were carried out using a homemade cantilever deflection sensing system with a liquid flow cell. The laser beam was focused on the cantilever's free end and the "compressive" (negative deflection, towards silicon side) and "tensile" (positive deflection, towards gold side) stresses of the cantilever were measured by monitoring the position of the reflected laser beam on a position sensitive detector (PSD). Data from nanomechanical cantilever deflections were recorded in real-time using a multifunctional data-acquisition board driven by LabView-based software. **Figure 2.8** shows the experimental set-up for the cantilever deflection sensing system. Microcantilever bending deflection was measured using a home-made system. Functionalized MCL array is mounted in a flowcell with 200 μL volume and PBS buffer flow was introduced by a syringe pump and sample injections are also controlled by a 6-way valve with injection loop volume of 2 mL. The PBS buffer solution was set to flow through the cell using a syringe pump and the flow rate was set at 5 mL min^{-1}. Stoney's formula was used to determine surface stress.

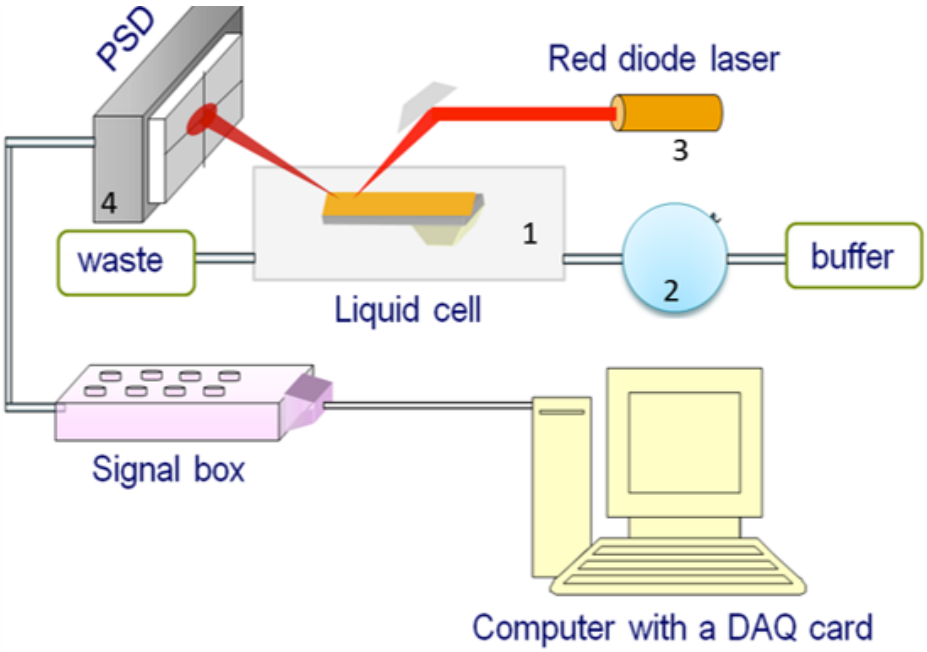

Figure 2.8 A schematic of the MCL detection system. 1) MCL mounted in a Liquid cell; 2) syringe pump; 3) red diode laser for deflection test; 4) position sensitive detector (PSD).

AMPs and short fragments functionalized MCL sensors were capable of detecting corresponding strains to 10^3 cfu mL^{-1} level. MCL is also used to monitor the protein conformational change with pH variation. With the designed conjugated polymers, the MCL sensor can detect dopamine at picomolar range with high selectivity.

2.3.4 Hollow channel microfluidic cantilevers

The hollow channel cantilevers were fabricated using top-down microfabrication techniques as described in previous work[140,141]. The hollow channel cantilever used for this work is 500 µm in length, 20 µm in channel width, 3 µm in channel height (**Figure 2.9**). The vibration of the hollow channel cantilever was measured by an MSA-500 laser Doppler

vibrometer (LDV, Polytec, USA). The resonance frequency, vibration amplitude and quality factor (Q factor) were measured simultaneously. Measurement is usually carried in a homemade vacuum chamber in order to reduce the damping caused by air. DNA samples were injected and sealed in the microfluidic channel, and the whole chip was heated from the bottom at a rate of 1 °C/min. DNA melting induced Q factor variation was recorded and analyzed, as long as other physical parameters as frequency and amplitude.

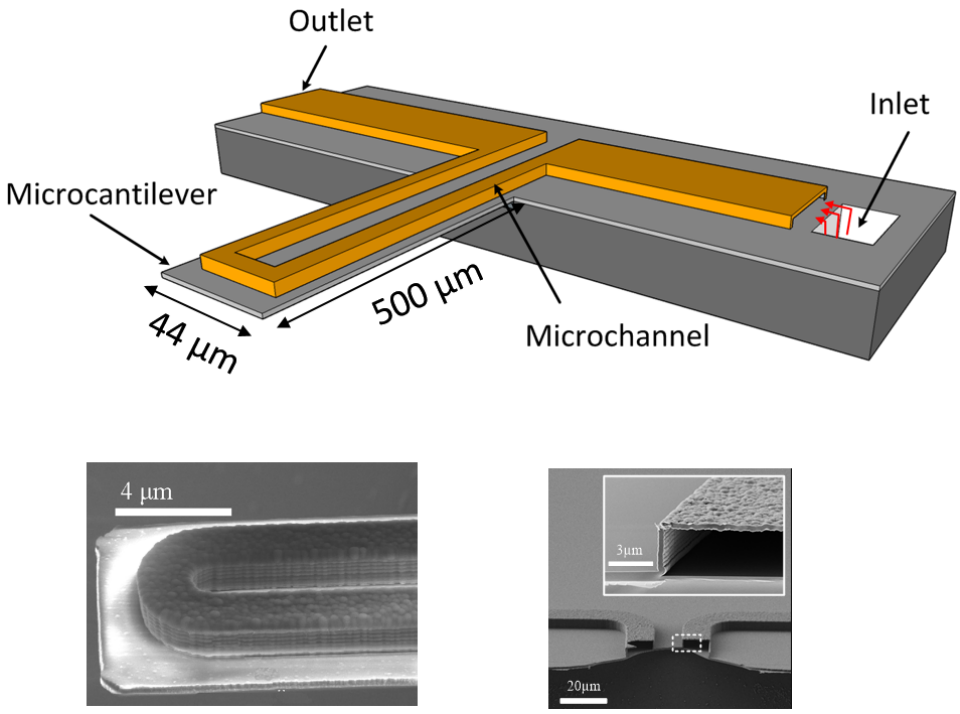

Figure 2.9 Schematic and SEM images of a hollow channel microfluidic cantilever.

2.4 Summary

Based on various targets, we designed and selected corresponding sensing molecules which have high selectivity and much improved reliability. According to different transducer/sensing layer duos, we designed protocols to create stable and efficient interfaces. The sensing molecules with thiolated end can be directly immobilized on gold surface; while the other molecules are usually functionalized onto gold surface through linkers with thiol ends. The other end usually contains an amine group or a carboxyl group which can form an amide bond with peptide/protein sensing molecules. Due to their molecular weight and related steric effect, linkers with longer carbon chains are commonly used for larger sensing molecules, while short linkers are much preferred for smaller molecules like peptides. All the methodology developed are used in the sensor development in following chapters. Also, they can be used as guidelines for other sensors design and development.

Chapter 3. Screening Short Peptide Fragments from Class IIa Bacteriocins as *Listeria* Recognition Elements

"Detection of *Listeria monocytogenes* with short peptide fragments from class IIa bacteriocins as recognition elements", Azmi, S., Jiang, K., Stiles, M., Thundat, T., & Kaur, K., *ACS Combinatorial Science*, **2015**, 17(3), 156-163. **(Cover Feature)**

3.1 Introduction

Rapid, sensitive, and specific detection of pathogenic bacteria using culture-independent methods is critical for monitoring food, the environment, and patients in clinical settings. In general, the conventional culture-based methods for detecting and enumerating bacteria are labor-intensive and time-consuming.[142] On the other hand, rapid methods, like immunoassays and polymerase chain reaction (PCR), are expensive, require state-of-the-art infrastructure, and often require sample pretreatment.[11,143,144] Pathogenic bacteria like Listeria monocytogenes are widely found in nature, such as soil, stream water, sewage, plants, and food, and have a mortality rate approaching 25%.[145,146] Detecting such pathogens in a timely fashion at low-levels, therefore, remains critical.

Several biosensor platforms have been recently developed that utilize a recognition element, such as an antibody, aptamer, or peptide for sensing, and the binding of these sensing moieties to bacteria is read through a transducer in real time. Antibody-based platforms have been popular due to their high affinity and specificity; however, these biomolecules lack stability under harsh conditions and can be expensive.[147,148] In contrast to antibody and oligonucleotide probes, peptides are intrinsically more stable in harsh environments, easier to synthesize, and exhibit broad activities and affinities against wide range of bacterial strains.[149–152] We have explored the viability of using Leucocin A (LeuA), a naturally occurring antimicrobial peptide (AMP) that displays potent activity against Listeria strains (minimum inhibitory concentration or MIC ~0.1 nM)[153,154] as a molecular recognition element in biosensor platforms. Using a LeuA-based platform, we selectively detected L. monocytogenes from other Gram-positive strains at a concentration

of 10^3 cfu/mL.[152] LeuA belongs to class IIa bacteriocins that are characterized by a conserved disulfide bond and a YGNGV sequence near the N-terminus and with an amphiphilic helical C-terminal domain.[154,155] Class IIa bacteriocins possess a narrow activity spectrum, with high potency (typically active in the nanomolar range) against specific Gram-positive strains including *Listeria*, and act by a receptor-mediated mechanism on the target bacterial cells.[156] Such potent activity is presumably achieved by a specific binding interaction of the peptides with membrane-localized proteins of the mannose phosphotransferase system (man-PTS) of the target cells.[157,158] The expression levels of the receptor on the target bacterial surface dictate the activities of class IIa bacteriocins from one strain to another.[159]

Peptide-functionalized microcantilever-based systems are an ideal platform for developing miniature sensors, as the presence of a peptide makes bacterial detection highly sensitive, specific, and label-free due to the specific interaction between peptide and bacteria.[160–162] For chemical and biological sensing, one side of a cantilever is coated with a thin film of gold and functionalized with molecular recognition agents such as antibodies or peptides to make it chemically specific. When target molecules or cells bind to the recognition agents, the change in surface energy results in cantilever deflection, which can be detected with different readouts, such as optical beam deflection, capacitance, or piezoresistivity. The sensitivity and reproducibility of a cantilever's bending response depends on the uniformity of the immobilized functional layer as well as the cleanliness of the sensing surface.[163–166] For class IIa bacteriocins, the C-terminal domain determines the target cell specificity.[155] Therefore, we hypothesized that small peptide fragments derived from the C-terminal region of class IIa bacteriocins[167,168] may bind Listeria strains with the same

specificity as that of the native full-length sequences and that a self-assembled monolayer (SAM) of small peptides on a gold microcantilever may serve as a potential biosensor platform for Listeria detection.

Accordingly, in this study, we screened a library of peptide fragments (14-residue) derived from native bacteriocins to identify the specific recognition elements from three class IIa bacteriocins, namely, Leucocin A (LeuA), Pediocin PA1 (PedPA1), and Curvacin A (CurA) (**Figure 3.1**). Several fragments from the C-terminal domain displayed high binding toward pathogenic Gram-positive bacteria, including *L. monocytogenes, Enterococcus faecalis,* and *Staphylococcus aureus*. Microcantilevers coated with gold and functionalized with a high-affinity peptide fragment, Leu10, showed a much higher deflection signal upon Listeria binding compared to that from microcantilevers functionalized with low-affinity fragments or a blank microcantilever (no peptide). In addition, MCL functionalized with a high-affinity peptide fragment showed a similar deflection and response time as that of full-length LeuA upon *Listeria* binding. This study highlights the potential of short peptide-based platforms in the development of biosensors to detect pathogenic bacteria.

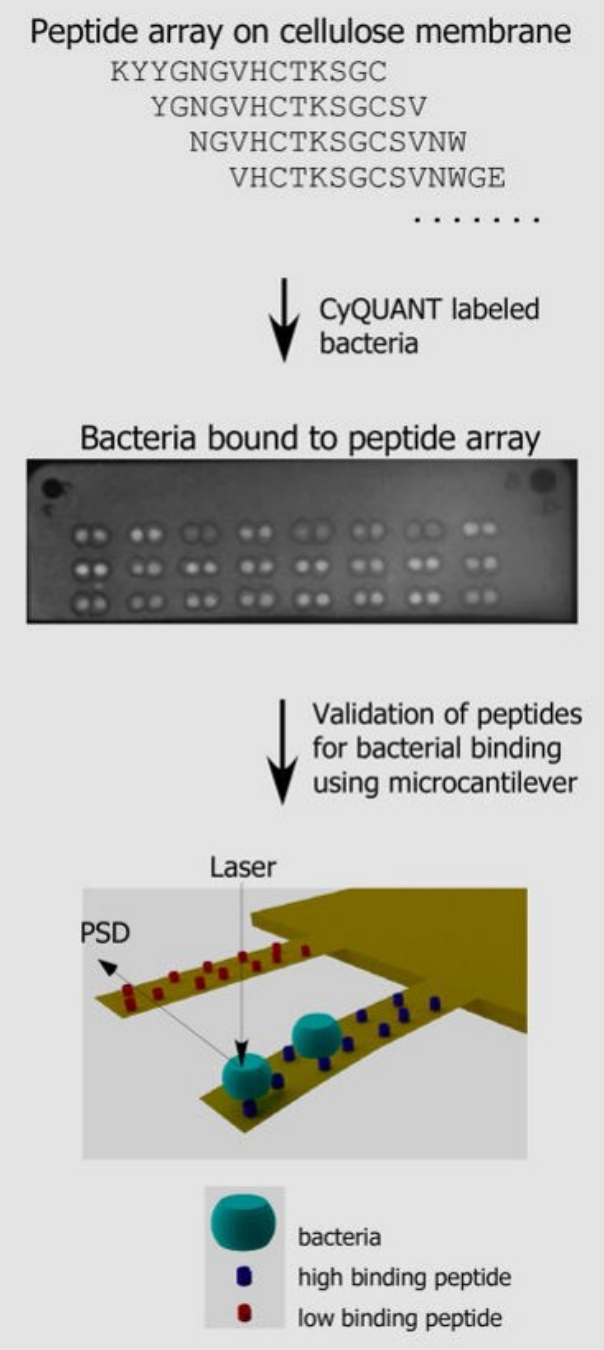

Figure 3.1 Schematic illustrating the steps used for screening and validating peptides with specific binding toward Gram-positive *L. monocytogenes*. PSD: Position sensitive detector.

3.2 Experimental Procedures

3.2.1 Materials

All reagents and solvents were of analytical grade and used as received with no further purification. Five bacterial strains, pathogenic (level II) and nonpathogenic, namely, *L. monocytogenes* (ATCC 19116 and ATCC 43256), *L. mesenteroids* (or UAL 280), *S. aureus* (ATCC 13565), and *E. faecalis* (ATCC 19433), were used in this study. All strains were obtained from the cell bank of CanBiocin, Inc. (Edmonton, AB, Canada) and were sub-cultured in their respective appropriate media, like APT or LB broth.

3.2.2 Peptide Array Synthesis

A peptide array library comprising 24 short peptide sequences (each 14 amino acids long) was synthesized in duplicate on a cellulose membrane using SPOT synthesis **(Figure 3.2)**.[169] Short peptide sequences were derived from the sequence of full-length class IIa bacteriocins Leucocin A, Pediocin A, and Curvacin A. Briefly, from the full-length Leucocin A, 13 peptides of 14 amino acids in length, skipping two amino acids, were derived, and six and five peptides were derived from the central amphipathic α-helical region of Pediocin A and Curvacin A, respectively. The peptide array was synthesized on a PEG-500-derivatized cellulose membrane with a free amino terminal group using a semiautomatic robot AutoSpot ASP222 (Intavis AG, Germany), as described in Appendix.[170,171]

Bacteriocin	Amino acid Sequence
Leucocin A	KY**YGNGV**HCT KSGCSVNWGE AFSAGVHRLA NGGNGFW
Pediocin PA1	KY**YGNGV**TCG KHSCSVDWGK ATTCIINNGA MAWATGGHQG NHKC
Curvacin A	ARS**YGNGV**YCN NKKCWVNRGE ATQSIIGGMI SGWASGLAGM

Fragment #	Fragment (14-mer) Sequence
Leu 1	KY**YGNGV**HCTKSGC
Leu 2	**YGNGV**HCTKSGCSV
Leu 3	**NGV**HCTKSGCSVNW
Leu 4	**V**HCTKSGCSVNWGE
Leu 5	CTKSGCSVNWGEAF
Leu 6	KSGCSVNWGEAFSA
Leu 7	GCSVNWGEAFSAGV
Leu 8	SVNWGEAFSAGVHR
Leu 9	NWGEAFSAGVHRLA
Leu 10	GEAFSAGVHRLANG
Leu 11	AFSAGVHRLANGGN
Leu 12	SAGVHRLANGGNGF
Leu 13	AGVHRLANGGNGFW
Ped 1	SVDWGKATTCIINN
Ped 2	DWGKATTCIINNGA
Ped 3	GKATTCIINNGAXA
Ped 4	ATTCIINNGAXAWA
Ped 5	TCIINNGAXAWATG
Ped 6	IINNGAMAWATGGH
Cur 1	KCWVNRGEATQSII
Cur 2	WVNRGEATQSIIGG
Cur 3	NRGEATQSIIGGXI
Cur 4	GEATQSIIGGXISG
Cur 5	ATQSIIGGXISGWA

Figure 3.2 Peptide library derived from different class IIa bacteriocins. In all, 24 peptide fragments (14-mers) were derived from Leucocin A (N to C), Pediocin PA1, and Curvacin A by overlapping 12 amino acids and skipping two amino acids. From Pediocin PA1 and Curvacin, peptide fragments were derived from the C-terminal region only (15-38 and 14-35, respectively). The YGNGV motif (bold) and residues in the C-terminal domain forming amphipathic α-helix (red) in the native peptide are highlighted. All peptides are conjugated to cellulose membrane from the C-terminus via a β-alanine (Z) linker.

3.2.3 Peptide Array-Cell Binding Assay

Bacteria were labeled with CyQUANT dye before performing the cell binding assay with the peptide array membrane. The peptide array membrane was incubated with the labeled bacteria, and, after washing, the net fluorescence intensity of each peptide spot due to bound bacteria was quantified using a Kodak imager, as described in the Appendix.

3.2.4 Peptide Synthesis and Purification

The three selected peptide fragments (Leu10, Leu13, and Ped3) were synthesized by an automated synthesizer (Tribute, Protein Technology Inc., USA) utilizing solid-phase methods, as described in the appendix.[116]

3.2.5 Circular Dichroism

The circular dichroism (CD) spectra of the peptides were recorded on an Olis CD spectropolarimeter (GA, USA) in 40% TFE (40% TFE in water, v/v). The spectropolarimeter was calibrated routinely with 10-camphor sulfonic acid. The samples were scanned at room temperature (~25 °C) with the help of a capped quartz cuvette with a 0.2 cm path length at a wavelength range of 250–185 nm. The final concentration for CD measurements was 0.3 mg/mL (~200 μM) for each peptide. The baseline of blank (40% TFE) was subtracted from the peptide sample reading. An average of 4–6 scans were taken for each sample with a scan speed of 20 nm/min and a data interval of 1 nm.

3.2.6 Peptide Immobilization on Microcantilever System (Gold Surface)

Gold-coated silicon microcantilever (MCL) arrays, 500×90×1 μm^3 (Micromotive Octosensis), were obtained from IBM Research Laboratory (Rüschlikon, Zurich). The gold-coated MCL array was rinsed with aliquots of ethanol followed by Piranha cleaning for 3 min and finally with DI water and ethanol rinse before functionalization. The backside of the MCL was passivated by immersing the array into a bis(triethoxysilylpropyl) poly(ethylene oxide) ethanol solution for 20 min followed by rinsing and drying in air. After passivation, the microcantilever array was kept in 0.01 M cysteamine hydrochloride in a phosphate buffer solution (8×PBS) at pH 8.1 for 6 h at room temperature for the formation of a self-assembled monolayer (SAM) of cysteamine linker. After rinsing with ethanol and PBS, MCL arrays were immersed into a 1× PBS solution at pH 7.4 containing class IIa bacteriocin fragment peptides (Leu10, Leu13, or Ped3; 1.0 mg/mL). EDC (0.2 M) and NHS (0.05 M) were also added to the PBS solution to activate the carboxyl group (−COOH) of the peptides. The formation of amide bond between the cysteamine and the peptides led to immobilization of the peptides. The cantilever array was functionalized using a dip-in method.[172] By dipping the cantilever beam into the peptide solutions, the MCL array was selectively functionalized. The unmodified cantilevers served as the reference in bacterial detection. Prior to the deflection test, the MCL array was removed from the solution and rinsed with copious amounts of PBS to remove any physically adsorbed materials. The array was then dried with nitrogen and setup in the flow cell of the detection system.

3.2.7 Microcantilever Deflection System and Detection

The detection of *L. monocytogenes* by the peptide-functionalized MCL array is based on the concept of changes in intrinsic stress leading to cantilever bending. All of the experiments were performed in 1× PBS (pH 7.4) solution with a constant flow rate of 5 mL/h. A syringe pump was used to introduce the mobile phase (PBS) and the bacterial solution into the flow cell where the MCL array was located. Due to the constant flow, the microcantilever response from fluidic dynamics was also recorded. This was considered as background noise for the study of peptide-assisted bacteria detection using the MCL system. This noise was minimized by taking the differential signal between the functionalized beam and the reference beam. After a steady baseline was achieved, the bacterial sample solution was injected into the experimental system at the same flow rate of 5 mL/h. The response of each microcantilever bending was recorded as a function of time as well as the total volume of PBS and bacterial solution flowed through the system. Deflection of the cantilever array was measured by a position-sensitive detector (PSD) assembled with the homemade system.

3.3 Results and Discussion

3.3.1 Design of Peptide Library Derived from Class IIa Bacteriocins

Previously, we used full-length LeuA (37-mer) and a 24-residue fragment from the C-terminal region of LeuA to show that these peptides bind specifically to Gram-positive strains like *Listeria* and show much less binding toward other Gram-positive

bacteria.[116] These peptides do not bind to Gram-negative bacteria such as *Escherichia coli*. The binding between peptide and bacteria was detected using fluorescence microscopy (using labeled bacteria) or impedance spectroscopy (label-free detection).[152] Although fluorescence microscopy allowed detection of about 73 bacteria/100 μm^2, we were able to detect bacteria at a concentration of 1 cell/μL or 10^3 cfu/mL using the impedance method.

Here, we have designed a peptide library with 14-mer overlapping sequences from three class IIa bacteriocins, namely, LeuA, PedPA1, and CurA (**Figure 3.2**). Thirteen short fragments (Leu1-Leu13) were derived from the full-length LeuA (37-mer). In addition, six Pediocin fragments (Ped1-Ped6) and five Curvacin fragments (Cur1-Cur5) were derived from the C-terminal regions of PedPA1 (15-38) and CurA (14-35), respectively. For the latter two bacteriocins, fragments were derived from the C-terminal region to limit the number of peptides in the library.

A library of 24 peptides in duplicate was synthesized in an array format on a cellulose membrane derivatized with poly(ethylene glycol)-500 (PEG-500) with free amino groups (**Figure 3.2**). Peptides were conjugated to the membrane's amino groups through the C-terminal carboxylate, as we found previously that peptides immobilized from the C-terminus led to a higher number of bound bacteria (81 bacteria/100 μm^2) compared to that with peptide immobilized from the N-terminus (73 bacteria/100 μm^2).[173] Following peptide array synthesis, the membrane was incubated in DMSO (20%) for 10-12 h at 4 °C and then overnight at room temperature to form intramolecular disulfide bonds between the cysteines present in some sequences (Leu1-Leu5).

3.3.2 Screening of Peptide Fragments through a Whole Cell Binding Assay

Peptides displaying high binding to pathogenic bacteria, especially *Listeria* strains, were screened by incubating the peptide library with several Gram-positive strains. Bacteria were labeled with the fluorescent CyQUANT dye, by incubating with the dye for 2 h in dark, prior to incubating with the peptide library. CyQUANT was selected for bacteria labeling due to its low intrinsic fluorescence and high fluorescence and the quantum yield on nucleic acid binding compared to that of other dyes like DAPI and CFSE.[170,174] The relative binding affinities of peptide fragments were determined through the net fluorescence intensity of the bound bacteria measured with a fluorescence Kodak imager (**Figure 3.3**).

The library was incubated with individual bacterial strains, and the binding was recorded followed by regeneration of the peptide array to remove all of the bound bacteria. The binding experiment was repeated once. The membrane was reused for up to 6-8 regenerations. After the binding assay was performed with five different bacterial strains, the binding to peptides was compared by plotting the fluorescence of the bound bacteria to each peptide fragment in the library, as shown in **Figure 3.3**. Several fragments from the C-terminal domain of LeuA (Leu7-Leu11), PedPA1 (Ped1-Ped3), and CurA (Cur1-Cur4) showed good binding to the bacterial strains. LeuA fragments displayed higher binding compared to that of PedPA1 and CurA, as shown by the fluorescence intensities of the bound bacteria. Moreover, Leu10 displayed the highest binding toward all of the pathogenic strains. In order to further validate the differential affinity of the peptide fragments, we selected two peptide fragments, Leu10 (high binding) and Ped3 (relatively

lower affinity peptide), for subsequent experiments. Leu13 was selected as a negative control peptide that demonstrated no binding toward any of the tested bacterial strains.

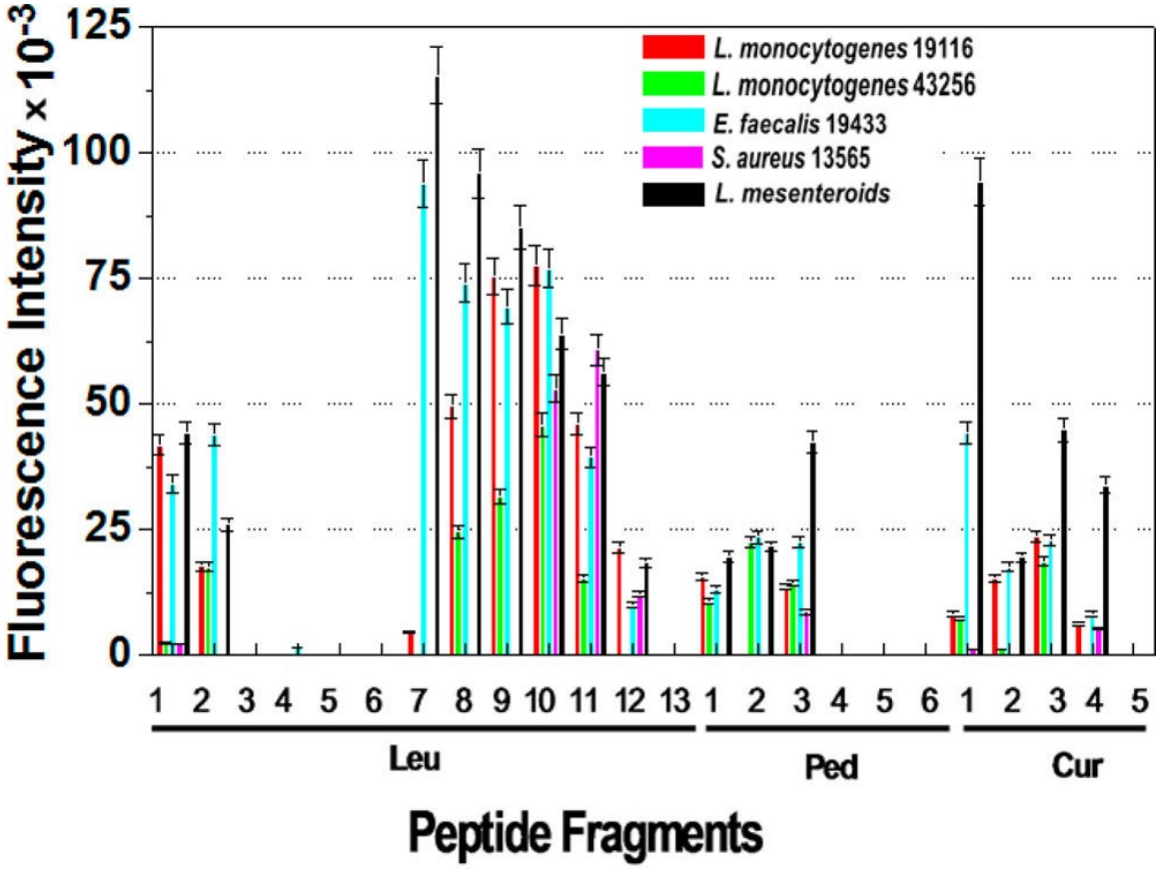

Figure 3.3 Screening of peptide fragments showing high binding to *Listeria monocytogenes*. A peptide array library on a cellulose membrane was incubated with fluorescently labeled bacterial cells (OD 0.05) for 3h followed by extensive washing. Fluorescence intensity of bound bacterial cells was measured using a Kodak imager, with excitation and emission at 467 and 535 nm, respectively. The results presented here are mean fluorescence intensity ± SD. Red, *L. monocytogenes* ATCC 19116; green, *L. monocytogenes* ATCC 43256; blue, *E. faecalis*; pink, *S. aureus*; and black, *Leuconostoc mesenteroids* (or UAL 280).

Previously, we used cellulose membrane to screen peptides for mammalian cell line binding.[170,171] Here, we show that a peptide library on a cellulose membrane can also be used to screen peptides with affinity toward bacterial cells. In general, functionalized cellulose membrane is an ideal platform to evaluate a library of peptides (or other synthetic molecules) for whole cell binding or binding with biomolecules like proteins, peptides, and oligonucleotides.[169,175,176] Kaga and co-worker utilized a membrane-derived peptide array library to identify an octamer peptide that induces caspase-dependent cell death, and this study was performed through direct interaction of the membrane-adhered peptide with the cells.[177] Similarly, Hilpert and Hancock used a membrane array library to dig out a highly active antimicrobial peptide from already known Bac2A.[178] In this study, the authors synthesized 100 analogs of Bac2A on the cellulose membrane and identified several antimicrobials that performed better than the parent through monitoring luciferase activity of transformed bacterial cells in an antimicrobial activity assay. However, in these studies, the authors punched out the peptide spots into a 96-well plate to perform the antitumor or antimicrobial activity. We have used the intact peptide array library on the membrane to study peptide–cell binding interactions.

3.3.3 Secondary Structure of Select Peptides in Solution

To understand the structural basis of Leu10's higher and selective binding to *Listeria* strains, we used circular dichroism (CD) spectroscopy to study the solution conformation of selected peptides. CD spectra of Leu10 were compared to those of Ped3 and Leu13 in 40% TFE (**Figure 4.4**). The CD spectra of fragment Leu10 showed typical negative minima at 207 nm ($\theta = -5.0 \times 10^3$) and 222 nm and a positive band at 195 nm,

suggesting a helical conformation. On the other hand, the spectra of Ped3 exhibited a negative minimum at 208 nm, suggesting a partial helical conformation or transformation from a β-sheet to a helical shape in the presence of TFE. Finally, Leu13 displayed a negative band at ~195 nm, which is characteristic of a random coil. The CD spectrum of Leu10 resembled that of native LeuA, which is a helical peptide, as observed by CD and NMR spectroscopy.[179,180]

Peptide fragment	Sequence (14-mer)
Leu 10	H_2N-G**E**AFSAGVH**R**LANG-$CONH_2$
Leu 13	H_2N-AGVH**R**LANGGNGFW-$CONH_2$
Ped 3	H_2N-G**K**ATTCIINNGAXA-$CONH_2$

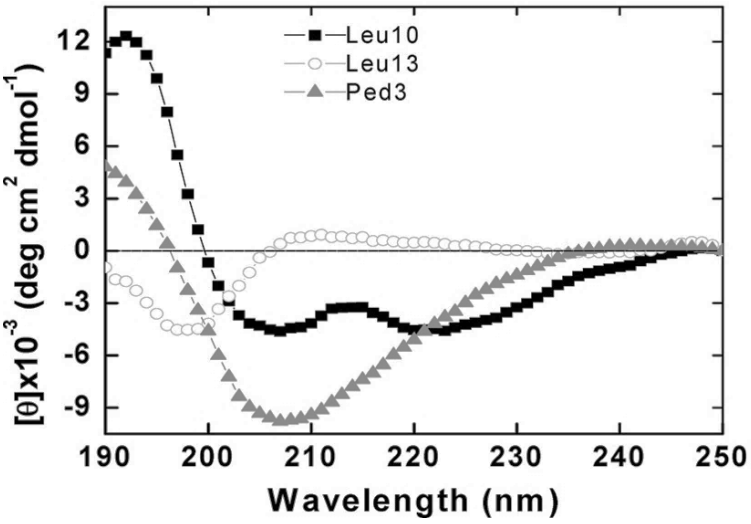

Figure 3.4 CD spectra of peptide fragments (Leu10, Leu13, and Ped3) in 40% TFE/water. The concentration of peptides was 0.3 mg/mL (~200 μM).

The CD spectrum of native LeuA shows a negative band at 206 nm ($\theta = -10.5 \times 10^3$) and a negative shoulder near 220 nm ($\theta = -6.0 \times 10^3$).[168] Usually, it has been seen that helical conformations of a peptide play an important role in its interaction with a membrane

receptor or antimicrobial activity.[181,182] The presence of a helical conformation in Leu10 and not in Ped3 and Leu13 confirms our conjecture that helical conformation may play an important role in the differential affinity of these peptides toward Gram-positive bacteria.

3.3.4 Detection of Bacteria by Deflection of Peptide Coated Microcantilevers

Peptide fragments identified from library screening were evaluated using peptide-functionalized microcantilevers (MCL). A deflection in MCL upon bacterial binding was used for the detection of *L. monocytogenes* due to the specific interaction between peptide and bacteria. MCL deflection, which corresponds to the absorption of cells (bacteria) or molecules, can be accurately measured by a position-sensitive detector (PSD) and is described by Stoney's formula for electroplated metal films.[183] For MCL systems, where the secondary coatings are quite thin compared to the thickness of the cantilever, a no-slip boundary condition at the substrate–film interface can be assumed and the stress relaxation due to substrate deformation is negligible, so the deflection of the free end of a microcantilever, δ, can be related to differential surface stress, Δ*s*, by

$$\Delta s = \frac{Et^2}{3L^2(1-\nu)}\delta \qquad (3-1)$$

where *E* is Young's modulus for the substrate (Si, 155.8 GPa), *t* is the thickness for the cantilever (1 μm), *L* is the length of the cantilever (500 μm), and *v* is Poisson's ratio (Si, 0.28). This formula (Eq 3-1) was used to determine the surface stress differential upon bacteria binding. In addition, in our system, an optical beam deflection-based response readout was used. There are several procedures to readout the response of a microcantilever

such as optical beam deflection, capacitance, piezoresistivity, piezoelectricity, and interferometry. Optical beam deflection-based response readout delivers the highest sensitivity and is used in most microcantilever-based biochemical applications.[184]

The three peptide fragments, Leu10, Ped3, and Leu13, were separately immobilized onto MCLs. The binding behavior of these fragments was compared with that of full-length LeuA. MCL coated with cysteamine alone (linker) was used as a blank reference. The sample flowed through the MCL system at a constant flow rate of 5 mL/h. First, buffer (PBS, 50 mM, pH 7.4) was allowed to flow through the system to establish a stable baseline, followed by the introduction of the sample solution containing *L. monocytogenes* at a concentration of 10^5 cfu/mL. As shown in **Figure 3.5**, we observed that the response or signal builds over time after the introduction of the bacterial sample and that the signal saturates in about 20 min when the peptide–cantilever surface reaches maximal bacterial binding. The deflection on the Leu10-functionalized MCL was measured at around 100 nm, which refers to a surface stress of 29 mN/m. In comparison, the LeuA-functionalized sensor showed a response of about 120 nm, indicating similar binding processes between LeuA and *L. monocytogenes* as well as Leu10 and *L. monocytogenes*. On the other hand, the response of the Ped3-functionalized sensor to *L. monocytogenes* was significantly reduced. The deflection observed for Ped3 was about 40 nm, whereas Leu13 showed no significant response to *L. monocytogenes*. Furthermore, the response time for Leu10 MCL is comparable to that of the LeuA MCL, suggesting that Leu10 is an optimum peptide candidate for *L. monocytogenes* detection.

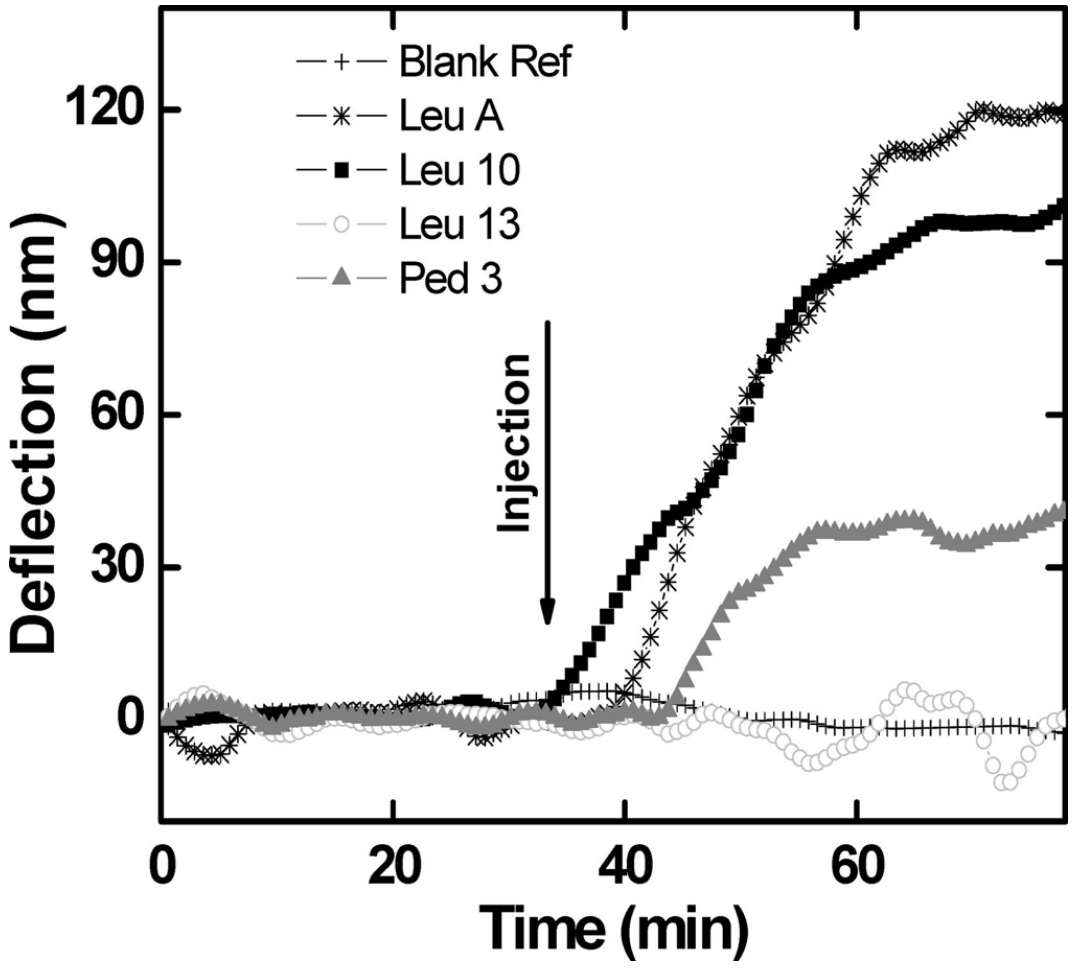

Figure 3.5 Deflection of microcantilevers functionalized with LeuA derived short peptides upon *L. monocytogenes* ATCC 19116 binding. *L. monocytogenes* was injected at a concentration of 105 cfu/mL (in PBS) at a flow rate of 5 mL/h. LeuA is a 37-residue full-length antimicrobial peptide, whereas Leu10, Leu13, and Ped3 are 14-residue peptide fragments.

We have used peptide-conjugated microcantilevers with optical beam deflection for detecting the specific interaction between the sensor and bacteria with high sensitivity. Such a nanomechanical platform offers advantages over other biosensor methods such as surface plasmon resonance (SPR), quartz crystal microbalance (QCM), and electrochemical methods, like impedance, admittance, or capacitance. SPR real-time detection is based on a change in the refractive index when an analyte interacts with the recognition surface. It is highly sensitive, but SPR detection may require pretreatment of the sample to first isolate bacteria, e.g., using antibodies.[185] Bouguelia and co-workers used SPR to detect low levels of *Salmonella* and other Gram-negative pathogens.[186] However, their culture–capture–measure (CCM) approach utilizes monoclonal antibodies immobilized on an SPR surface, and the detection takes place in several hours (>6 h). QCM, which is a mass-based method, has not yet been optimized for high sensitivity.[187] Similarly, electrochemical methods like impedance spectroscopy that provide a fast readout are still in the early stages of development.[149,152,188]

3.4 Conclusions

Peptides function as specific recognition elements for the detection of a variety of biomolecules and cells. Using a synthetic peptide array library on a cellulose membrane, we screened short peptide fragments for high and specific binding to *L. monocytogenes*. Peptide fragments were derived from three potent anti-Listerial peptides that belong to class IIa bacteriocins. Several fragments from the C-terminal region showed high-to-moderate binding to five Gram-positive bacteria. Fragment Leu10 (GEAFSAGVHRLANG), which displayed the highest relative binding to bacteria

compared to that of other fragments, was chosen for validation using a microcantilever (MCL)-based technique. MCLs were functionalized with fragments Leu10, Ped3, Leu13 or with full-length LeuA. The Leu10-functionalized MCL was able to detect *Listeria* with the same sensitivity as that of the LeuA-functionalized MCL. It is interesting to note that the binding response of a short fragment was similar to that of the full-length peptide. However, the antibacterial activity of this class of peptides is dramatically reduced even with a small change in the sequence, and short sequences are generally inactive.[168,189] In addition, class IIa bacteriocins have a well-folded C-terminal amphipathic helix that is considered to be important for its target bacteria binding and antimicrobial activity. Leu10, derived from the C-terminal region of LeuA, folds into a helical conformation, suggesting that Leu10 may possess a similar binding mechanism as that of full-length bacteriocins to the target bacteria. The study highlights the use of peptide array membranes to screen short fragments from antimicrobial peptides with specificity toward pathogenic bacteria and demonstrates that such peptides can be used as recognition elements in biosensor development.

Chapter 4. Investigation of pH-induced Protein Conformation Changes by Nanomechanical Deflection

"Investigation of pH-induced protein conformation changes by nanomechanical deflection", Thakur, G., Jiang, K., Lee, D., Prashanthi, K., Kim, S., & Thundat, T. *Langmuir*, **2014**, 30(8), 2109-2116

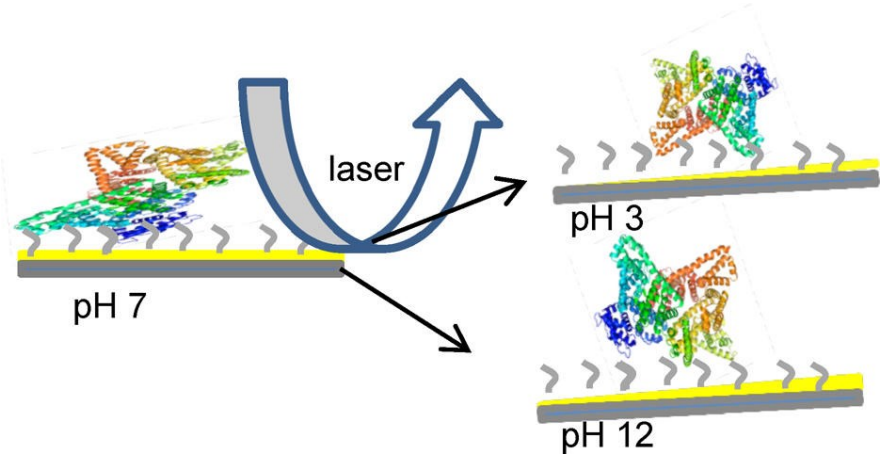

4.1 Introduction

Conformational and orientation transitions in proteins are critical factors which impact various biological processes. Many spectroscopic techniques are widely used to understand the conformational changes of proteins such as circular dichroism (CD),[190] fluorescence spectroscopy,[191] nuclear magnetic resonance (NMR),[192] and Fourier transform infrared (FTIR) spectroscopy.[193] Most of these methods are solution based i.e., they require the biomolecules dissolved in a solvent. In the past decade, various biosensing techniques involving solid-liquid interface such as quartz crystal microbalance (QCM),[194,195] surface plasmon resonance (SPR),[196] microcantilever sensors,[197] atomic force microscopy (AFM),[198] and impedance spectroscopy[199] have been developed. These techniques which use surface immobilized biomolecules require information on conformational changes of biomolecules to understand the sensing phenomena on the surface.

Microcantilevers have attracted attention due to their sensitivity and versatility as a sensing platform as well as a label-free detection technique.[197,200–203] Several antibody-antigen assays investigated using microcantilever sensors suggested that molecular binding-induced surface stress is a sensitive detection signal that is ideal for liquid environment.[203–210] These signals are basically induced due to molecular binding to receptors or proteins which indirectly induces conformational changes in the receptors or proteins. However, to develop a cantilever-based biosensor that can provide more quantitative information, one needs to understand the basic mechanisms involved in surface stress generation, which would receptor specific. To understand the binding-induced stress generation on microcantilever systems, it is important to understand the orientation and conformational

changes of receptors or proteins which act as binding sites for the target analytes.[211–214] Protein conformational changes have significant implications in the development of biosensors. In addition, the surface stress of a microcantilever can also be influenced by variations in pH of the solution. The deflection of a bimaterial microcantilever changes as a function of pH because of the pH-induced variations in the surface charges of one of its surfaces. A microcantilever can be made into a sensitive pH sensor based on surface stress change.[215–217]

Human serum albumin (HSA) is a widely studied protein that accounts for more than 50% of total plasma protein concentration with the molecular weight of 65 kD.[117–119] HSA is known to undergo pH-dependent conformational isomerization. At physiological pH of 7.4, the HSA is identified as a heart-shaped molecule existing in normal (N) form. However, at pH greater than 9, the transition takes place to basic (B) form, where it is believed that the heart shaped structure is changed into an ellipsoid. At acidic pHs below 4.7, it is believed to exist in fast (F) form.[120,121]

Most of the previous studies on conformational analysis of biomolecules, specifically proteins, used the indirect methodology to find conformational change.[211,213,214] Here, we investigated the direct conformational change of protein (HSA) on a microcantilever surface by variation of pH. Two complementary techniques, microcantilever array and surface plasmon resonance sensing, were used to investigate the conformational change of immobilized HSA on the gold surface.

4.2 Materials and Methods

4.2.1 Materials

Commercially available silicon microcantilevers (Micromotive Co., Mainz, Germany) were used in all the experiments. The dimensions of the cantilever were 500 µm in length, 90 µm in width, and 1µm in thickness. All chemicals used including NaCl, Na_2PO_4, 1-ethyl-3-(3-dimethyl aminopropyl)carbodiimide (EDC), N-Hydroxysulfosuccinimide (Sulfo-NHS) and 2-(N-morpholino) ethanesulfonic acid (MES) were purchased from Sigma Aldrich. The ligands carboxy-PEG $_{12}$-lipoamide (PEG_{12}-CL), and solvents such as ethanol were purchased from Fisher Scientific. Deionized (DI) water with a resistivity of 18.2 $M\Omega \cdot cm^{-1}$ from Milli-Q-water purification system was used in all the experiments.

4.2.2 Preparation of denatured HSA

2mg/ml of HSA solution in PBS buffer was heated at 60 ° C for overnight and characterized using CD and FTIR spectroscopy (see Appendix).

4.2.3 Functionalization of the cantilevers and SPR sensor chips

Silicon microcantilevers were cleaned using piranha (H_2SO_4: H_2O_2 (3:1)) for 10 min, washed with plenty of deionized water and rinsed with ethanol. After air-drying, the freshly cleaned microcantilever was coated with a 5/50 nm Ti/Au layer using an electron-beam evaporator. The freshly coated microcantilevers were cleaned using UV-ozone cleaner for

3-5 hrs and rinsed with ethanol. Dried cantilevers were passivated with PEG-silane on backside. Gold side of the cantilever was functionalized by immersing in 1mM PEG_{12}-CL solution in PBS buffer (20 mM Na_2PO_4, 0.15 M NaCl) at pH 7.4 for 3hrs. After cleaning the microcantilevers and removing the excess reagent, activation of the carboxyl group was carried out by zero length crosslinking agent EDC and sulfo-NHS. The microcantilevers on the array were immersed in 0.2M EDC and 50 mM sulfo-NHS prepared in MES buffer (0.1M MES, 0.5M HCl) at pH 6 for at least 30 min and stirred at very low speed. Excess of the reagent was removed by washing the cantilevers in the buffer solution. Each of the activated microcantilevers was functionalized with HSA or denatured HSA for 2 hours leaving the rest of four cantilevers as references (**Figure 4.1A**). Hydroxyl amine was used to block the active sites on the reference cantilevers and unreacted active carboxyl moieties on the protein immobilized cantilevers.

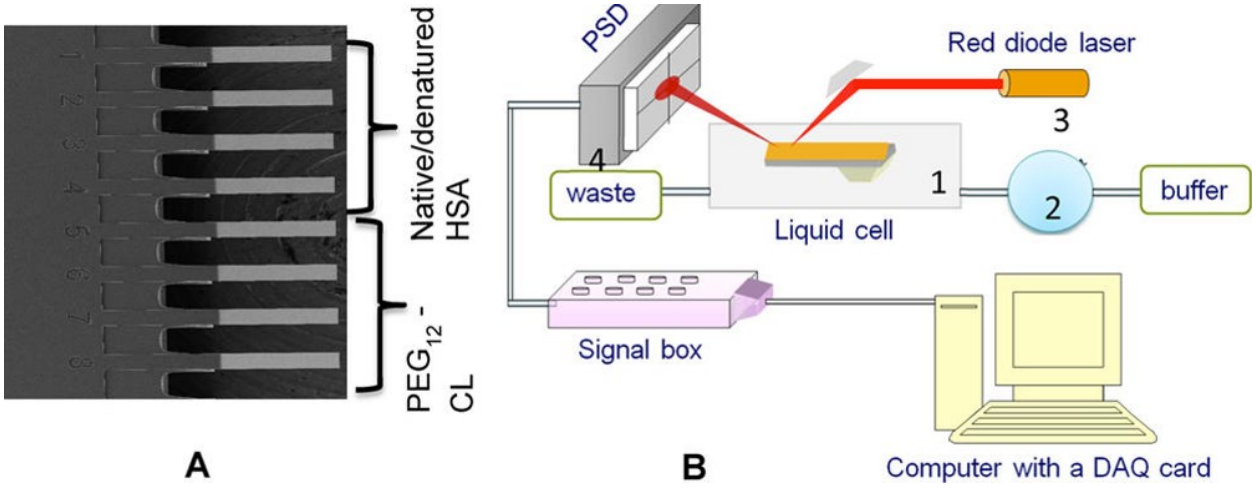

Figure 4.1 Image of microcantilever array and schematics of the microcantilever deflection detection system: A) Four cantilever beams are coated with HSA and the rest of them are coated with PEG_{12}-CL as references. B) Schematic drawing of the cantilever deflection sensing system: 1) the liquid cell with a cantilever. 2) Buffer injection with a syringe pump3) Red diode laser 4) Readout system connected with PSD.

SPR sensor chips were functionalized in the same manner. Glass sensor chips with 50 nm Au coating were purchased from Biolin Inc. for SPR Navis system. After cleaning with piranha (*Caution!*), sensor chips were functionalized with PEG_{12}-CL to form a self-assembled monolayer (SAM) and then either native or denatured HSA was immobilized on the sensor surface using same chemistry as previously discussed for microcantilevers.

4.2.4 Cantilever deflection measurements

Deflection measurements were carried out using a homemade cantilever deflection sensing system with a liquid flow cell. The laser beam was focused on the cantilever's free end and the "compressive" (negative deflection, towards silicon side) and "tensile" (positive deflection, towards gold side) stresses of the cantilever were measured by monitoring the position of the reflected laser beam on a position sensitive detector (PSD). **Figure 5.1B** shows the experimental set-up for the cantilever deflection sensing system. The experiments were performed in a stainless-steel flow cell (Scentris, Veeco, Santa Barbara, CA). The PBS buffer solution (50 mM NaCl, 20 mM Na_2PO_4) was set to flow through the cell using a syringe pump and the flow rate was set at 5 mL/min. Stoney's equation[218,219] was used to determine surface stress.

$$\Delta\sigma = \frac{1}{3}\left(\frac{t}{L}\right)^2\left(\frac{E}{1-\nu}\right)\Delta z \qquad (5-1)$$

where L is the effective length, t is the thickness of the cantilever, E is Young's modulus, ν is Poisson ratio of Si, and Δz is the deflection of the cantilever.

4.2.5 SPR experiments

Conformational change of HSA was measured using a Navi-200 (BioNavis, Helsinki, Finland) instrument. SPR was operated at 25 ºC in a flow-through mode with a flow rate of 10 μL/min. The laser wavelength used is 760 nm.

4.2.6 Atomic Force Microscopy (AFM)

Multimode 8 atomic force microscope (Bruker, Santa Barbara, CA) was used for tapping mode imaging. The protein was immobilized on a silicon wafer coated with Ti/Au (5/50 nm). Freshly prepared samples were used for AFM conducted in air.

4.3 Results and Discussion

4.3.1 Characterization of surface

To achieve the required sensitivity and selectivity of a microcantilever sensor, it is very important to choose a right ligand to attach the receptor or protein to the cantilever surface. It is also important to characterize the functionalized surface to understand the properties and effectiveness of surface functionalization. The dithiolated ligand PEG_{12}-CL was used for HSA immobilization on the gold coated surface of the cantilever due to bidentate interaction mechanism in comparison to monothiolated ligands.[220] Moreover, it contains the PEG which is known to prevent bio-fouling and is a biocompatible ligand.[220,221] The characterization of the surface was achieved using AFM imaging. AFM of the self-

assembled PEG layer on gold surface showed that the SAM was organized with small islands on the surface[222] as presented in **Figure 4.2A**. PEG modified surface showed average height ranging from 5 ± 5 nm as shown in the histogram. Native HSA modified substrate showed a height up to 17 ± 5 nm (**Figure 4.2B**) and globular protein molecules were arranged in a circular fashion on the surface as shown in the AFM images. The radius of the HSA monomer in solution is 27 ± 0.35 Å,[223] whereas, the height of small circular features is 17 ± 5 nm. This suggests that these features are a cluster of protein molecules and not monomers. Denatured HSA did not show globular structures as seen through AFM images (**Figure 4.2C**) indicated by dashed circular marks. Denatured HSA showed characteristic features with an average height of 10 ± 3 nm.

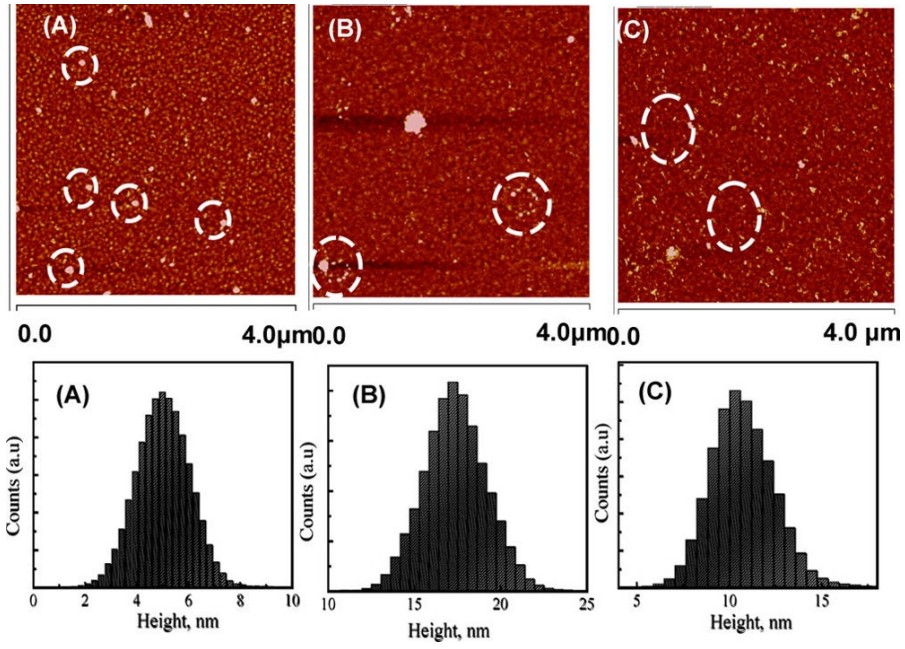

Figure 4.2 AFM images of immobilized gold substrate and corresponding histogram profiles A) CL-PEG$_{12}$ modified surface B) Native HSA immobilized surface C) Denatured HSA immobilized surface. Dashed circles in the images show specific features observed.

4.3.2 pH- dependent conformational change of native and denatured HSA

To understand the nature of surface stress on a cantilever, it is essential to use a reference cantilever for common mode rejection and analyze the signals as a differential deflection signal. pH-dependent conformational change of HSA was determined by switching the pH from 7 to 3 or 12 and then back to pH 7. Extraction of the differential deflection signals was achieved by taking the difference between average deflection signals of cantilevers modified with HSA an average deflection signal of cantilevers modified with PEG_{12}-CL SAM (**Figure 4.3**). To confirm the deflection signal is due to conformational change of HSA, we also performed control experiments by modifying cantilever array with denatured HSA and observed the differential deflection signal with respect to reference cantilevers coated with PEG_{12}-CL. Phosphate buffer with the total ionic strength of 0.1M was used with a variation of pH. The buffer strength was optimized to 50 mM sodium chloride and 20 mM dibasic sodium phosphate. Only a small amount of 0.1 M HCl or 0.1 M NaOH was used to decrease or increase the pH, respectively. A flow rate of 5mL/min was optimized and used for all the experiments and switching of buffer was done after reaching the baseline.

Figure 4.3A shows the differential deflection signal for conformational change of HSA by switching the buffer pH 7 to pH 3. The combination of various factors such as intermolecular interactions, electrostatic repulsion, attraction and steric effects results in bending of the cantilever as a change of ions or ionic strength.[212] Moreover, the orientation of protein molecules may alter under the different ionic environments resulting in bending of the cantilever. These results clearly demonstrate when the microcantilever array was

exposed to pH 3, due to protonation the charge on the protein surface was changed resulting in attractive protein-protein interactions causing the biomolecules to pack together (*pI* of HSA is 5.4).[120] The differential signal was approximately 200 ± 50 nm, which corresponds to a surface stress of 48 ± 12 mN/m. Switching the pH to 7 again changes the environment of the protein molecules and there is a relaxation of stress, which means the biomolecules change their orientation and conformation on the surface and try to reorient back to the same conformation. The relaxation of surface stress for native HSA takes approximately 3000 sec for reversing the conformational change. To confirm that this is a genuine change of conformation of the protein we performed same experiments with cantilever array immobilized with denatured HSA. **Figure 4.3B** shows the change in differential bending signal of denatured HSA with respect to the reference. Upon injecting buffer solution with pH 3, we observed a differential signal of 27.9 ± 20 nm that correspond to surface stress of 6.6 ± 7.2 mN/m. Relaxation of surface stress was observed in approximately 5000 sec. This result shows that cantilever deflection due to acidic pH change was dependent on the cantilever immobilization with native or denatured HSA.

Figure 4.3C shows the differential signal of native HSA with respect to PEG_{12} -CL as reference upon switching the pH of the buffer solution from 7 to 12. Tensile stress was observed with maximum differential bending of 75 ± 30 nm, which corresponds to surface stress of 18.0 ± 7.2 mN/m. Upon switching back to pH 7 the biomolecules try to reorient back to the same position in approximately 2000 s. Whereas, for denatured HSA (**Figure 4.3D**) minimal differential bending was observed at approximately 15 ± 5 nm (resulting in the surface stress of 3.6 ± 1 mN/m). An interesting observation was the stabilization of deflection signal was faster in the case of native HSA in comparison to denatured HSA.

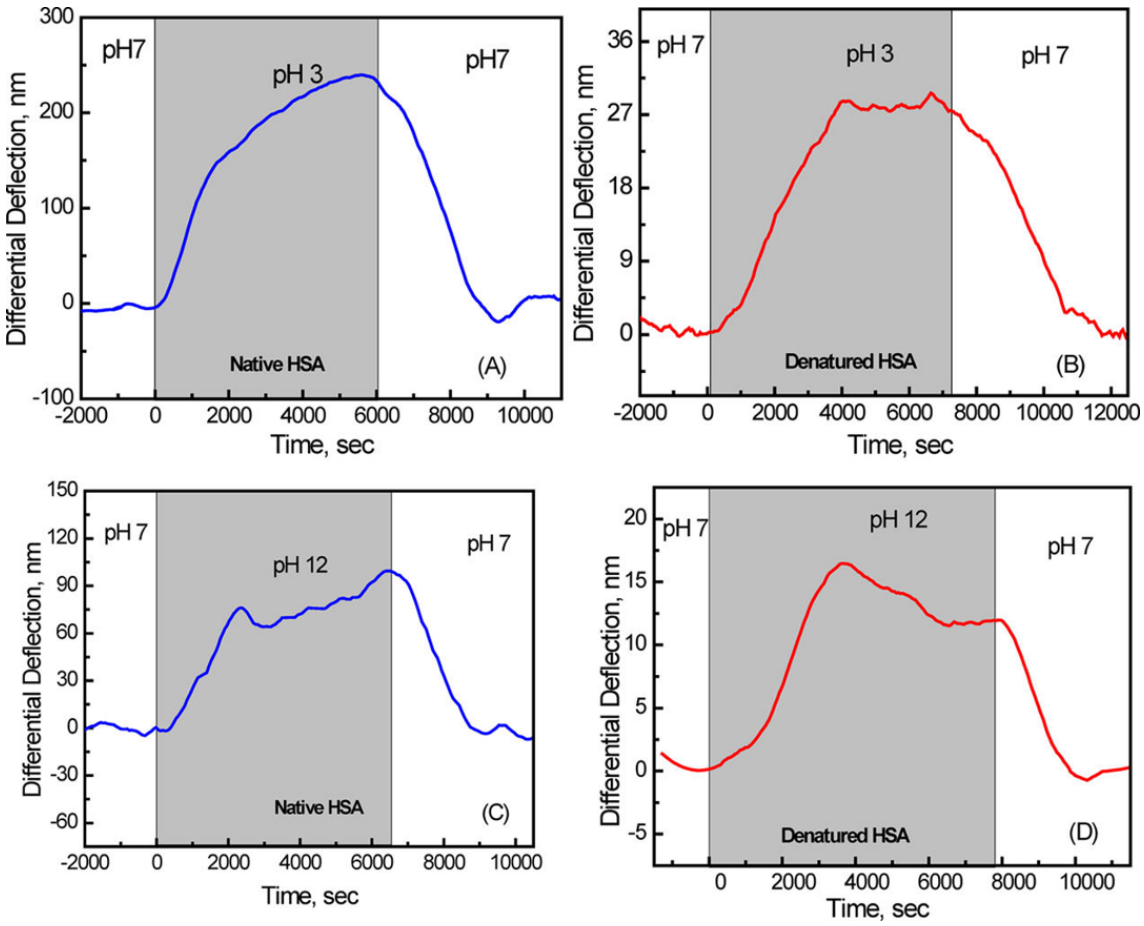

Figure 4.3 Differential deflection signal of HSA immobilized cantilevers with respect to reference cantilevers by variation of pH between 7-3-7 A) Native HSA immobilized cantilevers. B) Denatured HSA immobilized cantilevers. Differential deflection signal by switching pH between 7-12-7 C) Native HSA immobilized cantilevers. D) Denatured HSA immobilized cantilevers.

There is a significant reduction in bending signal for denatured HSA in response to pH variation in comparison with native HSA. The difference in cantilever bending response is most probably due to variations in immobilized native and denatured protein structures. the difference in cantilever bending response is most probably due to disparities between immobilized native and denatured protein structures. Thermal denaturation of this protein has been previously studied using various techniques.[224–228] One of the initial studies have revealed that thermal denaturation of HSA follows multiple steps: native (N) → extended (E) → unfolded (U).[227] It has been concluded that during extended form (E) at temperature ≤55 °C, domains II and I of the protein fall apart but native conformation almost stays intact. However, at higher temperature (65-70 °C), unfolded state (U) persists accompanied by disruption of domain II, causing irreversible breakdown of the secondary and tertiary structure of protein.[229]

It has been examined from CD, FTIR, and dynamic light scattering (DLS) experiments (Appendix) that HSA underwent N → U state. CD experiments showed that α-helix content was dropped from 64% in native (N) state to 44.2% denatured (U) state thus increasing the random coil or unordered form in the protein. Similarly, DLS experiments showed that hydrodynamic radius (r_h) of the denatured protein was increased that is consistent with reported data.[227] An increase in r_h is attributed to equilibrium volume expansion of protein due to thermal denaturation. Prior studies have revealed that buried residues in the hydrophobic core of HSA get exposed during the N → E → U transition, which can perturb the long-range solute–solvent interactions.[230] Moreover, both CD and DLS experiments provided evidence of HSA in a structurally disordered U state, where some of the subdomains break down exposing the hydrophobic residues.

Figure 4.4 is a schematic representation of the structure of the native protein (A) and heat denatured structure (B). Most of the hydrophilic residues are located on the periphery of the globular native structure (**Figure 4.4A**), which is a compact conformation. The structural perturbation in the U state is linked to a change in the conformation entropy, which favors unfolding and is corroborated by the energy cost of S-S bond cleavage.[231,232] It is most probable that same entropic state is not recovered during the refolding process of denatured protein (solute) in water (solvent) and results in an improperly folded state with exposed hydrophobic protein residues.[229] Denaturation may lead to the unfolded state of the polypeptide chain and expose the hydrophobic residues on the surface of the protein (**Figure 4.4B**), allowing it to be in an uncompacted conformation. Switching of pH from 7 to 3 protonate all the residues on the surface (**Figure 4.4C**), which would change the interactions between the residues and neighboring immobilized native protein molecules resulting in significant cantilever bending signal. Similarly, on deprotonation (**Figure 4.4D**) of the native protein molecules, there is a change in the orientation of the molecules into an ellipsoid structure that results in cantilever bending. However, very low bending of the microcantilever immobilized with denatured HSA relative to native HSA may be due to exposure of hydrophobic residues, which does not allow the orientation or conformation to change significantly. It must be pointed out that denatured HSA indeed shows some change which may correspond to change in orientation due to protonation (**Figure 4.4E**) or deprotonation (**Figure 4.4F**) of the core of the protein. Another possibility is less amount of denatured protein molecules immobilized on the surface of the cantilever due to variation in their structural properties. This may also lead to lower deflection signal, which is evident in our results.

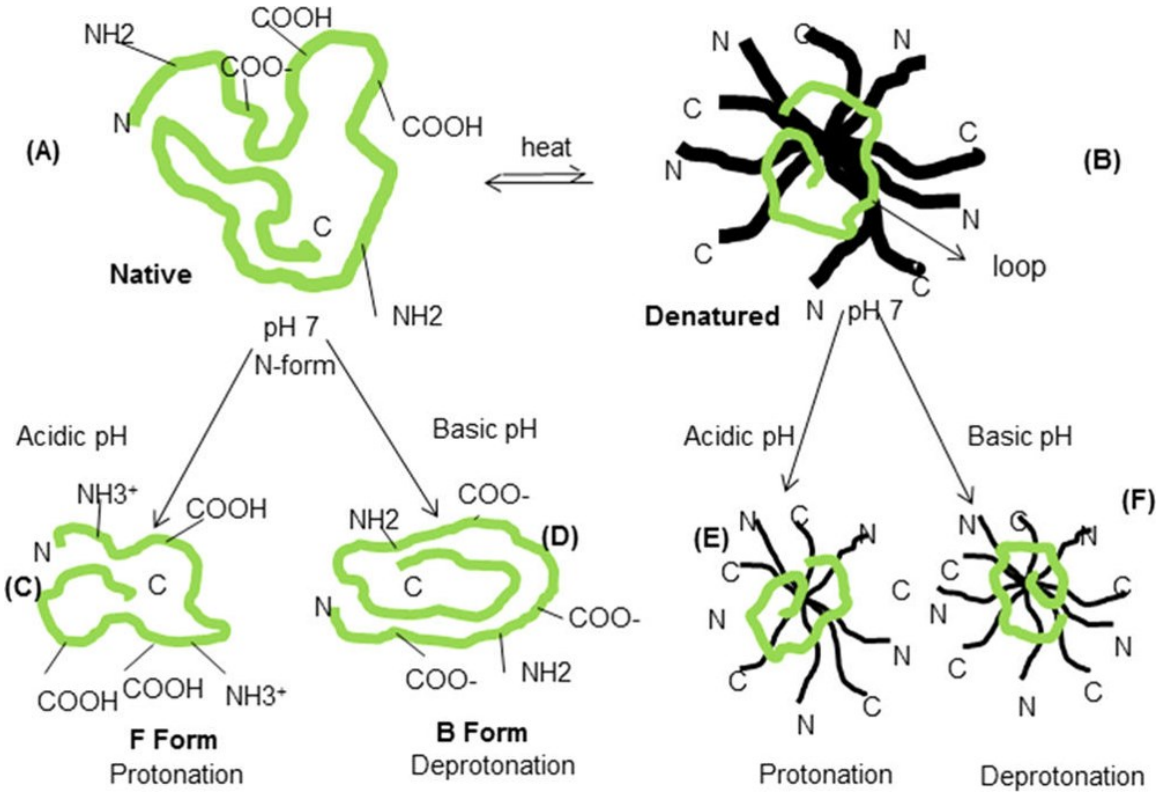

Figure 4.4 Illustration of native and denatured protein structures A) Native HSA. B) Denatured HSA. C) Protonated native HSA. D) Deprotonated native HSA. E) Protonated denatured HSA. F) Deprotonated denatured HSA.

Charge-charge repulsions either negative (at pH 12) or positive (at pH 3) in HSA residues bound to the microcantilever can appear when the pH is away from *pI* resulting in expanded protein structure.[233] Partial unfolding in the protein molecule at pH 12 can lead to decrease in helical structure thus less number of amino acids are involved in helix, therefore, there will be entropy change which leads to change in Gibbs free energy[234], that would in turn trigger surface stress change on the surface of a microcantilever. Conformation change in the protein structure is a consequence of a change in surface charge on the protein. Hence, protonation/deprotonation results in distinct surface charge density on the immobilized protein molecules. Consequently, there is a variation in surface charge density on the microcantilever surface immobilized with protein. It has to be pointed out that there is always ionization of backside of the cantilever due to variation in pH from neutral to acidic or basic. This will allow the cantilever to bend up independent of positive or negative charge densities. Hence, the bending of the cantilever will be in such a way to increase the surface area of charged surface. The net change in deflection may be due to variation in charge induced conformational change of protein molecules. Variation in the amount of bending for native and denatured HSA can be attributed to the effective change in charge on the surface of the microcantilever.

4.3.3 SPR investigations

To further examine the conformational change of immobilized HSA at liquid–solid interface, we used the SPR technique. Here, the sensor chip coated with gold was immobilized with native or denatured HSA and parallel experiments in line with microcantilever experiments were conducted.

Sensor chip was initially equilibrated by flowing PBS buffer (pH 7.4) and baseline was established. It was observed that for the native HSA, the sensorgram signal on injection of PBS buffer (pH 3) showed a change in reflectance angle of 80 ± 10 millidegree (**Figure 4.5A**). The relative change in resonance signal between PEG_{12}-CL and native HSA modified surface is 20 ± 15 millidegree. It has to be pointed out for PEG_{12}-CL, we also observe protonation and deprotonation. Clear transition points are seen after injection or switching of buffer from pH 3 to 7. The protein molecules appear to revert back to similar conformation or orientation after the injection time is over and PBS buffer at pH 7 is flowing into the cell. **Figure 4.5B** shows the transition from pH 7-3-7 for denatured HSA and PEG_{12}-CL. The resonance signal for denatured HSA is remarkably low at 35 ± 10 millidegree as compared to PEG_{12}-CL (100 ± 20 millidegree) and native HSA (80 ± 10 millidegree). In contrast to native HSA, denatured HSA shows a significant change in relative signal between PEG and denatured HSA immobilized sensor chips. For pH variation between 7-3-7, the relative change between PEG and protein coated sensor was 80 ± 20 millidegree for denatured HSA and approximately 20 ± 15 millidegree for native HSA.

Generally, increase in SPR signal reflects the increase in mass density at the sensor surface with a subsequent increase in the dielectric character. The water molecules interaction to the immobilized protein on the sensor surface may change the dielectric properties and consequently the refractive index.[235–237] For an unfolded or denatured protein the structural orientation is less compact or extended on the surface as observed from AFM images (**Figure 4.2 C**) which may allow the significant decrease in bound water content. Whereas,

in the case of native HSA, which is a globular structure there may have significantly high content of bound water.

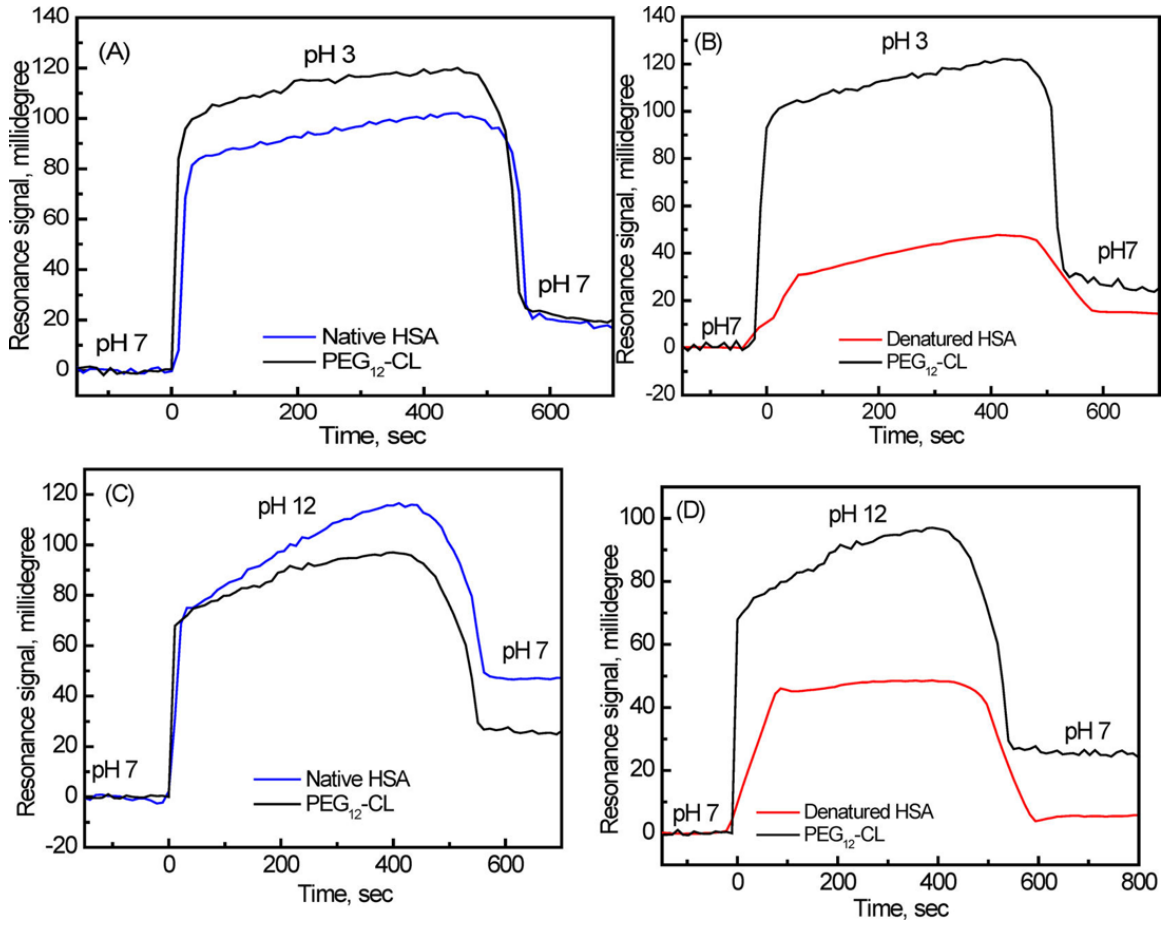

Figure 4.5 Surface plasmon resonance signal by variation of pH between 7-3-7. A) Native HSA immobilized sensor chip (blue), PEG_{12}-CL coated surface (black). B) Denatured HSA immobilized sensor chip. Relative resonance response of pH variation between 7-12-7: C) native HSA and PEG coated sensor chips. D) Relative resonance response between denatured HSA and PEG coated sensor chips.

Figure 4.5C shows the comparison between native HSA immobilized and PEG_{12}-CL coated sensor surface by variation of pH from 7-12-7. For the pH variation from 7 to 12, the change in resonance signal between PEG and native HSA is very low at approximately 0.1 ± 0. 5 millidegree. However, transition in reflectance angle was increased to100 ± 10 millidegree in contrast to native HSA at approximately 80 ± 10 millidegree. A higher slope in case of injection of pH 12 indicates that the time period required for achieving equilibrium state is longer in the case of pH 12 as compared to injection of pH 3. An interesting point to be noted was by reversing the pH from 12 to 7, the protein molecules were far above the original reflectance angle value at 50 ± 10 millidegree. This observation shows that the conformational change might not be completely reversible, especially when treating the protein molecules at pH 12.

Similar experiments with denatured HSA are presented in **Figure 4.5D**. The reflectance angle for denatured HSA upon transition from pH 12 to 7 was approximately 40±10 millidegree. Relative change between PEG_{12}-CL and denatured HSA was significant at approximately 40 ± 10 millidegree. SPR results for native and denatured HSA compliment to the microcantilever bending results, where both native and denatured HSA show a difference in the signal. For native HSA, the differential signal is higher in comparison with denatured HSA in the case of microcantilever deflection, which is promising prospect to develop pH based biomolecular sensors.

4.4 Conclusions

Conformation and orientation of native and denatured HSA at solid-liquid interface were investigated by two complementary techniques namely, microcantilever deflection and SPR spectroscopy. The surface stress on microcantilever was primarily due to charge induced conformational change of native or denatured HSA by variation of pH. We conclude from these experiments switching of pH on native and denatured HSA shows the variation in nanomechanical bending signal, which may be due to the variation of surface charge density on cantilever surface. This result indicates the HSA-protonation/deprotonation allow the protein on the surface of the cantilever to become more hydrophobic or folded. Since we know in solution there is a significant α-helix loss on acidic or basic pH, additional attractive forces may be dominant within the domains when HSA is immobilized on the surface. Complimentary results related to SPR show that the relative signal change for immobilized native protein does not show significant change when compared to cantilever deflection experiments. However, relative change for denatured protein in SPR is more pronounced as compared to deflection experiments. The two techniques work on entirely different principles, which reflect that the similar changes are observed in both techniques. However, the deflection signal change in case of cantilevers for native protein is more pronounced and would help in the development of pH based biosensors. Such studies would shed light on developing pH based biosensors on microelectromechanical systems (MEMS).

Chapter 5. Rapid and Highly Sensitive Detection of Dopamine using Conjugated Oxaborole based Polymer and Glycopolymer Systems

"Rapid and Highly Sensitive Detection of Dopamine Using Conjugated Oxaborole-Based Polymer and Glycopolymer Systems", Jiang, K., Wang, Y., Thakur, G., Kotsuchibashi, Y., Naicker, S., Narain, R., Thundat. T., *ACS Applied Materials and Interfaces*, **2017**, 9(18), 15225-15231.

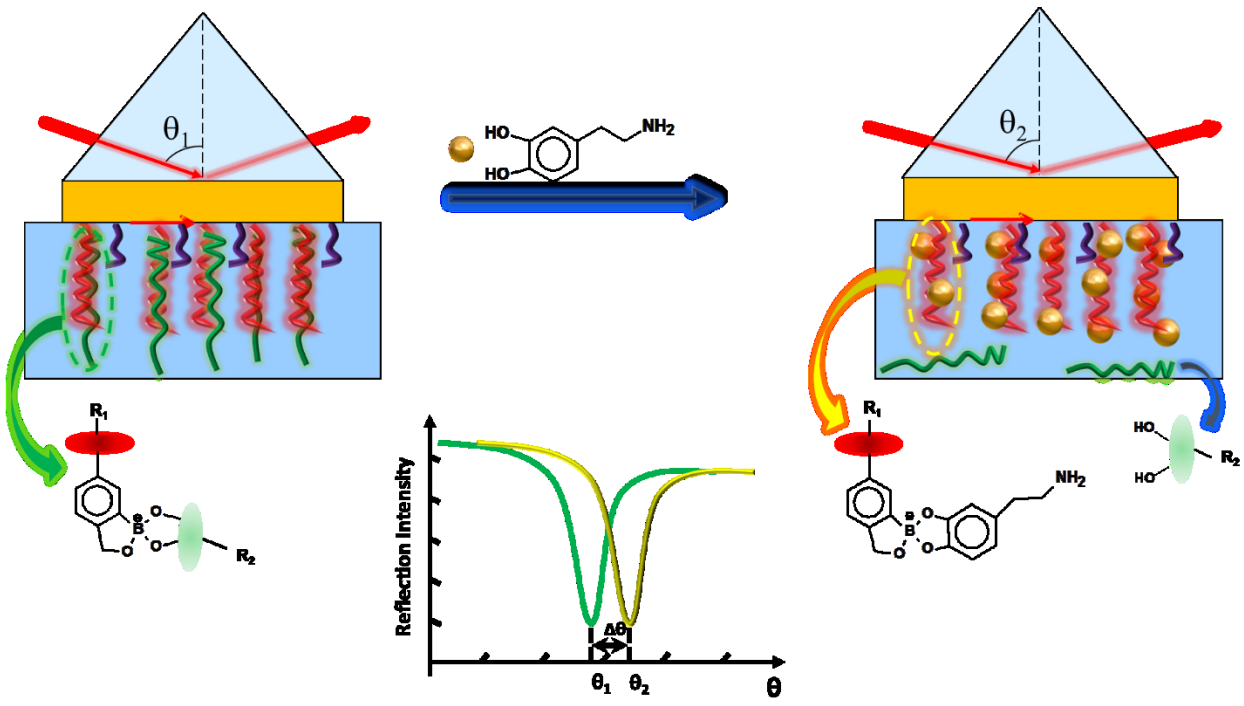

5.1 Introduction

Dopamine (DA) is a simple organic chemical in the catecholamine family which plays a critical role in the function of the central nervous system (CNS), endocrine system and cardiovascular system. Monitoring the concentration level of DA has attracted a great deal of attention since c[238–240]. Much effort has been focused on the development of techniques for highly selective and quantitative detection of DA. In the past decades, several analytical methods, such as high-performance liquid chromatography (HPLC)[241], capillary electrophoresis[242], fluorescence[243] and electrochemical methods[244,245], have been developed for DA level monitoring, but they require long sample-preparation time and well-trained operators. Novel sensors utilizing field-effect transistor (FET)[246], nanoparticles[247] and conducting polymers[246,248] have been developed for DA detection, but they require complicated sensor surface functionalization and lack long-term stability. DA level in biological samples is in the range of 10^{-9} to 10^{-5} mol L^{-1}(M), with an excess of epinephrine (EPI), ascorbic acid (AA), uric acid (UA) and other compounds[248,249]. Thus, development of a real-time detection system for DA that is highly specific and sensitive is still needed. Although there are many sensitive sensor platforms, they require selective receptor layers for obtaining selectivity in detection.

Boronic acid is well known for its interaction with molecules having a cis-diol configuration to form stable cyclic esters.[122] A well-defined copolymer poly(*N*-isopropylacrylamide-*st*-5-methacrylamido-1,2-benzoxaborole) (P(NIPAAm-*st*-MAAmBO)) has been synthesized by reversible addition-fragmentation chain transfer (RAFT) polymerization by Narain and coworkers.[123] Dopamine, due to the nature of the

catechol group, was reported to have a binding constant (~18000 K mol^{-1}) over two orders of magnitude higher than that of the cis-diol containing compounds (~100 K mol^{-1}), such as glucose, fructose, and mannose etc., toward the boronic groups.[250] However, due to the relatively low physiological level of DA as compared to other chemicals such as saccharides[239,251], a highly-selective sensing layer is needed for DA detection. It has been demonstrated that glycopolymers can form stable structure with boroxol containing compounds.[123,252] Due to their structural difference, the binding affinity between P(NIPAAm-*st*-MAAmBO) and glycopolymer (poly(2-lactobionamidoethyl methacrylamide) (PLAEMA), which has two cis-diol unit in each side-chain, is estimated to be lower than that of DA, but higher than that of monosaccharides[250]. This makes the conjugated P(NIPAAm-*st*-MAAmBO) and PLAEMA layer much less reactive to non-specific saccharides or other structural analogs, leaving only DA binding to P(NIPAAm-st-MAAmBO) by the displacing PLAEMA.

In this work, we describe a highly selective interface for DA detection and we demonstrate it in two different sensor platforms, namely surface plasmon resonance (SPR) and microcantilevers (MCL). SPR is a sensitive technique for fast and label-free detection of chemical and biological analytes.[253,254] Microcantilever sensor based on mechanical bending, on the other hand, utilizes changes in surface stress due to surface adsorption.[255] However, both the SPR and the MCL sensors require functional coatings for obtaining selectivity in sensing. With functionalized sensing layers, both sensor platforms have been utilized for sensing and diagnosing applications in solution environments that include whole cell recognition, protein interaction, glucose sensing, heavy metal detection, etc.[97,256,257] The conjugated polymer layer consisted of P($NIPAAm_{149}$-*st*-$MAAmBO_{19}$)

(MAAmBO content: 12 mol%, M_n: 13200 g mol^{-1}, M_w/M_n=1.27) and P(LAEMA$_{21}$) (M_n: 10000 g mol^{-1}, M_w/M_n=1.1).[123] In addition to the DA detection in buffer solutions, this conjugated polymer layer is evaluated for specificity in the presence of cross-reacting analytes such as saccharides, EPI, AA and UA. We have investigated the selectivity, sensitivity, and the polymer layer swelling of this conjugated polymer system. The possible regeneration of the polymer interface has also been evaluated.

5.2 Experimental Section

P(NIPAAm$_{149}$-*st*-MAAmBO$_{19}$) and P(LAEMA$_{21}$) were synthesized following previous work.[124–126,258] All other chemicals were obtained from Sigma-Aldrich (USA). Phosphate buffered saline (PBS, 0.1 M, pH 7.4) is used as a mobile phase solution flowing continuously through the gold coated sensor chip surface. All the water used in this work was deionized from a MilliQ instrument (18 MΩ cm^{-1}).

SPR sensor chips were fabricated based on lime soda glass slides. The dimensions were fixed as 2 cm×1.2 cm×0.05 cm. The sensor chips were coated with 5 nm titanium (Ti) adhesion layer followed by 50 nm gold (Au) using an electron beam evaporator (Kurt J. Lesker, USA) at a deposition rate of 0.2 Å sec^{-1}. Same gold coating procedure was applied on microcantilever sensors (MicroMotiv Octosensis, 500-µm length, 90-µm width, 1-µm thickness, MicroMotiv Microtechnology, Germany).

The gold-coated SPR and MCL sensor chips were carefully cleaned using piranha solution (H_2SO_4 and H_2O_2, 3:1 in volume) and rinsed by aliquots of water and ethanol and dried by nitrogen before any surface functionalization process. The polymer functionalization was

performed in a three-step method. First, P(NIPAAm$_{149}$-*st*-MAAmBO$_{19}$) was immobilized to the gold-coated surface of the sensor for forming a self-assembled monolayer (SAM) via thiol-Au covalent bond through the dithioester group at the polymer terminal. The second layer of P(LAEMA$_{21}$) was conjugated to the sensor substrate by the oxaborole-diol interaction as described previously. After rinsing with PBS, the chip was treated with thiolated poly(ethylene glycol) (PEG) to block any uncovered gold surface in order to avoid non-specific adsorption. A PEG functionalized chip was used as a reference to eliminating noise and other systematic errors (by common mode rejection). SPR reflection angle was measured by Navi 200 instrument (BioNavis, Finland) and the mechanical bending of microcantilevers was measured by means of a multiplexed optical beam deflection setup. SPR sensorgram and MCL deflection signals monitored as a function of time during the injection of DA samples. ^{11}B NMR was performed to confirm the DA displacement reaction with P(NIPAAm$_{149}$-*st*-MAAmBO$_{19}$) and P(LAEMA$_{21}$) conjugates. The topography of the conjugated polymer functionalized chip before and after DA injections was acquired using an atomic force microscopy (AFM) for investigating surface morphology evolution due to adsorption.

5.3 Results and Discussions

5.3.1 Detection mechanism

SPR is an optoelectronic phenomenon occurring at the interface between a negative and positive permittivity material stimulated by incident light. At a specific incident angle (resonance angle), the polarized light can resonantly excite the delocalized electrons

(surface plasmon) of the metal film, resulting in a minimum in the reflected light intensity. This angle is recorded as the SPR sensorgram. This electromagnetic surface wave propagates in a direction parallel to the negative permittivity (metal)-dielectric material interface. Since this surface wave is on the boundary of metal and the medium, the resonance is highly sensitive to any changes on the surface such as refractive index variation[1]. Surface plasmon obeys the following dissipation relation:

$$K_{sp} = \frac{\omega}{c}\left(\frac{1}{\varepsilon_1\mu_1} + \frac{1}{\varepsilon_2\mu_2}\right)^{-1/2} \qquad (5-1)$$

where ε is the relative permittivity, and μ is the relative permeability of the glass prism and the metal. The resonance angle strongly depends on the refractive index of the medium in close proximity of the metal surface[259]. Moreover, the local refractive index change is synchronous with the surface adsorption/desorption events.

Microcantilever sensor based on mechanical bending, on the other hand, utilizes changes surface stress due to molecular adsorption. As in the case of SPR sensors, microcantilevers also require immobilized selective layers for achieving selectivity in sensing. Molecular adsorption on the immobilized sensing layer on the microcantilever surface results in conformational change, which leads to a change in surface stress. When the sensing layer is immobilized only on one of the surfaces of the cantilever, a differential surface stress is generated that leads to cantilever bending. The bending (deflection) of the cantilever can be measured by reflecting a laser beam form the free end of the cantilever on to a position sensitive detector (PSD). The relation between cantilever deflection δ and the surface stress differential Δs is described by Stoney's formula[3]:

$$\Delta s = \frac{Et^2}{3L^2(1-\nu)}\delta \qquad (5-2)$$

where E is Young's modulus for the substrate (Si, 155.8 GPa), t is the cantilever thickness, L is the cantilever length and ν is Poisson's ratio (Si, 0.28). Besides quantitative measurement, microcantilever bending also demonstrates the sensing layer response with stimulus which can suggest the mechanisms of target-sensing layer interactions.

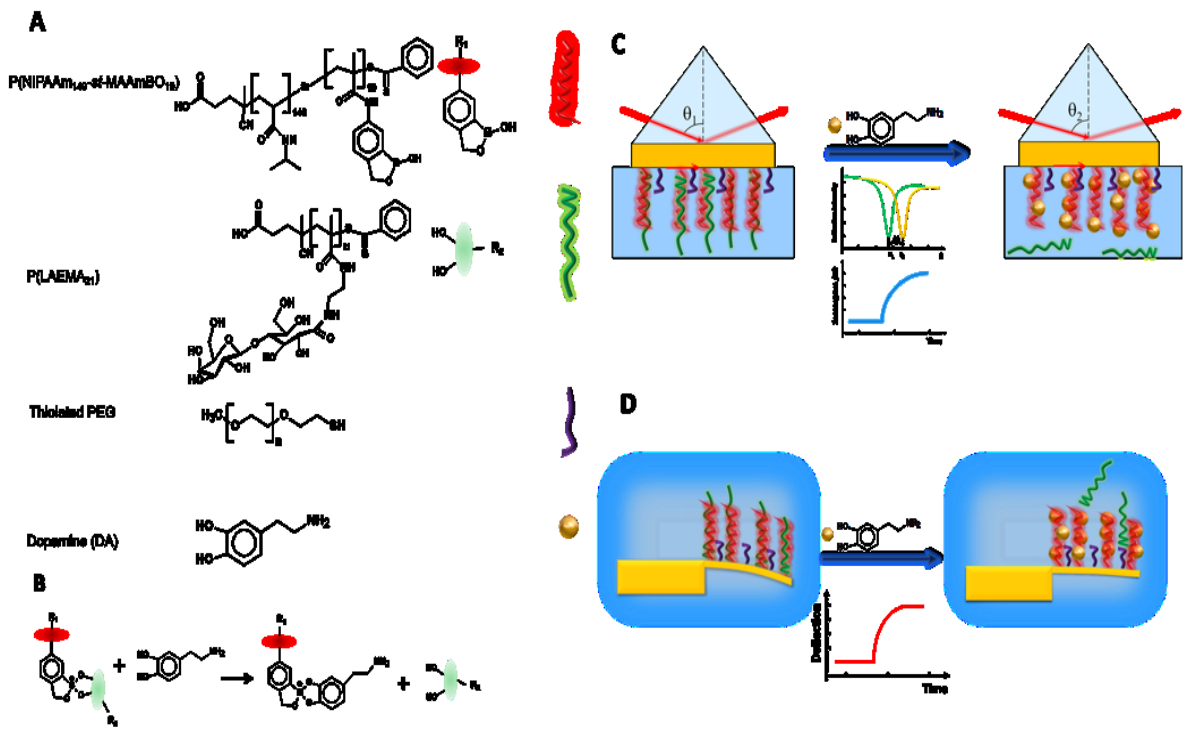

Figure 5.1 Polymer structures, binding of dopamine to oxaborole residues, SPR and MCL sensor platforms. A: Structures of the P(NIPAAm$_{149}$-*st*-MAAmBO$_{19}$), P(LAEMA$_{21}$) and DA; B: a brief equation showing the adsorption-displacement reaction on the sensor surface; C: Schematics illustrating light reflection angle change due to the surface plasmon resonance change caused by selective adsorption of molecules on gold surface; D: microcantilever deflection change due to DA displacement on conjugated polymer surface.

Figure 5.1 shows the DA detection mechanism using the covalent interaction between DA and P(NIPAAm$_{149}$-*st*-MAAmBO$_{19}$) on both SPR and MCL sensor platforms. The structures and schematics of the polymers and DA are listed in **Figure 5.1A**. The reaction process is briefly described in **Figure 5.1B** where the DA binding to P(NIPAAm$_{149}$-*st*-MAAmBO$_{19}$) resulting in the displacement of the previously conjugated P(LAEMA$_{21}$). The DA displacement swells the P(NIPAAm$_{149}$-*st*-MAAmBO$_{19}$) on the SPR sensor surface changing the local refractive index and the reflection angle. The increase in the reflection angle is measured as the sensorgram change for quantitative analysis (**Figure 5.1C**, see detailed information in **Chapter 1**). Similar experiments were also carried out with functionalized MCL sensors with repeated injections with DA. The displacement of P(LAEMA$_{21}$) by DA results in surface stress variation, which causes the microcantilever to bend (**Figure 5.1D**).

5.3.2 Conjugated polymer system on MCL platform

Figure 5.2 shows the experimental arrangement and the results for DA detection using cantilever arrays. A microcantilever array with 8 cantilevers was functionalized using capillary tubes, where the Group I was functionalized with P(NIPAAm$_{149}$-*st*-MAAmBO$_{19}$) only and the group III was functionalized with conjugated P(NIPAAm$_{149}$-*st*-MAAmBO$_{19}$) and P(LAEMA$_{21}$). The cantilevers in the Group II were functionalized with PEG and served as reference cantilevers. The functionalized MCL array was mounted in a flowcell with a constant PBS flow of 5 mL h^{-1}. DA sample with a concentration of 5 nM was injected into the flow without changing the flow rate, followed by PBS rinsing. As shown in **Figure 5.2B**, the PEG functionalized group had negligible responses to DA injection while the

bending signal of other groups of microcantilevers built up over time. After about 3000 seconds, the bending of the conjugated polymer and P(NIPAAm$_{149}$-*st*-MAAmBO$_{19}$) functionalized microcantilevers reached a steady state of about 95 nm and 140 nm (correspond to surface stress differential of 27 mN m^{-1} and 40 mN m^{-1}) respectively. An increase in the deflection indicates an increase in the surface stress on the polymer functionalized surface, which suggests the DA binding swells the polymers.[260,261] However, deflection change of the conjugated P(NIPAAm$_{149}$-*st*-MAAmBO$_{19}$) and P(LAEMA$_{21}$) functionalized cantilevers is slightly less than that of P(NIPAAm$_{149}$-*st*-MAAmBO$_{19}$) functionalized ones. This is possibly due to the pre-conjugated P(LAEMA$_{21}$) swelling the P(NIPAAm$_{149}$-*st*-MAAmBO$_{19}$) before the DA was injected. Thus, when the DA displaced the P(LAEMA$_{21}$), the swelling effect was less intense. Since the binding affinity between P(NIPAAm$_{149}$-*st*-MAAmBO$_{19}$) and P(LAEMA$_{21}$) is a critical factor for achieving enhanced selectivity of the sensor, slightly reduced sensitivity (due to reduced swelling) is acceptable.

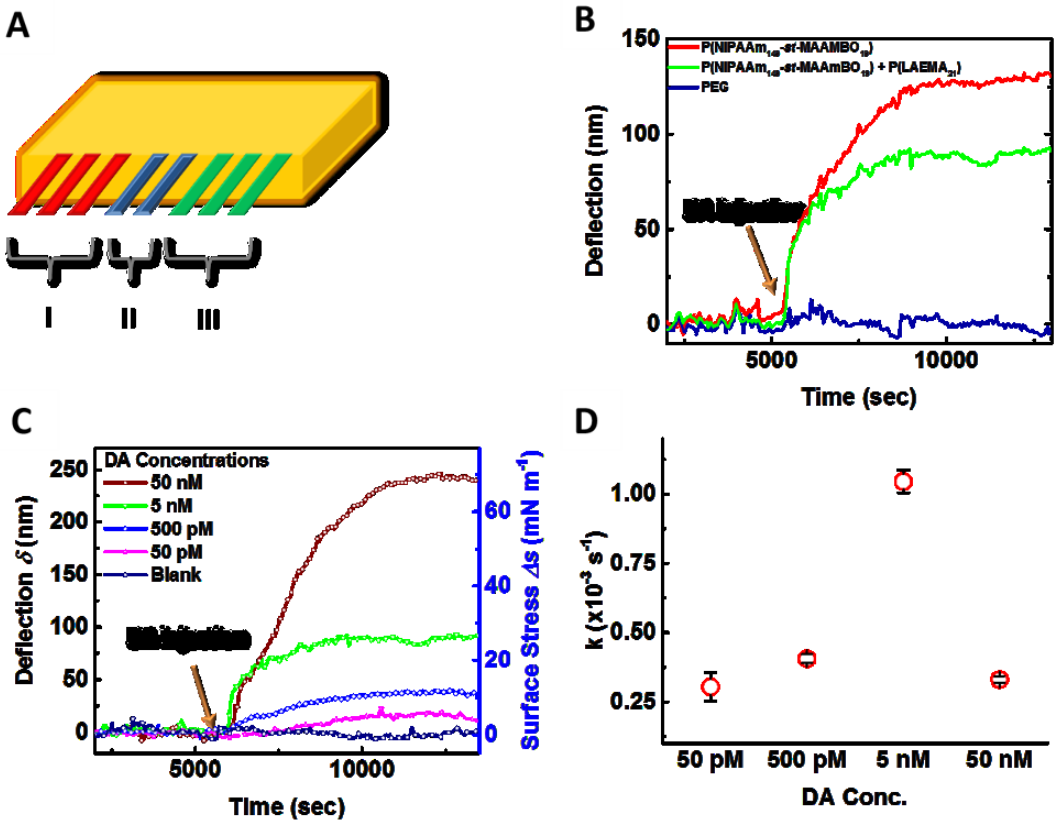

Figure 5.2 Microcantilever sensor array was used to monitor the polymer swelling with DA binding. A: schematic showing the MCL array functionalized with 3 different polymer layers, I: P(NIPAAm$_{149}$-*st*-MAAmBO$_{19}$) layer; II: PEG layer as blank reference; III: P(NIPAAm$_{149}$-*st*-MAAmBO$_{19}$) and P(LAEMA$_{21}$) conjugated layer; B: MCL bending with 5 nM DA injection: P(NIPAAm$_{149}$-*st*-MAAmBO$_{19}$) and P(LAEMA$_{21}$) functionalized microcantilevers have an average bending of 95 nm while P(NIPAAm$_{149}$-*st*-MAAmBO$_{19}$) functionalized beams bend 140 nm, indicating a larger amount of swelling. However, the binding affinity between P(NIPAAm$_{149}$-*st*-MAAmBO$_{19}$) and P(LAEMA$_{21}$) is one crucial factor of the sensor selectivity; C: MCL bending deflection increase with injected DA concentration from 50 pM to 50 nM from 15 nm to 240 nm; D: the binding constant (k) increases from 50 pM to 5 nM indicating a faster displacement reaction with increased DA concentrations, but a decrease of 50 nM sample suggests the saturation of the sensor surface.

The sensitivity and the limit of detection (LOD) of the polymer assisted MCL sensors were determined by injecting DA samples with various concentrations following the similar protocol described above. Freshly functionalized MCL sensors were used for each DA sample injections. From **Figure 5.2C**, it is clear that as DA concentration increased from 50 pM to 50 nM, microcantilever deflection change increased from 15 nm to 240 nm. Since the average noise level was ~5 nm, the LOD (for S/N≈3) of microcantilever sensor can be estimated as two orders of magnitude lower than the physiologically relevant level.[248] The P(NIPAAm$_{149}$-*st*-MAAmBO$_{19}$) swelling is enhanced with increasing DA concentration. A typical detection time for the MCL sensor is 5000 seconds under the test condition, which can be further adjusted by applying different flow rates. **Figure 5.2D** shows the variation of adsorption rate (*k)* as a function of different DA concentrations. For DA concentration increase from 50 pM to 5 nM, the adsorption rate showed an increase from 0.3×10^{-3} s^{-1} to 1.1×10^{-3} s^{-1}. This increase in the adsorption rate may be due to the availability of the multiple oxaborole units in the P(NIPAAm$_{149}$-*st*-MAAmBO$_{19}$) polymer chain as binding sites. However, for 50 nM DA injection, the adsorption rate decreases, which may be due to the saturation of the binding sites on the microcantilever surface.

5.3.3 Sensitivity of the conjugated polymer system on SPR platform

Figure 5.3 shows the sensitivity and dynamic range of the functionalized SPR sensor. Since the lowest DA concentration in physiological samples is around 10^{-9} M (1 nM), the sensitivity and resolution of the polymer functionalized SPR sensor was determined at nanomolar range. The injection of 1 nM DA generated 5.3 millidegree increase in sensorgram and the equilibrium was reached at about 800 seconds after injection. The

sensorgram evolution with the DA concentration is demonstrated in **Figure 5.3A**. For each DA sample injection from 1 to 10 nM, the corresponding sensorgram change is 5 millidegree (S/N≈5). The relation between the DA concentration (1 to 10 nM) and the sensorgram change is shown in **Figure 5.3B**. Thus, from 1 to 10 nM, the sensorgram exhibits a linear relation with DA concentration with a LOD of 1 nM.

The DA adsorption rate (*k*) also varies with the DA concentration. As the concentration changes from 1 to 10 nM, the adsorption rate (*k)* increases from 1.1×10^{-3} s^{-1} to 6.5×10^{-3} s^{-1} (**Figure 5.3C**). As indicated previously, the increased adsorption rate with increasing DA concentration can be due to the availability of the multiple binding sites on the P(NIPAAm$_{149}$-*st*-MAAmBO$_{19}$) chain. Interestingly, the adsorption rate of the SPR sensor is higher than that of the microcantilever sensor, which leads to a reduced detection time. The increasing adsorption rate for 1 to 10 nM of DA also suggests that the DA concentration can be measured accurately in this range.

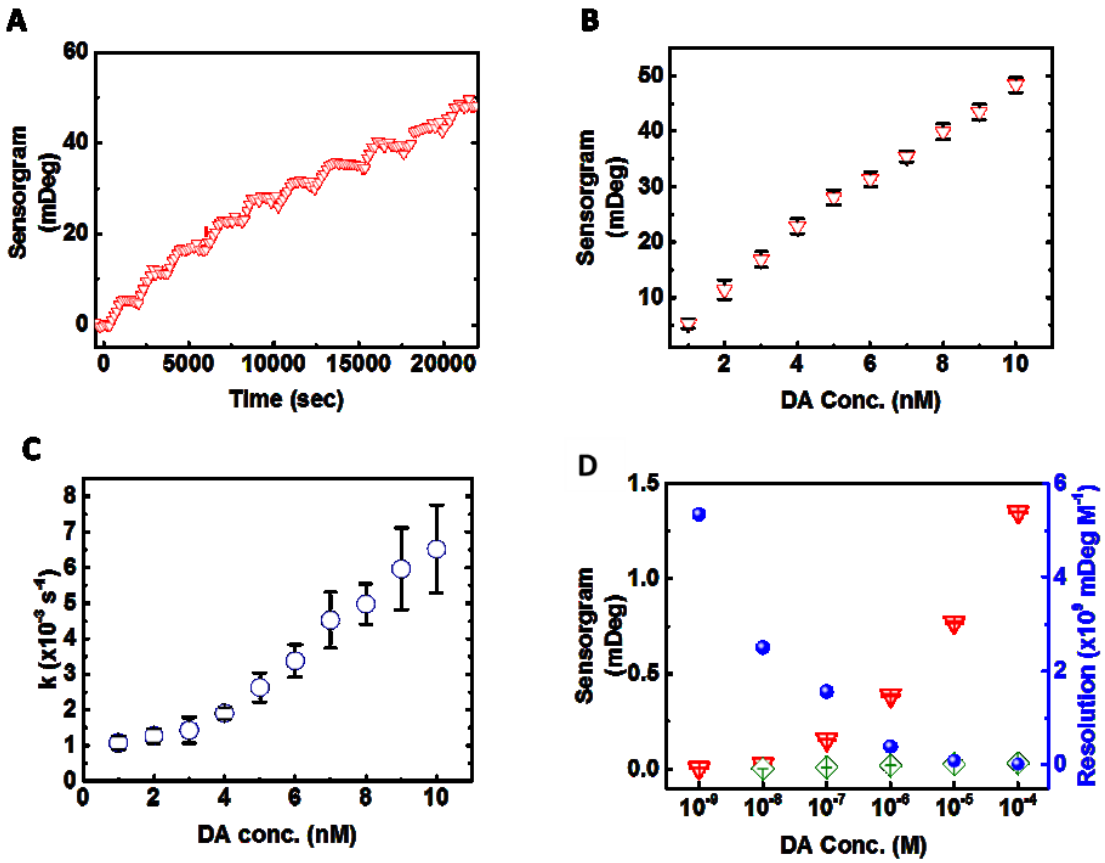

Figure 5.3 Sensitivity and working range of the P(NIPAAm$_{149}$-*st*-MAAmBO$_{19}$) and P(LAEMA$_{21}$) functionalized SPR sensor. A: SPR sensorgram increase from 5 to 50 millidegree with DA concentration from 1 to 10 nM; B: from 1 to 10 nM, the sensorgram-concentration presented a linear relationship; C: the DA adsorption rate increase from 1 to 10 nM due to the reaction kinetics; D: SPR sensorgram increase from 0.005° to ~1.4° over 5 folds of DA concentration with the conjugated polymer functionalized sensor(red) while the sensorgram remained identical with PEG functionalized sensor(green); and resolution of the functionalized SPR sensor decrease with the DA concentration.

The dynamic range of the polymer functionalized SPR sensor was determined by injecting DA samples from 10^{-9} to 10^{-4} M. As shown in **Figure 5.3D**, the sensorgram increases up to 300 times from 5 millidegrees to over 1.3 degrees while the DA concentration increases five orders of magnitude. It demonstrates that the polymer functionalized SPR sensor has a broad working range for DA detection. In contrast, the sensorgram of PEG functionalized blank reference chip does not change significantly with DA concentration. However, with higher DA concentration, the resolution of the conjugated polymer functionalized sensor decreases as shown in **Figure 5.3D**. The decrease in resolution can be attributed to the saturation of the binding sites. DA binds onto the sensor surface through a displacement reaction with pre-conjugated P($LAEMA_{21}$). However, the conjugated DA will affect the orientation of P($NIPAAm_{149}$-*st*-$MAAmBO_{19}$) which leads to the inhibition of the further DA adsorption. Also, when the injected DA samples are concentrated enough, there are not enough binding sites for the excess DA molecules; thus, the sensor resolution decreases.

5.3.4 Selectivity and recognition test of the conjugated polymers

The capability of distinguishing the target analyte of clinical samples is usually the major challenge for developing biosensors. The selectivity of the conjugated polymer sensing layer was investigated by comparing sensorgram variation caused by different injections with 5 nM DA, glucose, AA and UA samples using SPR sensors functionalized with conjugated P($NIPAAm_{149}$-*st*-$MAAmBO_{19}$) and P($LAEMA_{21}$); P($NIPAAm_{149}$-*st*-$MAAmBO_{19}$) only and PEG as blank control. Recognition tests were performed using EPI, AA and UA as the structural analogs and different monosaccharides (glucose, fructose, and

mannose) as other potential co-existing molecules with diols of equal or higher concentrations of 5, 50 and 500 nM.

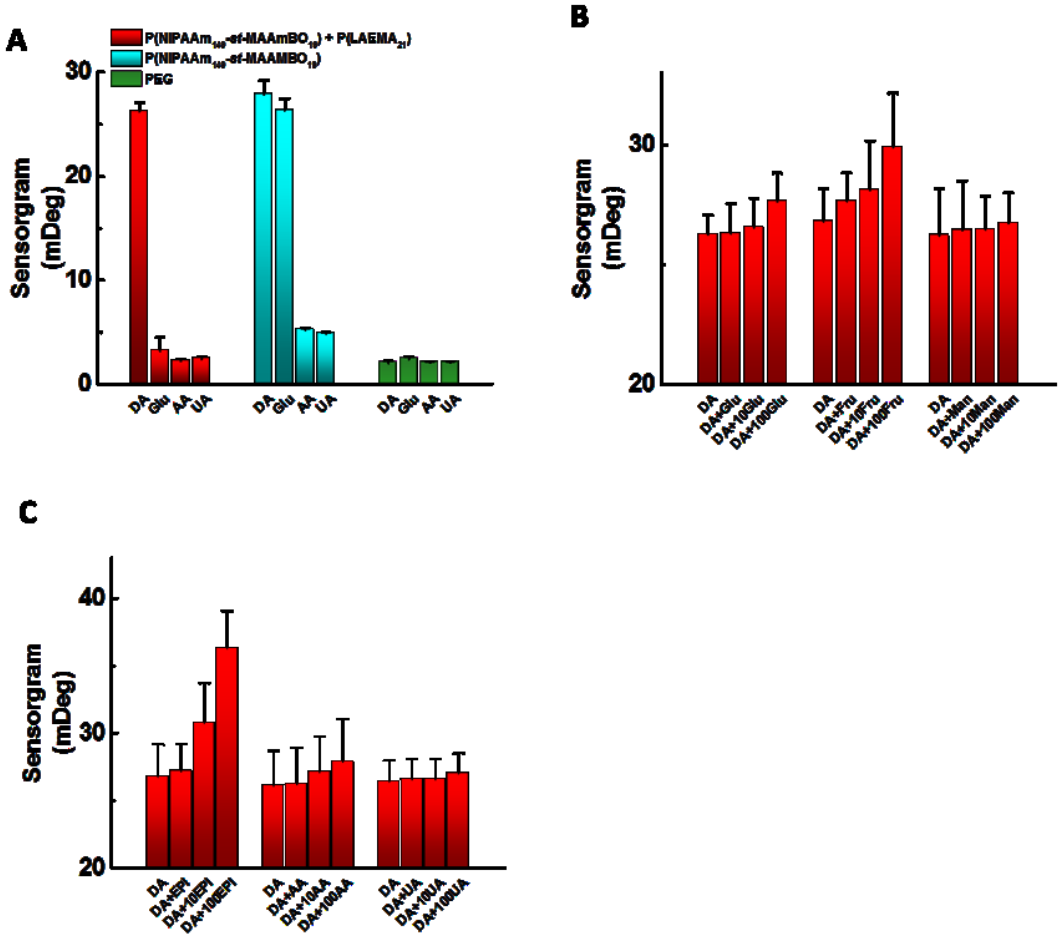

Figure 5.4 Selectivity and recognition test for the polymer assisted SPR sensor. A: selectivity of polymer sensing layer: with P(NIPAAm$_{149}$-*st*-MAAmBO$_{19}$) and P(LAEMA$_{21}$) functionalization, the sensor is selective to DA only; with only P(NIPAAm$_{149}$-*st*-MAAmBO$_{19}$), the sensing layer does not show any selectivity to DA; B: DA with monosaccharides; C: DA with other potential co-existed molecules and structural analogs. The functionalized polymer assay showed higher affinity toward DA than the saccharides, AA and UA, however, EPI interfered the sensorgram due to the structural similarity. All the tests are based on DA concentration of 5 nM.

The selectivity of the sensor was attributed by the conjugated P(NIPAAm$_{149}$-*st*-MAAmBO$_{19}$) and P(LAEMA$_{21}$) layer as stated previously. As demonstrated in **Figure 5.4A**, PEG functionalized sensor was almost inert to any sample injections. The P(NIPAAm$_{149}$-*st*-MAAmBO$_{19}$) showed significant response to 5 nM DA injection and a much lower response to AA or UA injections, but it failed to distinguish the glucose sample from DA. In contrast, the conjugated polymer layer has little response to glucose injection due to the estimated higher binding constant between P(NIPAAm$_{149}$-*st*-MAAmBO$_{19}$) and P(LAEMA$_{21}$) than that between P(NIPAAm$_{149}$-*st*-MAAmBO$_{19}$) and glucose. On average, one P(LAEMA$_{21}$) molecule has two cis-diol units on each side chain which lead to a higher binding constant to P(NIPAAm$_{149}$-*st*-MAAmBO$_{19}$) than that of glucose. According to previous studies of binding constant,[250] the maximum estimated binding constant is lower than that of DA. As compared to molecules with aliphatic hydroxyls, the aromatic hydroxyls from DA molecules can form more stable cyclic-esters with oxaborole groups. In addition, the aromatic groups in DA can further stabilize the cyclic-ester structure. Thus, the conjugated polymer functionalized sensor is selective to DA only. However, the conjugated polymers and P(NIPAAm$_{149}$-*st*-MAAmBO$_{19}$) functionalized SPR chips showed similar response with 5 nM DA sample, which is due to the similar level of thickness and surface roughness change caused by DA binding. This effect was further confirmed by AFM topography and surface roughness study. In addition, 5 nM DA did not saturate the SPR sensor surface, which also lead to similar sensorgram response.

It can be found in **Figure 5.4B** that sensorgram of DA slightly increases with the added saccharides. Fructose, which has the highest binding constant (~4000 K mol^{-1}) to boronic groups among the monosaccharides[15], introduced the largest sensorgram increase of about

11% when 500 nM of fructose was added. Due to the fact that the conjugated P($LAEMA_{21}$) has a higher binding affinity than the free monosaccharides, the displacement reaction happens when DA presented. Thus, the conjugated polymer functionalized sensor is capable of recognizing DA with coexisting saccharides. As illustrated in **Figure 5.4C**, the coexisting compounds UA and AA do not affect the detection at 100 times higher concentration than that of DA in the injected sample mixtures. This demonstrates that the sensor is highly selective to DA over UA or AA. However, with 10 times and 100 times concentrated EPI mixed in DA samples, the sensorgram level increased to about 15% and 40%. This effect of EPI was due to the structural similarity of the DA and EPI. Both molecules belong to catecholamine family (with catechol groups), which make them able to form covalent bonds with oxaborole groups on P($NIPAAm_{149}$-*st*-$MAAmBO_{19}$) and displace P($LAEMA_{21}$) from the conjugated polymer. It can be inferred that other molecules in catecholamine family (e.g. norepinephrine, NE) or large molecules (e.g. glycoproteins) can also interfere the detection results. Yet, comparing with other DA sensors,[247,248] this polymer functionalized SPR sensor has demonstrated high DA selectivity at nanomolar range.

5.3.5 Detection mechanisms of the conjugated polymer system

The mechanism of signal generation, changes in surface stress and refractive index, is attributed to DA binding induced swelling. We have carried out ^{11}B NMR to characterize the DA displacement reaction. Previous studies of ^{11}B NMR showed the ^{11}B chemical shift peak move to lower field when electron-withdrawing groups bound to boronic acid.[262] As illustrated in **Figure 5.5**, P($NIPAAm_{149}$-*st*-$MAAmBO_{19}$) revealed a single ^{11}B peak at 19.5

ppm. Upon addition of P($LAEMA_{21}$) to the solution, two small peaks at 10.9 ppm and 10.5 ppm were observed, indicating the binding between P($NIPAAm_{149}$-*st*-$MAAmBO_{19}$) and P($LAEMA_{21}$). Furthermore, when DA was added into the solution, the two peaks at 10.5 and 10.9 ppm disappeared and a new signal peak was observed at 7.9 ppm, which indicated the binding of DA to P($NIPAAm_{149}$-*st*-$MAAmBO_{19}$) by displacing P($LAEMA_{21}$). In comparison to the P($LAEMA_{21}$), DA, with a catechol group and its aromatic nature, shifted the ^{11}B peak to the lower field. It can be inferred that oxaborole group forms a far more stable cyclic-ester with the catechol group than with oriented cis-diols. Thus, DA can displace the conjugated P($LAEMA_{21}$) while the other compounds like saccharides, AA and UA can only bind to a minimum extent.

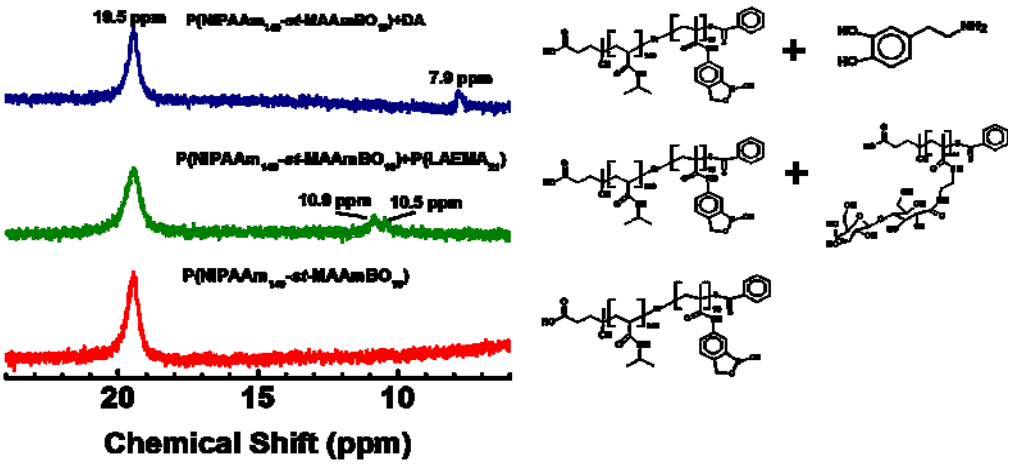

Figure 5.5 ^{11}B NMR characterization of DA interaction with polymers. Boron peak was observed at 19.5 ppm in P(NIPAAm$_{149}$-*st*-MAAmBO$_{19}$).; with P(LAEMA$_{21}$) bind, two more peaks at 10.9 ppm and 10.5 ppm were observed; DA binding to P(NIPAAm$_{149}$-*st*-MAAmBO$_{19}$) introduced a peak at 7.9 ppm due to the stronger electron-withdrawing effect.

We have also used AFM for characterizing the changes in the surface morphology of polymer layer due to DA adsorption. A FastScan C probe with a spring constant of 0.8 N m^{-1} was used for imaging. From comparing the topography of an SPR chip before and after conjugated polymer immobilization (**Figure 5.6A and 5.6B**), it can be concluded that during immobilization, irregularly shaped aggregates of 20 nm thickness formed on the gold-coated SPR sensor chip. **Figure 5.6C** shows that, after the 5 nM DA injection, the polymer layer thickness increased to 25 nm, indicating the swelling of P(NIPAAm$_{149}$-*st*-MAAmBO$_{19}$) due to DA binding. Also, the surface roughness increases from 4.8 to 5.2 nm after the DA displaced the P(LAEMA$_{21}$), which is also due to the swelling after DA binding. The 25 % swelling of the polymer layer thickness increases the local refractive index. In addition, the swelling of P(NIPAAm$_{149}$-*st*-MAAmBO$_{19}$) enhances the interaction between gold surface and PBS medium, resulting in an increase in the local refractive index. As a result, SPR sensorgram shifts due to DA binding to P(NIPAAm$_{149}$-*st*-MAAmBO$_{19}$) and resultant displacement of P(LAEMA$_{21}$). In contrast, the SPR chip with only P(NIPAAm$_{149}$-*st*-MAAmBO$_{19}$) yields a 28-nm-thick polymer layer, and after DA binding it increases to about 35 nm with a roughness increase from 5.5 to 6.8 nm (**Figure 5.6D and 5.6E**). Both polymer functionalized sensing layer has a comparable thickness with typical synaptic cleft distance (20-40 nm)[27], which makes it ideal for DA fast-scan detection. This result also confirms the previous selectivity test such that, with only P(NIPAAm$_{149}$-*st*-MAAmBO$_{19}$) on the surface, the initial polymer thickness and roughness are larger than that with conjugated polymers indicating the binding of P(LAEMA$_{21}$) increased the total coverage on the gold surface. On the other hand, the thickness and roughness variation of the conjugated polymer is less than that of the P(NIPAAm$_{149}$-*st*-

MAAmBO$_{19}$) but only slightly. Thus, the SPR sensorgram response from the conjugated polymer functionalized chip is lower than that of P(NIPAAm$_{149}$-*st*-MAAmBO$_{19}$) functionalized one.

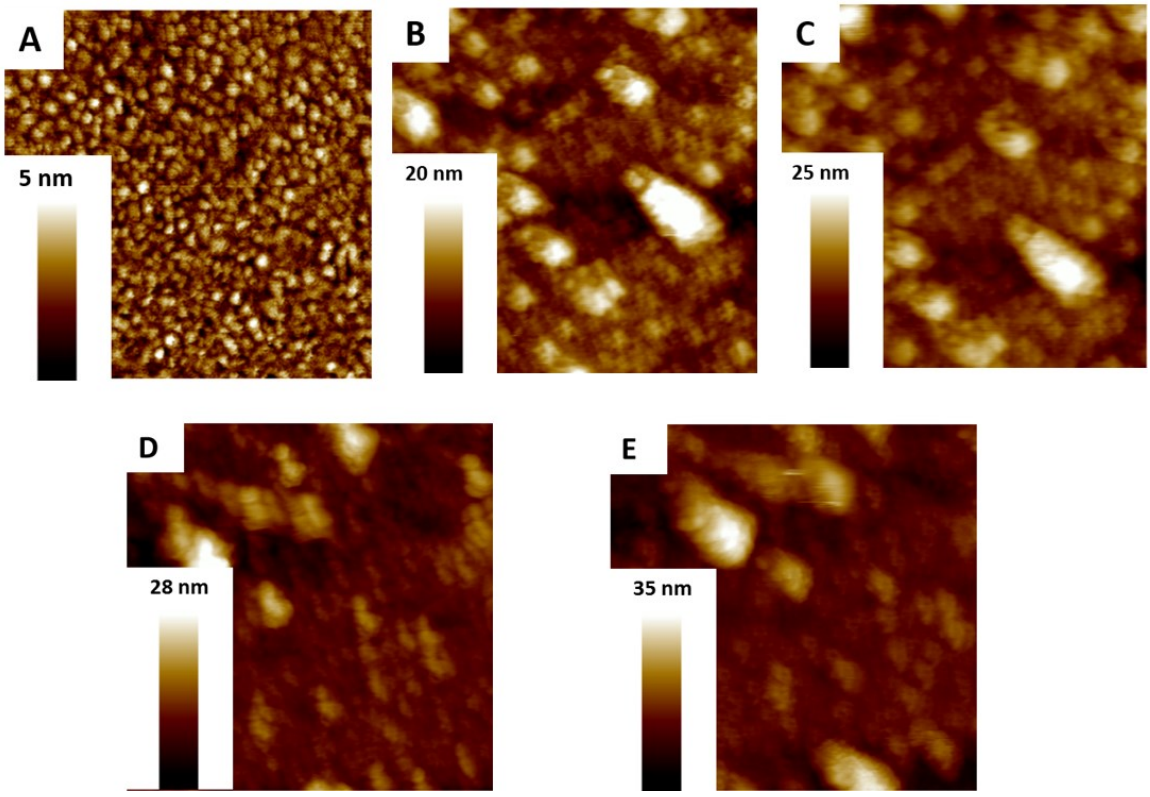

Figure 5.6 Atomic force microscopy (AFM) topography images of the SPR sensor chips. A: gold coated chips before polymer functionalization; B: sensor chip functionalized with P(NIPAAm$_{149}$-*st*-MAAmBO$_{19}$) and P(LAEMA$_{21}$) conjugated polymer layer; C: conjugated polymer functionalized chip after 5 nM DA injection; D: sensor chip functionalized with P(NIPAAm$_{149}$-*st*-MAAmBO$_{19}$); E: P(NIPAAm$_{149}$-*st*-MAAmBO$_{19}$) functionalized chip after 5 nM DA injection.

Compared with previously reported DA detection methods, the conjugated polymer functionalized MCL and SPR sensors have at least one order of magnitude improvement in LOD for DA detection.[263,264] In addition, the conjugated polymer functionalized sensors also have a relatively simpler preparation procedure without incorporating enzymes or other bio-componants.[246,265] The high sensitivity and selectivity of the presented sensor systems are due to the combined advantages of optimum binding affinity between P($LAEMA_{21}$) and P($NIPAAm_{149}$-*st*-$MAAmBO_{19}$), the DA displacement binding reaction, and the sensitivity of MCL and SPR sensor platforms. Compared to MCL sensor results, the SPR sensor does not achieve sub-nanomolar detection limit. However, the measured LOD at the nanomolar range is ideal for clinical detection. With the sensors as tested, the SPR sensor shows much-reduced detection time than the MCL sensor which is an advantage in potential clinical applications. Compared with other DA detection methods,[266] the conjugated polymer system offers a much simplified and compact sensor setup. Also, with a much faster detection and in real-time, in-line detection is possible. Usually, surface functionalization is one of the major limits for most of the surface related sensing techniques. However, this conjugated polymer system synthesized by RAFT method allowed the easy formation of self-assembled layer on gold coated sensor surface via the Au-thiol interactions. As shown by both MCL and SPR sensors, this conjugated polymer system can potentially be used in other sensor platforms.

5.3.6 Sensor regeneration and stability

In this study, we also take the advantage of the reversible covalent interaction between diols and oxaborole groups to design potential reusable biosensors. A surface regeneration

procedure was performed by washing with pH 4 PBS, and followed by the re-conjugation of P(LAEMA$_{21}$).[123,252] The sensor regeneration was tested over 5 times and evaluated using 5 nM DA sample. The sensorgram signal showed less than 10% decrease after 5 regeneration cycles, but it still showed reliable and reproducible results (**Figure 5.7A**).

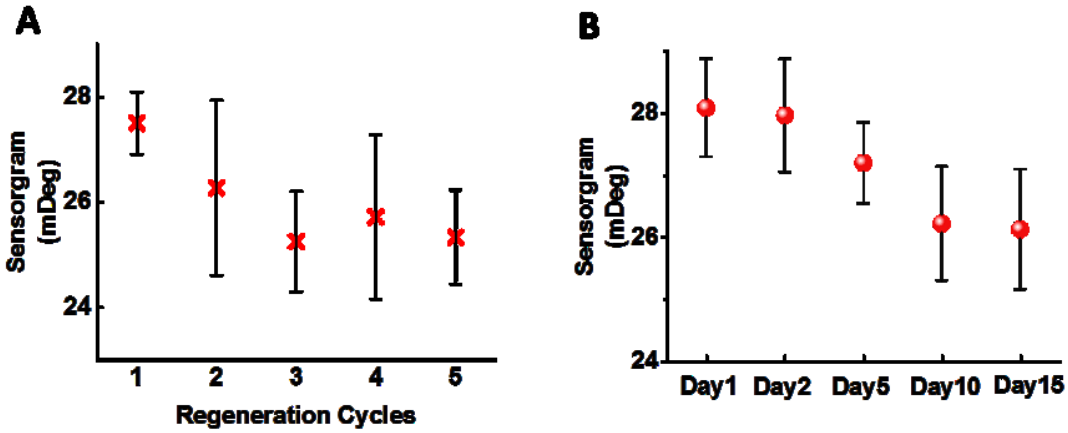

Figure 5.7 Sensor regeneration and stability test with 5 nM DA injections. A: SPR sensorgram signal reduced less than 10% after 5 times regeneration; B: the functionalized sensor remained 95% sensorgram signal within 5 days after surface functionalization and 90% after 15 days.

The sensor stability was also evaluated for over 2 weeks under ambient condition. From day 1 to 15, the sensorgram change representing 5 nM DA injections decreased about 10% (**Figure 5.7B**). It can be concluded that the polymer functionalized sensor is stable for at least 2 weeks. Comparing with methods using specific DA receptors[9], the conjugated polymer system provides much improved stability.

5.4 Conclusions

In summary, a conjugated polymer layer consisting of P(NIPAAm$_{149}$-*st*-MAAmBO$_{19}$) and P(LAEMA$_{21}$) was designed for real-time detection of dopamine with high selectivity, sensitivity and broad dynamic range. Sensing performance of the conjugated polymer was evaluated using MCL and SPR sensor platforms. The SPR sensor achieved a fast response time and a wide dynamic range from 10^{-9} to 10^{-4} M with a limit of detection of 1 nM, while the LOD for the MCL was 50 pM. Due to the optimum binding affinity between P(NIPAAm$_{149}$-*st*-MAAmBO$_{19}$) and P(LAEMA$_{21}$), this conjugated polymer sensing layer showed high selectivity to dopamine but little cross-reactivity to coexisting compounds like ascorbic acid, uric acid and saccharides. In addition, the sensing layer could be regenerated and reused for multiple times and was stable over 2 weeks at ambient conditions. Future studies will focus on real clinical sample selectivity and reliability test. This conjugated polymer system could be exploited as a unique method for DA detection clinically.

Chapter 6. Nanomechanical Manifestation of DNA Melting in a Microfluidic Cantilever

"Nanomechanical Manifestation of DNA Melting in a Microfluidic Cantilever", Keren Jiang, Arindam Phani, Javix Thomas, Faheem Khan, and Thomas Thundat, *manuscript in progress*.

6.1 Introduction

DNA replication is a fundamental process occurring in all living organisms and is the foundation for biological inheritance. Primarily it involves configuration and conformational changes.[267,268] There has been longstanding interest in understanding the DNA replication, and the physiochemical processes associated with it. The four major steps of this process include: "replication fork" formation; primer binding; elongation and termination.[269] Among them, "replication fork" formation is the "unzipping" of DNA helix by an enzyme, named helicase, which initiates the replication by breaking the hydrogen bonds (H-bonds) between base pairs and then unwinding the two strands. Other factors such as pH, presence of chemicals, and temperature can also lead to DNA helix dissociation.

Nucleic acid thermodynamics deals with the effect of temperature on the structure of double-stranded DNA (dsDNA). At melting temperature (T_m), half of the DNA strands are in the single-stranded state (ssDNA). Along with multiple other parameters, T_m is mostly determined by the length of the DNA strand and its specific sequence. Thus, by analyzing the denaturation/melting process, characters of the specific dsDNAs, such as cytosine(C)/guanine(G) pair content and sequence differences between two DNA sequences can be investigated. It is a simple solution for genotyping, mutation scanning and sequence matching.[270] Compared to DNA sequencing method, melting temperature study is less accurate, but it has much improved time and labor efficiency.

As thermal denaturation/melting is important in understanding DNA replication process, multiple efforts have been made for effective measurement of the melting temperature.

Optical absorption spectroscopy is typically used for obtaining DNA melting curve.[269] As the temperature is increased, the dsDNA begins to dissociate leading to a rise in the absorbance intensity. The bases (on the ssDNA) become unstacked and absorb more light in the 260-nm wavelength region. Thus, UV-Vis optical density at 260-nm (OD_{260}) is widely used for melting curve analysis. Techniques based on fluorescence spectroscopy are the most common approach since it can provide a much higher limit of detection (LOD).[271,272] But generally this method requires the use of fluorescent dyes to achieve higher LOD. With the existing commercially available methods, commonly, a sample size as much as one-milliliter is required for satisfactory measurement. It also requires sample amplification before analysis. The recent development of high resolution melting analysis (HRMA)[273] based on polymerase chain reactions (PCR)[274] methods are faster and less expensive approaches, but require well-trained personnel to conduct the tests.

DNA's mechanical properties influence many of its biological functions, for example, its interaction with proteins and its wrapping around histones.[275] Studies also show that many biological machines depend on the mechanical properties of dsDNA[217,276,277], which can be useful in designing of novel therapeutic methods. Traditionally, it has been a challenge to study the mechanical properties of DNA, but the advent of micron-scaled devices has triggered new approaches to study DNA melting process.[36,37,278] Nanomechanical biosensors, such as microcantilevers, have demonstrated that they are capable of detecting a single base mismatch in oligonucleotide hybridization.[37] With dsDNA functionalized on microcantilever surface, the DNA melting process can be monitored as changes in surface stress due to dsDNA dissociation.[36] However, variations in the graft density of immobilized DNA strands can result in irreproducibility in the measurements. Attempts to quantify the

immobilized DNA mass on the cantilever have been unsuccessful due to the severe damping for the cantilever in the solution. Additionally, non-specific adsorption also affects the mass sensitivity of the sensor.

In this study, we have employed a microfabricated microfluidic cantilever for analyzing the DNA melting by monitoring the effect of DNA melting on the viscosity of the buffer solution confined in the cantilever. The change in viscosity of the confined liquid affects the resonance response of the cantilever. Though the resonance frequency does not change because of the conservation of confined mass, the Q-factor of resonance shows large change due to changes in viscosity. By monitoring the changes in the Q-factor due to DNA melting process, the melting temperature T_m can be accurately determined. This technique depends on the increased energy dissipation of the cantilever due to unravelling of the DNA strands.

6.2 Experimental Section

6.2.1 dsDNA samples preparation

ssDNA samples were purchased from Integrated DNA Technologies (IDT, Iowa, USA). ssDNA and their compliment strand were incubated with calculated concentrations of in phosphate buffer saline (PBS, Sigma-Aldrich) for hybridization. PBS with varied sodium concentration was prepared by add sodium chloride. Formamide was added into PBS with calculated volume for comparing the solvent effect.

6.2.2 Q measurement

The microfluidic cantilever (MC-516, Fourien Inc. Alberta, Canada) used for this work is 500 μm in length, 20 μm in channel width, 3 μm in channel height. The structural material of the cantilever is silicon nitride which is quite compatible to bio samples. The sensor chip (5 mm × 5 mm) was placed in a vacuum holder and operated at a 10^{-5} mTorr pressure in order to reduce air damping thus increase the Q. In order to apply heat, a restive heater was used where the temperature was controlled through proportional integrated differential (PID) controller. The resonance of the DNA filled cantilever was measured by a MSA-500 laser Doppler vibrometer. During the experiment, the resonance frequency, vibration amplitude, and Q were measured simultaneously. dsDNA sequences with a variation on base pair numbers, composition (G/C ratio) were analyzed using the microfluidic cantilever. The viscosity and Q factor relationship can be briefly explained using a Kelvin-Voigt model. However, in this work, the total Q decrease comes from multiple factors such as the stiffness of the cantilever, elasticity and viscosity of the filled solution and the DNA melting process. To avoid the complicity of analyzing the Q change, a solvent sample has been used following the same temperature ramping process as a blank sample. By monitoring the Q difference (ΔQ) between the DNA samples and their solvents (blank), the DNA melting process was analyzed.

6.2.3 OD_{260} Measurement

OD_{260} measurement is performed using a Varian Cary 50 UV-vis spectrometer (Agilent, California, USA) equipped with an Isotemp 3016D heated bath circulator (Fisher

Scientific, Ontario, Canada). Incubated dsDNA samples were tested using a capped 1-mL quartz cuvette. Temperature was ramped according to the estimated T_m. 260-nm absorption peak was utilized for quantifying the DNA samples concentration variation during the melting process. T_m was determined by taking the maximum of dAbs/dT.

6.3 Results and Discussions

6.3.1 Quality factor (Q) measurement of DNA filled Microfluidic Cantilever

Miniature size of a microfluidic cantilever makes it an ideal platform for measuring changes in specific gravities of picoliters (pL) of confined liquids by continuous monitoring of its resonance frequency. In addition to quantifying the mass change (and the density) of the confined liquid sample, resonance response can also be used for monitoring the quality factor (Q) of the cantilever, a unit less parameter which describes energy dissipation in the resonator.[279] By monitoring the changes in the quality factor it is possible to estimate the changes in the viscosity of the sample present inside the cantilever. Q can be defined as follows:

$$Q = \frac{f_c}{\Delta f} \qquad (6-1)$$

where f_c stands for the resonance frequency, Δf is the full width at half maximum (FWHM) or resonance width. An increased viscosity of the liquid in the channel leads to higher energy dissipation with every resonant cycle, which causes a decrease in the Q. In the DNA melting process, the dissociation of the dsDNA results in the dynamic viscosity change of the solution inside the microfluidic channel.

The microfluidic cantilevers (MC-516, Fourien Inc., Edmonton, AB, Canada) used in this work had typical dimensions of 500 μm in length, 20 μm in channel width, 3 μm in channel height (**Figure. 6.1a and b**). The microfluidic cantilever has already been demonstrated for various applications such as to measure antimicrobial susceptibility[92], to identify proteins[280] and to characterize drugs.[281] During the experiment, the resonance frequency, vibration amplitude, and Q were measured simultaneously (**Figure. 6.1c and d**). DNA samples with different base pair numbers and different G/C contents were analyzed using the microfluidic cantilever. In this work, the total decrease in Q comes from multiple factors such as the stiffness of the cantilever, the viscosity of the filled solution and the DNA melting process. Therefore, we have used a differential approach by analyzing the temperature dependent Q change of a buffer sample as blank reference sample. By monitoring the difference in the Q (ΔQ) between the DNA sample and its solvent (blank), the DNA melting process was analyzed.

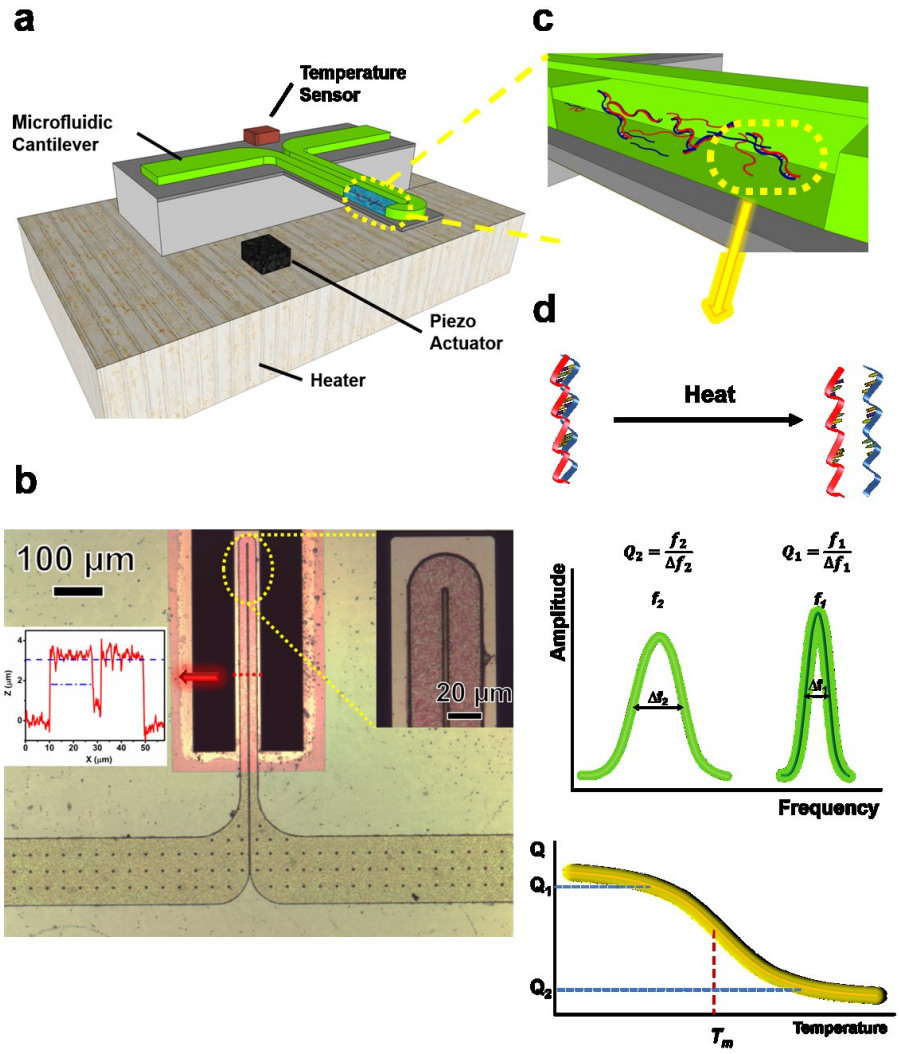

Figure 6.1 Schematics and images of microfluidic cantilever setup and the nanomechanical characters measurement. a. A scheme of the microfluidic cantilever setup; b. A white light confocal microscopy image of the MC-516 microfluidic cantilever. This cantilever is 500 µm in length, 20 µm in channel width, 3 µm in channel height. The right insertion is a zoom-in image on channel tip; the left insertion is a section height profile from the marked position of the microfluidic channel cantilever.; c. a zoomed-in view of DNA melting process in microfluidic channel and d. a schematic illustrating the frequency and Q factor change during the DNA melting process.

A typical dsDNA (DNA-1) melting in a microfluidic cantilever result shows that the Q decreases with increasing temperature (**Figure. 6.2a**). From 35 to 40 °C, the reduction in the Q is insignificant, indicating that the viscosity does not change much in this range. However, the decrease in the Q is large from over 9000 to less than 8200, in the temperature range of 40 to 50 °C, indicating significant changes in the viscosity of the liquid in the microfluidic channel. After 50 °C, the decrease in the Q turns negligible again, indicating the end of the melting process. In comparison, from 35-50 °C, phosphate buffer saline (PBS) blank sample shows a steady Q decrease from 9100 to 8900. Sample of ssDNA also shows a limited decrease in the Q from 9100 to 8750 over the temperature range. As illustrated in **Figure. 6.2a**, the frequency of the dsDNA, ssDNA and PBS all showed an increase with increasing temperature. These results can be explained as a result of the decrease in the density of liquid with increasing temperature. However, these observed resonance frequency changes for all the samples were less than 2% of their room temperature values. These results show that temperature dependent change of effective mass is small for a microfluidic cantilever.

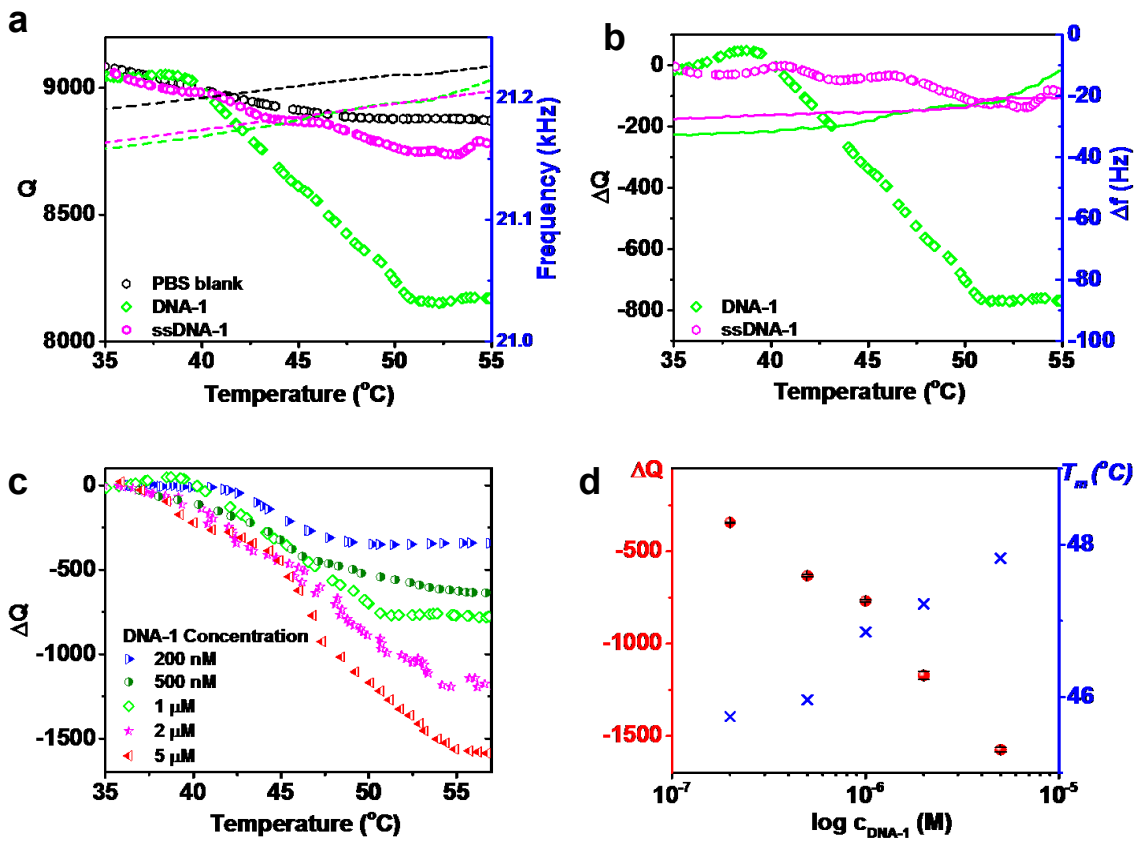

Figure 6.2 Q factor decrease as a function of temperature, dsDNA shows a significant change while ssDNA shows limited change, PBS buffer is tested as blank reference. a: Q decrease with temperature ramping and frequency increase in the same range; b: ΔQ change corrected from PBS blank data; c&d: ΔQ and T_m variation with increased DNA concentrations.

The dsDNA-1 has a ΔQ decrease of about 800 while ssDNA has ΔQ change less than 200 from 35-55 °C (**Figure. 6.2b**). Using the same correction method, dsDNA and ssDNA have frequency change (Δf) less than 20 Hz, which shows the minimal effect of DNA melting on the cantilever frequency. From the ΔQ vs temperature curve, the T_m was determined to be about 47 °C. This value shows very good agreement with the T_m from determined from UV-vis OD_{260} (49 °C, see **Figure 6.3a**). But compared to the UV-vis spectroscopy method, the sample volume used in the microfluidic cantilever sensor is only 100 pL, which is much less than the 1-mL needed for the UV-vis measurement.

The viscosity increase during the DNA melting is mainly caused by the increase in the number of DNA molecules. Theoretically, during the process of unravelling of dsDNA into ssDNA, the number of molecules are doubled. As the total number of molecules increases, the mean free path between molecules inside the microfluidic channel decreases, leading to an increase in the viscosity and a resultant increase in the ΔQ. In order to verify the changes in ΔQ with changes in DNA concentration, experiments were conducted with DNA-1 samples with different concentrations (**Figure. 6.2c and d**). For concentration from 200 nM to 5 μM, the ΔQ change due to melting ranges from 350 to over 1500, while T_m increases from 46 to 48 °C. Since ΔQ from PBS blank in the same temperature range is about 200, it can be inferred that 200 nM is the LOD of this microfluidic cantilever sensor system.

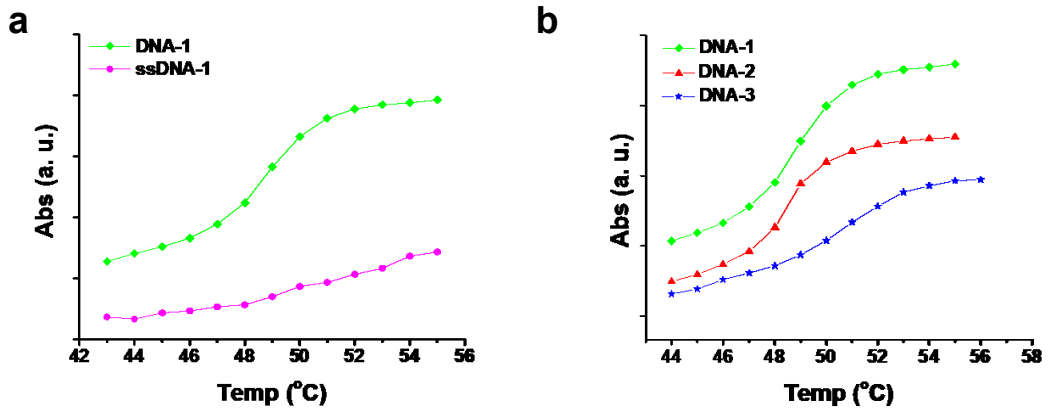

Figure 6.3 UV-vis OD_{260} measurement of the DNA samples. a: from 43 to 55 °C, dsDNA-1 shows sharp absorption increase between 46 to 51 °C, T_m is determined as 49 °C; however, ssDNA-1 does not show sharp absorption change with temperature ramping; b: T_m of DNA samples with different sequence is also determined by OD_{260}. T_m measured are listed in **Table 6-1**.

Table 6-1 T_m variation with DNA sequences (°C)

	Calculated	OD_{260}	Cantilever
DNA-1	56.1	49	47
DNA-2	55.5	49	47
DNA-3	60.5	52	50

6.3.2 DNA Sequences and Nanomechanical Properties

The sequence of the DNA also affects the T_m and also the viscosity during melting. As illustrated in **Figure. 6.4a**, DNA-2 shows a similar ΔQ decrease with temperature as DNA-1, but ΔQ variation is reduced to 500. It can be explained as the result of the sequence length difference between the samples. DNA-2, as a 25-mer DNA, has a much-reduced length than DNA-1 (45-mer). When the DNA-2 sample melts, the ssDNA is less flexible compared to the ones from the 45-mer DNA-1, and therefore, the increase in viscosity is less than that due to DNA-1. However, with a G/C content of 28%, DNA-2 shows a similar T_m with DNA-1. DNA-3, with G/C content of 48%, has a measured T_m of 50 °C, but a similar ΔQ decrease with DNA-2 because of the same sequence length. From the -dΔQ/dT variation with temperature (**Figure. 6.4b**), the T_m of DNA samples can be determined. With a specific sequence length, G/C content determines the T_m of DNA samples. For all the three DNA samples, drastic decrease in ΔQ and peaks corresponding -dΔQ/dT were observed with DNA melting, proving that the T_m could be determined with 100-pL sample with 1μM concentration.

DNA sequence affects T_m due to variation in the number of hydrogen bonds. Each G/C pair forms three H-bonds while each A/T pair forms two H-bonds. Therefore, dsDNA samples with higher G/C content requires higher energy to melt. A rough estimation for 15-20 nucleotides primers, known as Wallace method,[282] is given by:

$$T_m = 2(A + T) + 4(G + C)\ ℃ \qquad (6-2)$$

T_m of DNAs with more base pairs can be estimated using nearest-neighbor interaction method.[283,284]

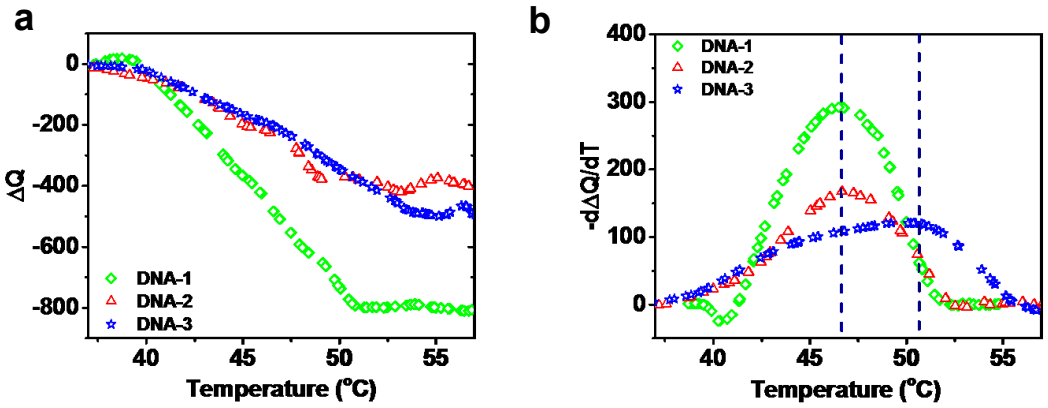

	Sequence	GC%
DNA-1	5'-AAAAAAATTTTTAAATTTAAATTTAAATTTAAATTTAAATTTAAA-3'	**0**
DNA-2	5'-CCCAAATTCAAATTAATAAAAACCC-3'	**28%**
DNA-3	5'-GGAGGGAAGAAGAAATTGGGGTTGA-3'	**48%**

Figure 6.4 T_m varies with DNA sequences. Base pair number and G/C content are the two major factors determine T_m of DNA samples. a: ΔQ change with three different DNA sequence, longer sequence promotes larger ΔQ change, higher G/C content results in higher T_m; b: DNA melting rate change with temperature; ΔQ decreasing rate and magnitude is affected by DNA sequence, asymmetric rate change indicates that with higher G/C content, DNA melts at a higher rate at higher temperature due to the higher energy required to dissociate G/C bonds.

Longer DNA sequence causes a larger decrease in ΔQ, indicating a higher viscosity increase. For the same molar concentration of dsDNA molecules, the initial solution viscosity is similar for all DNA samples at helical state. However, after the dissociation of the helices, longer DNA chains have a shorter mean free path in their coil state, which results in a higher viscosity. In addition, dsDNA has a persistence length of 50 nm while ssDNA has a persistence length less than 4 nm,[285,286] which means after DNA melting, the ssDNA will be in a random coil conformation. Base pair stacking is another major contributing factor for the dsDNA stability. Due to its hydrophobic and electrostatic nature, base pair stacking is much more prevalent in dsDNA than in ssDNA, providing the structural support for the dsDNA.[287] As a result, when dsDNA dissociates into ssDNA, the "rod-like" structure turns into coil structure and can dynamically wind into "balls" or "hairpins", which increases the total viscosity of the fluid.

Comparing the three samples, the DNA-1 sample with only A/T base pairs shows a higher ΔQ changing rate than the G/C containing sequences of the DNA-2 and the DNA-3 samples. The DNA-3 melting curves cover a temperature range of over 15 °C while DNA-1 melting process completes in a 10 °C temperature window. Higher G/C content leads to a higher T_m and also a smoother melting curve. The A/T rich region can dissociate at a lower temperature while the G/C rich region stays hybridized, leaving the dsDNA in a "half-melt" state. This process leads to an asymmetric melting rate with temperature increasing. The T_m of the DNA-3 is 51 °C, but the melting process starts at around 40 °C and completes at about 55 °C. With higher G/C content, the asymmetric feature is enhanced, indicating the G/C rich region melts only at a higher temperature.

Comparing with the T_m measured by OD_{260} **(Figure. 6.3b)**, all three DNA samples have similar T_m results from both methodologies. The OD_{260} result also confirms the reduced melting rate with higher G/C content. But the asymmetric melting feature is not observed in OD_{260} since it measures concentrations related light absorption rather than the molecular conformation related mechanical property.

As noted in Supplementary Table 1, all the DNA samples have much higher calculated T_m than the measured T_m values from both experimental techniques. It is possibly related to the formation of self-hybridized structures, such as a hairpin structure **(Figure. 6.5**), which leads to a much lower T_m than the fully hybridized dsDNA. For example, the DNA-3 has a calculated T_m of 60.5 °C. However, a possible existing hairpin structure with only two A/T bond formation at base number 10/17 and 11/16 can largely reduce the T_m of the dsDNA. Other small variation such as nucleic acid mismatch can also cause a decrease in T_m.[37] Similar situations apply to the other DNA samples used in these studies. Comparing the experimental results with the calculated values of T_m for many synthetic DNA sequences can provide insight into thermodynamics of DNA configurations. However, for real samples or naturally existing dsDNA samples, the sequences are usually much larger than the ones studied here. Thus, further study is needed for identifying the dynamic process of the melting.

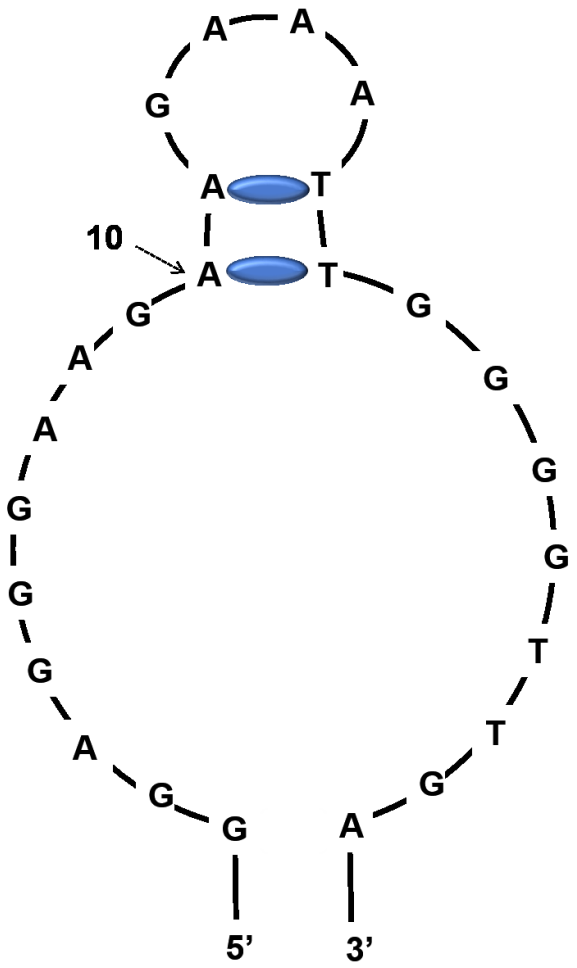

Figure 6.5 A possible self-hybridized hairpin structure of DNA-3. The H-bonds forms between A/T at 10/17 and 11/16, lead to a large decrease in T_m from the theoretical estimation T_m.

6.3.3 Effects of Ionic Strengths and Chemicals on DNA Melting

DNA melting point can be affected by other parameters such as ionic strength. The dsDNA samples in different concentrations of Na^+ were analyzed using microfluidic cantilevers (**Table 6-2**). From theoretical estimation, the DNA-1 sample for Na^+ concentration from 50 to 200 mM, the T_m increases from 49.5 to 61 °C. The T_m measured from the microfluidic cantilevers showed a similar increasing trend with Na^+ concentrations. However, the T_m values measured from cantilever sensors are much lower than the estimated T_m, which is similar to the previous results from different DNA samples, indicating other possible existing self-hybridized structures. The OD_{260} measurement also proves that the T_m increase with Na^+ concentrations (**Figure 6.6a**) and is in good agreement with the values from cantilevers. From **Figure 6.7a**, the ΔQ also varies with Na^+ concentrations. For Na^+ concentrations from 50 to 200 mM, the T_m increases from 43 to 50 °C (**Figure. 6.7b**). From helix state (dsDNA) to coiled state (ssDNA), ΔQ increases from 500 to 800 with Na^+ concentration increase. The phosphate groups, which form the backbone of DNA strand, are negatively charged at physiological pH (PBS, pH=7.4). Cations can stabilize the DNA duplex structures via decreasing the local negative charge density.[288–291] With higher Na^+ concentration, the viscosity variation is larger after melting, indicating a reduced mean free path between the molecules after DNA melting. One possible explanation is that with higher Na^+ ions concentration, the repulsive force between the strands decreases. As a result, the ssDNA molecules have a reduced mean free path and can possibly form other cross-binding structures. Na^+ also affect the base pair stacking[290] and elasticity of DNA molecules[292], which also contribute to the overall viscosity change.

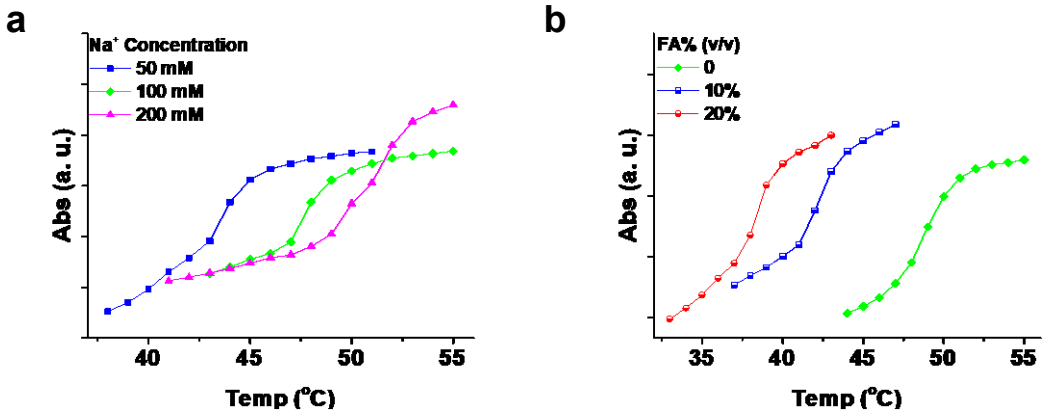

Figure 6.6 OD_{260} measurement of the DNA samples with variation in Na concentration and formamide (FA) fraction. a: from 36 to 55 °C, dsDNA-1 with increasing Na^+ concentrations, T_m increases; T_m measured are listed in **Table 6-2**; b: T_m of DNA samples with different FA fraction in PBS is also determined. T_m measured are listed in **Table 6-3**. OD_{260} results agree with the T_m determined from cantilever measurement.

Table 6-2 T_m variation with Na^+ concentration (°C)

Na^+ Conc. (mM)	Calculated	OD_{260}	Cantilever
50	49.5	45	43
100	56.1	49	47
200	61.9	54	50

Table 6-3 T_m variation with FA fraction (°C)

FA% (v/v)	Calculated	OD_{260}	Cantilever
0	56.1	49	47
10	50.3	43	43
20	44.5	38	37

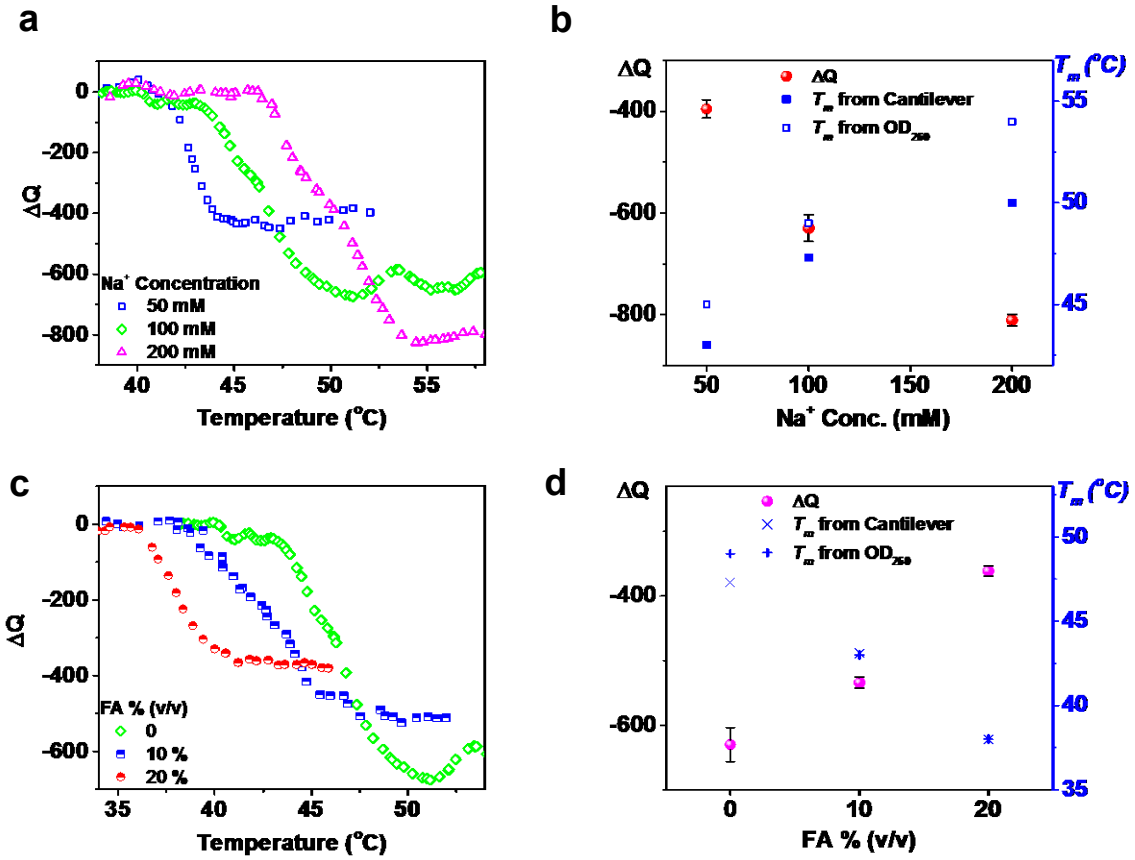

Figure 6.7 Ionic strength and solvent content also affect DNA melting process. A: ΔQ decrease as a function of temperature with varied Na^+ concentrations; b: ΔQ and T_m increase with higher Na^+ concentration; c: ΔQ decrease as a function of temperature with varied formamide fraction; d: ΔQ and T_m decrease with higher FA fraction in solvent.

The effect of the presence of chemical on the DNA melting process is also evaluated. Formamide (FA, H_2NCHO) is one well-known compound which destabilizes the dsDNA by forming H-bonds with base pairs.[293] As listed in **Table 6-3**, FA fraction (v/v) increasing in PBS buffer leads to a decrease in the T_m of the DNA-1 sample. These results also show a lowering of the measured T_m value compared to the estimated T_m (~0.7 °C/ FA%) values.[294,295] Fig. 4c and d show that ΔQ is lower with higher FA fraction, which is also related to the destabilizing effect caused by FA. The formation of H-bonds and possibly complex structures with ssDNA also lead to an increase in the mean free path between the molecules. Thus, the ΔQ decreases with higher FA fractions. Similar to the ionic strength effect, OD_{260} measurement gives the T_m change, but not the other mechanical information (**Figure 6.6b**). It can be concluded that the measurement of DNA melting using hollow channel microcantilevers can provide thermal, dynamical and micromechanical information of DNA melting. It is also possible to measure the Gibbs free energy change during the melting process. This concept of using viscosity changes for characterization can also be used in other applications including protein folding, drug delivery and so on.

6.4 Conclusions

Energy dissipation in a resonating microfluidic cantilever varies sensitively due to configurational changes in the DNA and can provide new understanding of the nanomechanical processes associated with DNA replication process. Viscosity, which is a measure of energy loss in the samples confined in the microfluidic microcantilever sensor offers new platform for biosensing of picoliter volumes of samples. Compared to other micro/nano arrays applied for biosensing such as nanoparticles[10,35], SPR[295–297], and plane

cantilevers[36,37], the microfluidic cantilever measures the dynamic process and the mechanical properties involved in the bioprocesses without the need for surface immobilizations. This concept can also be used for dissipation based samples analysis in multiple fields. By observing the nanomechanical property change, novel understanding and discovery in biological processes and reactions will be achieved.

Chapter 7. Conclusions and Future Work

In this thesis, we focused on developing fast-scan, label-free biosensing systems with high specificity, sensitivity, and reliability. This specificity is achieved by applying target specific sensing layer molecules including antimicrobial peptides (AMPs), proteins, conjugated smart polymers and so on. By optimizing the sensing layers, the functionalized sensors are capable to detection targets from whole cells to small molecules. The highly-sensitive, fast-scan detection is achieved by utilizing microcantilever sensor platforms, which is capable of detecting analytes to picomolar range. Compared with other sensor platforms, the MCL sensors monitors the nanomechanical interactions of the biological process. With the help of microfabrication techniques, sensor chips dimensions are minimized to micro/nano scale, which enhance the detection performance and reduce sample volume. These types of micro/nano sized sensors can lead to the application of lab-on-a-chip technique in food and water monitoring, water screening, and clinical diagnostics and evaluations.

7.1 Conclusions

In chapter 3, we designed and screened the short peptide fragments from Class IIa bacteriocins as recognition elements for *L. monocytogenes* detection. MCL sensor platform is utilized as a tool for screening and validating high binding peptides. This work highlighted the short peptide fragments with a similar binding affinity with full sequence

bacteriocin, which is a more optimum sensing layer with reduced cost and improved stability.

In chapter 4, we investigated the pH-dependent conformational isomerization of human serum albumin (HSA) using microcantilever sensing platform. Native and denatured HSA proteins were immobilized on cantilever surfaces to understand the effect of pH on conformational changes caused by the effect of buffer pH. We demonstrated that the protonation and deprotonation of amino acid residues on proteins play a significant role in generating charge-induced cantilever bending. This protonation and deprotonation process was also monitored using SPR sensor. This detection methodology can be applied in disease detection related to protein misfolding or other conformational changes.

In chapter 5, we focused on detection of the small target using microcantilever and SPR sensors. A conjugated polymer interface consisting of an oxaborole containing polymer and a glycopolymer was used for achieving very high selectivity in dopamine (DA) detection. The optimum binding affinity between the polymers promotes the selectivity to DA through a displacement mechanism while remaining unaffected by other structurally related analogs and saccharide derivatives. Using the conjugated polymer sensing layer, the SPR biosensor was capable of detecting DA in the concentration range of 1×10^{-9} to 1×10^{-4} mol L^{-1} while the MCL sensor showed a limit of detection (LOD) of 50 pM. We find that the sensing mechanism is based on DA-induced reversible swelling of the conjugated polymer layer and this allows regeneration and reuse of the sensor multiple times. Also, we conclude that SPR is a suitable sensor platform for DA in-line detection at clinical level considering the detection time and stability, while MCL can achieve a much

lower LOD. This study gives perspectives about sensing layer design and transducer selection for different applications. The different sensing mechanisms of transducers will affect the LOD, working range and detection time, efficiency in sensor development.

In chapter 6, we used the microfluidic microcantilever for monitoring DNA melting process. A resonating microfluidic cantilever, with DNA solution confined in it, has been used for mechanically detecting the melting process. By real-time monitoring the temperature dependent variation in the cantilever resonance response, the thermodynamic and nanomechanical variations of the DNA melting process have been analyzed for 100-picoliter volumes of the samples with varied oligomer lengths, ionic strengths, and existence of different chemicals. These nanomechanical variations in the DNA sample provide a better understanding of the melting process and provide complementary information to the traditional UV absorption measurements. This methodology opens up new avenues for mechanical monitoring of biological reactions and processes.

In conclusion, we have developed multiple MEMs based biosensors targeting whole cell recognition, protein conformational change, and small molecules such as neurotransmitters detection. By designing and optimizing the sensing layers-target interfaces, highly specific biosensors are developed for label-free pathogen detection in food and water samples with significantly increased specificity and stability. By utilizing the nanomechanical property variation during the biological process, analytes can be detected and quantified per requirement. By creating effective sensing layer-transducer interfaces, fast-scan detection was achieved with a limit of detection comparable or beyond the clinical-relevant level.

Future biosensors can be designed accordingly for each specific target with the knowledge and principles developed in this thesis.

7.2 Future Work

In a foreseeable future, production of transducers with a much-reduced scale will be achieved. Thus, the sensitivity and limit of detection of the sensors can be increased to a level that can satisfy most of the biosensing applications. The challenge of biosensors developing still lies in selectivity development, sensing system scaling down, reliability and regeneration optimization and detection time and efficiency improvement.

One future direction is developing multichannel sensors. In real samples, there are usually multiple cells or molecules coexisting. It is beneficial if multiple targets/biomarkers can be quantified in one batch of detection. To achieve that, sensors with multiple channels are in demand. For example, the current MicroMotiv Octosense MCL array has 8 microcantilever beams which can be functionalized with 8 different sensing layers. Potentially, it can be developed as a sensor detecting 8 targets at the same time (we demonstrated it can detect 4 targets simultaneously). With the new design of sensor arrays parallelly, a biosensing system will be capable of detecting multiple analytes in real time, which will increase the diagnostic efficiency and accuracy.

Another important aspect is to continue studying the interfaces between different components in order to enhance the selectivity. We have explored the specific binding between AMPs and different bacteria strains and proved its specificity on various sensor

platforms. Comparing with widely used antibody sensing layer, these peptides have much-improved stability in harsh environments that increase the shelf life of the biosensors. Also, the fragments of AMPs have been proved to be active against the strains as well, which lead to further simplification of the sensing layer molecules. By screening and building the library of active peptide fragments, most effective sensing layer can be determined. As a result, biosensor stability and efficiency will be improved. In chapter 6, we discovered the polymer functionalized sensors have higher stability than peptide functionalized sensors. In the future, by studying the binding mechanism between AMPs and bacteria strains, it is possible to design biomimicry polymers which will have similar binding activity with AMPs. Thus, they can be widely used on label-free pathogen sensor productions.

Searching for novel targets/biomarker and their corresponding sensing molecules is another urgent task for biosensor development. As we developed sensors for circulating tumor cell (CTC) detection, the challenge still lies in as the low CTC amount existing in the circulation system. As one key factor for cancer treatment is early-stage-diagnosis, sensors targeting other cancer markers are needed. Researchers have been using other biomarkers such as metabolites, proteins for cancer detection and diagnosis. Exosomes, as cell-derived vesicles with a size less than 100 nm have recently attracted lots of attention. Via different proteins and DNAs, exosomes carry information of its origin cells. Thus, it is an ideal target as a cancer biomarker. Biosensors based on exosomes have been developed and being further improved. Keeping discovering and designing new sensing layer is one key factor to push biosensors evolution.

Mechanical interaction is one of the fundamental physical properties of biology. Microfluidic cantilever platform has been demonstrated to be ideal for studying the nanomechanical and thermodynamic properties variation during biological processes. These properties can be quantified with microfluidic cantilever platform. Statistical mechanic theories can be applied to explain these property variations, which will lead to breakthroughs in physical biology. It will also bring in new insight in sensor design and development.

Integration current sensor platforms with other techniques (e.g. spectroscopy) can also lead to new breakthroughs. For example, mid-infrared (MIR) spectroscopy gives "fingerprint" information about molecular vibration which is widely used for molecular recognition. Using a MIR laser, it is possible to excite the molecules adsorbed on the sensor surface and produce a thermal induced signal. Thus, molecular recognition can be achieved by this additional technique without the requirement of surface functionalization. However, further effort is needed for recognizing large molecules or even whole cells. By integrating MIR with bi-material microfluidic cantilevers (BMC), molecular recognition can be achieved in finite sample volume, with low sample concentration.

Besides all the possible future work in biosensing area, the knowledge, experience, and understanding from this thesis can be applied in multiple other areas. With new designs of sensing layer, physical transducers and so on, there are many possible fields that the principle and knowledge of the sensor interfaces development can be applied. Here, as an example, we have employed MEMs sensor to study the stress and anode material expansion in battery charge/discharge process.

7.2.1 Exploring the sodium storage mechanism in few-layers molybdenum disulfide from the stress

The emerging of electrical vehicles and powerful hand-held personal data devices has provoked the intensive research in high-capacity electrode materials for both Li-ion and Na-ion batteries. MoS_2 possesses a well-known 2D structure, with a large interlayer space of 6.15 Å, is one of the anode materials which attract great attention from researchers.[298]. The persistent challenge in high capacity anode materials is the large volume fluctuation during ion intercalation/extraction, which eventually leads to the electrode failure. Despite the fact that some nanoscale engineered electrode structures show promise in handling the volume fluctuation, it remains critical to understand the real-time intrinsic chemical and physical changes in the electrode, which provide guidelines for future electrode design.[299,300] Various in situ characterization technologies have been developed for this purpose.[301–303] In situ TEM reveals the volume expansion and pulverization of these high-capacity electrode materials in charge/discharge process.[304,305] In situ AFM provides additional mechanical information of electrodes, such as the formation of solid-electrolyte interface (SEI) layer and Young's modulus of both electrodes.[306,307] However, both techniques provide a limited quantified understanding of the stress.

With the ultrahigh sensitivity, microcantilever can be utilized to solve one problem in sodium (Na)-ion batteries (SIB): the stress induced in few-layers MoS_2 upon the intercalation and extraction of Na. The MoS_2 thin film was deposited on microcantilever surface with basal plane parallel to cantilever surface, which makes the system particularly sensitive to the stress in basal plane. For 2D materials, it is critical to understand the stress

in the basal plane since these materials often interact with substrates with their basal plane and stress in basal plane is directly applied on the substrate.

MoS_2 thin films will be deposited on silver coated MCLs via pulsed laser deposition (PLD). The deposited MoS2 thin film will be characterized by multiple approaches such as: X-ray diffraction, Raman spectroscopy, Scanning helium ion microscopy (HiM) and atomic force microscopy (AFM). The electrolyte will be 1 M $NaClO_4$ in ethylene carbonate/diethyl carbonate (1:1). Galvanostatic charge-discharge cycling will be performed on a Solatron 1470E Multichannel Potentiostat/CellTest System. The cantilever will be mounted in a homemade liquid cell with pre-fixed platinum (Pt) electrodes (**Figure 7.1**). Cantilever deflection will be monitored using a homemade system with NI DAQ and LabView based software for data acquisition following similar methods mentioned in Chapter 3, 4 and 5. The surface stress on cantilever will be calculated according to Stoney's formula.[219]

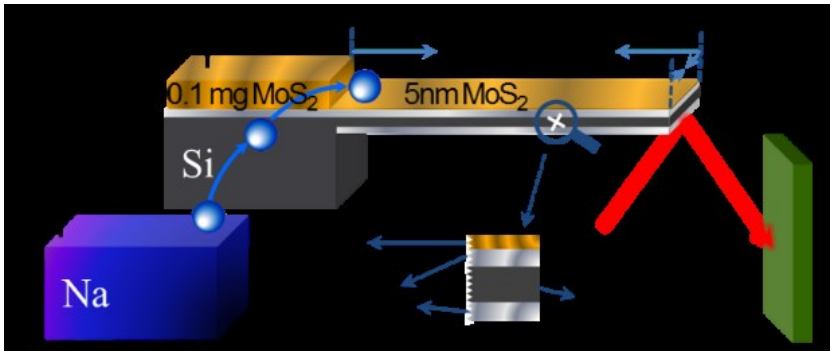

Figure 7.1 The schematic illustration of the microcantilever system to detect the sodiation /desodiation induced stress in few-layers MoS_2;

This work will provide fundamental insights into the stress evolution in various charge/discharge stages of the MoS_2 thin film. With ideal electrochemical environments, the microcantilever platform is sensitive enough to distinguish the stress generated in few layers MoS_2 from the impact of the electrical double layer. The protocol developed in this work can be readily adapted to resolve the stress in wide-range of electrode materials and gain additional insights into the charge storage mechanism. The fundamental understanding of stress will pave the road for long life battery design.

7.2.2 Summary

To sum up, by optimizing and designing new sensing layers and combining them with MEMs sensor platform with high sensitivity, there are multiple novel biosensors can be developed. Using nanomechanical sensor for monitoring biological processes can bring

new insights for fundamental biology research and sensor development. By further understanding the physics and chemistry between the analytes, sensing layer, physical transducer, and their interfaces, MEMs/NEMs sensors can be designed to inquiries and applied in multiple fields.

Biosensing is a topic with urgent demand and huge market. Developing highly-sensitive, highly-specific, low-cost sensors will benefit not only the scientific research, but the improvement of human life. Nanomechanical sensing technique is one promising platform for fundamental researches and practical applications.

Bibliography

(1) Eggins, B. R. *Chemical Sensors and Biosensors*; John Wiley & Sons, 2008.

(2) Kasemo, B. Biological Surface Science. *Surf. Sci.* **2002**, *500*, 656–677.

(3) Raiteri, R.; Grattarola, M.; Butt, H.-J.; Skládal, P. Micromechanical Cantilever-Based Biosensors. *Sens. Actuators B Chem.* **2001**, *79*, 115–126.

(4) Carrascosa, L. G.; Moreno, M.; Álvarez, M.; Lechuga, L. M. Nanomechanical Biosensors: A New Sensing Tool. *TrAC Trends Anal. Chem.* **2006**, *25*, 196–206.

(5) Fritz, J. Cantilever Biosensors. *Analyst* **2008**, *133*, 855–863.

(6) CLARK, L. C., Jr; LYONS, C. Electrode Systems for Continuous Monitoring in Cardiovascular Surgery. *Ann. N. Y. Acad. Sci.* **1962**, *102*, 29–45.

(7) Anker, J. N.; Hall, W. P.; Lyandres, O.; Shah, N. C.; Zhao, J.; Van Duyne, R. P. Biosensing with Plasmonic Nanosensors. *Nat. Mater.* **2008**, *7*, 442–453.

(8) Arlett, J. L.; Myers, E. B.; Roukes, M. L. Comparative Advantages of Mechanical Biosensors. *Nat. Nanotechnol.* **2011**, *6*, 203–215.

(9) Weizmann, Y.; Patolsky, F.; Willner, I. Amplified Detection of DNA and Analysis of Single-Base Mismatches by the Catalyzed Deposition of Gold on Au-Nanoparticles. *Analyst* **2001**, *126*, 1502–1504.

(10) Goluch, E. D.; Nam, J.-M.; Georganopoulou, D. G.; Chiesl, T. N.; Shaikh, K. A.; Ryu, K. S.; Barron, A. E.; Mirkin, C. A.; Liu, C. A Bio-Barcode Assay for on-Chip Attomolar-Sensitivity Protein Detection. *Lab. Chip* **2006**, *6*, 1293–1299.

(11) Sung, Y. J.; Suk, H.-J.; Sung, H. Y.; Li, T.; Poo, H.; Kim, M.-G. Novel Antibody/Gold Nanoparticle/Magnetic Nanoparticle Nanocomposites for Immunomagnetic Separation and Rapid Colorimetric Detection of Staphylococcus Aureus in Milk. *Biosens. Bioelectron.* **2013**, *43*, 432–439.

(12) Varshney, M.; Li, Y. Interdigitated Array Microelectrode Based Impedance Biosensor Coupled with Magnetic Nanoparticle-Antibody Conjugates for Detection of Escherichia Coli O157 : H7 in Food Samples. *Biosens. Bioelectron.* **2007**, *22*, 2408–2414.

(13) Zhang, J.; Lang, H. P.; Battiston, F.; Backmann, N.; Huber, F.; Gerber, C. Development of Robust and Standardized Cantilever Sensors Based on Biotin/Neutravidin Coupling for Antibody Detection. *Sensors* **2013**, *13*, 5273–5285.

(14) Wilson, R.; Turner, A. P. F. Glucose Oxidase: An Ideal Enzyme. *Biosens. Bioelectron.* **1992**, *7*, 165–185.

(15) Wang, N.; He, M.; Shi, H.-C. Novel Indirect Enzyme-Linked Immunosorbent Assay (ELISA) Method to Detect Total E. Coli in Water Environment. *Anal. Chim. Acta* **2007**, *590*, 224–231.

(16) Johnson, R.; Durham, R.; Johnson, S.; Macdonald, L.; Jeffrey, S.; Butman, B. Detection of Escherichia-Coli O157-H7 in Meat by an Enzyme-Linked-Immunosorbent-Assay, Ehec-Tek. *Appl. Environ. Microbiol.* **1995**, *61*, 386–388.

(17) Zen, J.-M.; Kumar, A. S. A Mimicking Enzyme Analogue for Chemical Sensors. *Acc. Chem. Res.* **2001**, *34*, 772–780.

(18) Duncan, B.; Le, N. D. B.; Alexander, C.; Gupta, A.; Yesilbag Tonga, G.; Yazdani, M.; Landis, R. F.; Wang, L.-S.; Yan, B.; Burmaoglu, S.; *et al.* Sensing by Smell: Nanoparticle–Enzyme Sensors for Rapid and Sensitive Detection of Bacteria with Olfactory Output. *ACS Nano* **2017**, *11*, 5339–5343.

(19) Liu, L.; Xia, N.; Liu, H.; Kang, X.; Liu, X.; Xue, C.; He, X. Highly Sensitive and Label-Free Electrochemical Detection of microRNAs Based on Triple Signal Amplification of Multifunctional Gold Nanoparticles, Enzymes and Redox-Cycling Reaction. *Biosens. Bioelectron.* **2014**, *53*, 399–405.

(20) Njagi, J.; Chernov, M. M.; Leiter, J. C.; Andreescu, S. Amperometric Detection of Dopamine in Vivo with an Enzyme Based Carbon Fiber Microbiosensor. *Anal. Chem.* **2010**, *82*, 989–996.

(21) Zasloff, M. Antimicrobial Peptides of Multicellular Organisms. *Nature* **2002**, *415*, 389–395.

(22) Mannoor, M. S.; Tao, H.; Clayton, J. D.; Sengupta, A.; Kaplan, D. L.; Naik, R. R.; Verma, N.; Omenetto, F. G.; McAlpine, M. C. Graphene-Based Wireless Bacteria Detection on Tooth Enamel. *Nat. Commun.* **2012**, *3*, 763.

(23) Etayash, H.; Norman, L.; Thundat, T.; Kaur, K. Peptide-Bacteria Interactions Using Engineered Surface-Immobilized Peptides from Class IIa Bacteriocins. *Langmuir* **2013**, *29*, 4048–4056.

(24) Farkas-Himsley, H. Bacteriocins--Are They Broad-Spectrum Antibiotics? *J. Antimicrob. Chemother.* **1980**, *6*, 424–426.

(25) Gratia, J. P. Andr? Gratia: A Forerunner in Microbial and Viral Genetics. *Genetics* **2000**, *156*, 471–476.

(26) Ennahar, S.; Sonomoto, K.; Ishizaki, A. Class IIa Bacteriocins from Lactic Acid Bacteria: Antibacterial Activity and Food Preservation. *J. Biosci. Bioeng.* **1999**, *87*, 705–716.

(27) Johnsen, L.; Fimland, G.; Nissen-Meyer, J. The C-Terminal Domain of Pediocin-like Antimicrobial Peptides (Class IIa Bacteriocins) Is Involved in Specific Recognition of the C-Terminal Part of Cognate Immunity Proteins and in Determining the Antimicrobial Spectrum. *J. Biol. Chem.* **2005**, *280*, 9243–9250.

(28) Fimland, G.; Johnsen, L.; Dalhus, B.; Nissen-Meyer, J. Pediocin-like Antimicrobial Peptides (Class IIa Bacteriocins) and Their Immunity Proteins: Biosynthesis, Structure, and Mode of Action. *J. Pept. Sci.* **2005**, *11*, 688–696.

(29) Jacquet, T.; Cailliez-Grimal, C.; Francius, G.; Borges, F.; Imran, M.; Duval, J. F. L.; Revol-Junelles, A.-M. Antibacterial Activity of Class IIa Bacteriocin Cbn BM1 Depends on the Physiological State of the Target Bacteria. *Res. Microbiol.* **2012**, *163*, 323–331.

(30) Kjos, M.; Nes, I. F.; Diep, D. B. Class II One-Peptide Bacteriocins Target a Phylogenetically Defined Subgroup of Mannose Phosphotransferase Systems on Sensitive Cells. *Microbiol. Read. Engl.* **2009**, *155*, 2949–2961.

(31) Ramnath, M.; Arous, S.; Gravesen, A.; Hastings, J. W.; Héchard, Y. Expression of mptC of Listeria Monocytogenes Induces Sensitivity to Class IIa Bacteriocins in Lactococcus Lactis. *Microbiol. Read. Engl.* **2004**, *150*, 2663–2668.

(32) Gerard, F.; Pradel, N.; Wu, L. F. Bactericidal Activity of Colicin V Is Mediated by an Inner Membrane Protein, SdaC, of Escherichia Coli. *J. Bacteriol.* **2005**, *187*, 1945–1950.

(33) Waters, V.; Crosa, J. Colicin-V Virulence Plasmids. *Microbiol. Rev.* **1991**, *55*, 437–450.

(34) Organization, W. H. *Microbiological Hazards in Fresh Leafy Vegetables and Herbs: Meeting Report*; World Health Organization, **2008**.

(35) Mirkin, C. A.; Letsinger, R. L.; Mucic, R. C.; Storhoff, J. J. A DNA-Based Method for Rationally Assembling Nanoparticles into Macroscopic Materials. *Nature* **1996**, *382*, 607–609.

(36) Biswal, S. L.; Raorane, D.; Chaiken, A.; Birecki, H.; Majumdar, A. Nanomechanical Detection of DNA Melting on Microcantilever Surfaces. *Anal. Chem.* **2006**, *78*, 7104–7109.

(37) Hansen, K. M.; Ji, H.-F.; Wu, G.; Datar, R.; Cote, R.; Majumdar, A.; Thundat, T. Cantilever-Based Optical Deflection Assay for Discrimination of DNA Single-Nucleotide Mismatches. *Anal. Chem.* **2001**, *73*, 1567–1571.

(38) Kahn, J. S.; Hu, Y.; Willner, I. Stimuli-Responsive DNA-Based Hydrogels: From Basic Principles to Applications. *Acc. Chem. Res.* **2017**, *50*, 680–690.

(39) Du, Y.; Dong, S. Nucleic Acid Biosensors: Recent Advances and Perspectives. *Anal. Chem.* **2017,** *89*, 189-215.

(40) Zhou, W.; Chen, Q.; Huang, P.-J. J.; Ding, J.; Liu, J. DNAzyme Hybridization, Cleavage, Degradation and Sensing in Undiluted Human Blood Serum. *Anal. Chem.* **2015**, *87*, 4001-4007.

(41) Mathur, D.; Medintz, I. L. Analyzing DNA Nanotechnology: A Call to Arms For The Analytical Chemistry Community. *Anal. Chem.* **2017**, *89*, 2646–2663.

(42) Shaibani, P. M.; Jiang, K.; Haghighat, G.; Hassanpourfard, M.; Etayash, H.; Naicker, S.; Thundat, T. The Detection of Escherichia Coli (E. Coli) with the pH Sensitive Hydrogel Nanofiber-Light Addressable Potentiometric Sensor (NF-LAPS). *Sens. Actuators B Chem.* **2016**, *226*, 176–183.

(43) Ji, H. F.; Thundat, T. In Situ Detection of Calcium Ions with Chemically Modified Microcantilevers. *Biosens. Bioelectron.* **2002**, *17*, 337–343.

(44) Culver, H. R.; Clegg, J. R.; Peppas, N. A. Analyte-Responsive Hydrogels: Intelligent Materials for Biosensing and Drug Delivery. *Acc. Chem. Res.* **2017**, *50*, 170–178.

(45) Gu, Z.; Aimetti, A. A.; Wang, Q.; Dang, T. T.; Zhang, Y.; Veiseh, O.; Cheng, H.; Langer, R. S.; Anderson, D. G. Injectable Nano-Network for Glucose-Mediated Insulin Delivery. *ACS Nano* **2013**, *7*, 4194–4201.

(46) Baker, G. A.; Desikan, R.; Thundat, T. Label-Free Sugar Detection Using Phenylboronic Acid-Functionalized Piezoresistive Microcantilevers. *Anal. Chem.* **2008**, *80*, 4860–4865.

(47) Hennemeyer, M.; Burghardt, S.; Stark, R. W. Cantilever Micro-Rheometer for the Characterization of Sugar Solutions. *Sensors* **2008**, *8*, 10–22.

(48) Sargent, A.; Loi, T.; Gal, S.; Sadik, O. A. The Electrochemistry of Antibody-Modified Conducting Polymer Electrodes. *J. Electroanal. Chem.* **1999**, *470*, 144–156.

(49) Ertl, P.; Mikkelsen, S. R. Electrochemical Biosensor Array for the Identification of Microorganisms Based on Lectin−Lipopolysaccharide Recognition. *Anal. Chem.* **2001**, *73*, 4241–4248.

(50) Schweiss, R.; Werner, C.; Knoll, W. Impedance Spectroscopy Studies of Interfacial Acid–base Reactions of Self-Assembled Monolayers. *J. Electroanal. Chem.* **2003**, *540*, 145–151.

(51) Esteban-Fernández de Ávila, B.; Escamilla-Gómez, V.; Campuzano, S.; Pedrero, M.; Pingarrón, J. M. Disposable Amperometric Magnetoimmunosensor for the Sensitive Detection of the Cardiac Biomarker Amino-Terminal pro-B-Type Natriuretic Peptide in Human Serum. *Anal. Chim. Acta* **2013**, *784*, 18–24.

(52) Jacobs, M.; Nagaraj, V. J.; Mertz, T.; Selvam, A. P.; Ngo, T.; Prasad, S. An Electrochemical Sensor for the Detection of Antibiotic Contaminants in Water. *Anal. Methods* **2013**, *5*, 4325–4329.

(53) Silley, P.; Forsythe, S. Impedance Microbiology—a Rapid Change for Microbiologists. *J. Appl. Bacteriol.* **1996**, *80*, 233–243.

(54) Wawerla, M.; Stolle, A.; Schalch, B.; Eisgruber, H. Impedance Microbiology: Applications in Food Hygiene. *J. Food Prot.* **1999**, *62*, 1488–1496.

(55) Saleem, M.; Rafiq, M.; Hanif, M. Organic Material Based Fluorescent Sensor for Hg2+: A Brief Review on Recent Development. *J. Fluoresc.* **2017**, *27*, 31–58.

(56) Xue, L.; Prifti, E.; Johnsson, K. A General Strategy for the Semisynthesis of Ratiometric Fluorescent Sensor Proteins with Increased Dynamic Range. *J. Am. Chem. Soc.* **2016**, *138*, 5258–5261.

(57) Zeng, L.; Miller, E. W.; Pralle, A.; Isacoff, E. Y.; Chang, C. J. A Selective Turn-On Fluorescent Sensor for Imaging Copper in Living Cells. *J. Am. Chem. Soc.* **2006**, *128*, 10–11.

(58) Xiao, Y.; Piorek, B. D.; Plaxco, K. W.; Heeger, A. J. A Reagentless Signal-On Architecture for Electronic, Aptamer-Based Sensors via Target-Induced Strand Displacement. *J. Am. Chem. Soc.* **2005**, *127*, 17990–17991.

(59) Ghindilis, A. L.; Schwarzkopf, K. R.; Messing, D. S.; Sezan, I.; Schuele, P.; Zhan, C.; Smith, M. W.; Simon, H. M.; Evans, D. R. Real-Time Biosensor Platform: Fully Integrated Device for Impedimetric Assays. In *Chemical Sensors 9 -and-Mems/Nems 9*; Hunter, G.; Aguilar, Z.; Li, J.; Davidson, J. L.; Shoji, S.; Sundaram, K. B.; Hesketh, P. J.; Carter, M.; Simonian, A.; Longdergan, A.; *et al.*, Eds.; 2010; Vol. 33, pp. 59–68.

(60) Yang, L.; Bashir, R. Electrical/Electrochemical Impedance for Rapid Detection of Foodborne Pathogenic Bacteria. *Biotechnol. Adv.* **2008**, *26*, 135–150.

(61) Wang, T.; Zhou, Y.; Lei, C.; Luo, J.; Xie, S.; Pu, H. Magnetic Impedance Biosensor: A Review. *Biosens. Bioelectron.* **2017**, *90*, 418–435.

(62) Maalouf, R.; Fournier-Wirth, C.; Coste, J.; Chebib, H.; Saïkali, Y.; Vittori, O.; Errachid, A.; Cloarec, J.-P.; Martelet, C.; Jaffrezic-Renault, N. Label-Free Detection of Bacteria by Electrochemical Impedance Spectroscopy: Comparison to Surface Plasmon Resonance. *Anal. Chem.* **2007**, *79*, 4879–4886.

(63) Dastider, S. G.; Barizuddin, S.; Dweik, M.; Almasri, M. A Micromachined Impedance Biosensor for Accurate and Rapid Detection of E. Coli O157:H7. *RSC Adv.* **2013**, *3*, 26297–26306.

(64) Qureshi, A.; Gurbuz, Y.; Kallempudi, S.; Niazi, J. H. Label-Free Capacitive E. Coli Biochip for Determining Chemicals That Induce Cellular Toxicity. *Procedia Eng.* **2011**, *25*, 928–931.

(65) Zhu, X.; Xu, H.; Lin, R.; Wang, Z.; Zheng, B.; Yang, G.; Chen, G. DNA Concatamers-Based Biosensor for Pb(II) Using Electrochemical Impedance Spectroscopy. *Anal. Methods* **2014**, *6*, 8886–8889.

(66) Ghindilis, A. L.; Smith, M. W.; Messing, D. S.; Haynes, V. N.; Middleton, G. B.; Schwarzkopf, K. R.; Campbell, C. E.; Zhan, C.; Ulrich, B.; Frasier, M. J.; *et al.* Development of Real-Time Assays for Impedance-Based Detection of Microbial Double-Stranded DNA Targets: Optimization and Data Analysis. *Biosens. Bioelectron.* **2012**, *35*, 87–93.

(67) Wang, X.; Li, Z.; Ly, N.; Zhou, F. One-Step Ligand Immobilization and Single Sample Injection for Regeneration-Free Surface Plasmon Resonance Measurements of Biomolecular Interactions. *Anal. Chem.* **2017**, *89*, 3261-3265.

(68) Oliveira, L. C.; Lima, A. M. N.; Thirstrup, C.; Neff, H. F. Introduction and Background Information. In *Surface Plasmon Resonance Sensors*; SpringerBriefs in Physics; Springer International Publishing, 2015; 1–9.

(69) Willets, K. A.; Duyne, R. P. V. Localized Surface Plasmon Resonance Spectroscopy and Sensing. *Annu. Rev. Phys. Chem.* **2007**, *58*, 267–297.

(70) Zeng, S.; Baillargeat, D.; Ho, H.-P.; Yong, K.-T. Nanomaterials Enhanced Surface Plasmon Resonance for Biological and Chemical Sensing Applications. *Chem. Soc. Rev.* **2014**, *43*, 3426–3452.

(71) Kumbhat, S.; Sharma, K.; Gehlot, R.; Solanki, A.; Joshi, V. Surface Plasmon Resonance Based Immunosensor for Serological Diagnosis of Dengue Virus Infection. *J. Pharm. Biomed. Anal.* **2010**, *52*, 255–259.

(72) Loget, G.; Wood, J. B.; Cho, K.; Halpern, A. R.; Corn, R. M. Electrodeposition of Polydopamine Thin Films for DNA Patterning and Microarrays. *Anal. Chem.* **2013**, *85*, 9991–9995.

(73) Zeng, C.; Huang, X.; Xu, J.; Li, G.; Ma, J.; Ji, H.-F.; Zhu, S.; Chen, H. Rapid and Sensitive Detection of Maize Chlorotic Mottle Virus Using Surface Plasmon Resonance-Based Biosensor. *Anal. Biochem.* **2013**, *440*, 18–22.

(74) Summanen, M.; Granqvist, N.; Tuominen, R. K.; Yliperttula, M.; Verrips, C. T.; Boonstra, J.; Blanchetot, C.; Ekokoski, E. Kinetics of PKCε Activating and

Inhibiting Llama Single Chain Antibodies and Their Effect on PKCε Translocation in HeLa Cells. *PLOS ONE* **2012**, *7*, e35630.

(75) Cooper, M. A. Optical Biosensors in Drug Discovery. *Nat. Rev. Drug Discov.* **2002**, *1*, 515–528.

(76) Chen, G. Y.; Thundat, T.; Wachter, E. A.; Warmack, R. J. Adsorption Induced Surface Stress and Its Effects on Resonance Frequency of Microcantilevers. *J. Appl. Phys.* **1995**, *77*, 3618–3622.

(77) Fritz, J.; Baller, M. K.; Lang, H. P.; Rothuizen, H.; Vettiger, P.; Meyer, E.; Güntherodt, H.; Gerber, C.; Gimzewski, J. K. Translating Biomolecular Recognition into Nanomechanics. *Science* **2000**, *288*, 316–318.

(78) Thundat, T.; Wachter, E. A.; Sharp, S. L.; Warmack, R. J. Detection of Mercury Vapor Using Resonating Microcantilevers. *Appl. Phys. Lett.* **1995**, *66*, 1695–1697.

(79) Thundat, T.; Warmack, R. J.; Chen, G. Y.; Allison, D. P. Thermal and Ambient Induced Deflections of Scanning Force Microscope Cantilevers. *Appl. Phys. Lett.* **1994**, *64*, 2894–2896.

(80) Lavrik, N. V.; Sepaniak, M. J.; Datskos, P. G. Cantilever Transducers as a Platform for Chemical and Biological Sensors. *Rev. Sci. Instrum.* **2004**, *75*, 2229–2253.

(81) Weeks, B. L.; Camarero, J.; Noy, A.; Miller, A. E.; De Yoreo, J. J.; Stanker, L. A Microcantilever-Based Pathogen Detector. *Scanning* **2003**, *25*, 297–299.

(82) Albrecht, T. R.; Akamine, S.; Carver, T. E.; Quate, C. F. Microfabrication of Cantilever Styli for the Atomic Force Microscope. *J. Vac. Sci. Technol. A* **1990**, *8*, 3386–3396.

(83) Hansen, K. M.; Thundat, T. Microcantilever Biosensors. *Methods* **2005**, *37*, 57–64.

(84) Stoney, G. *The Tension of Metallic Films Deposited by Electrolysis*; Royal Society of London, 1909.

(85) Berger, R.; Delamarche, E.; Lang, H. P.; Gerber, C.; Gimzewski, J. K.; Meyer, E.; Güntherodt, H.-J. Surface Stress in the Self-Assembly of Alkanethiols on Gold. *Science* **1997**, *276*, 2021–2024.

(86) Lang, H.; Baller, M.; Berger, R.; Gerber, C.; Gimzewski, J.; Battiston, F.; Fornaro, P.; Ramseyer, J. .; Meyer, E.; Güntherodt, H. . An Artificial Nose Based on a Micromechanical Cantilever Array. *Anal. Chim. Acta* **1999**, *393*, 59–65.

(87) Baller, M. .; Lang, H. .; Fritz, J.; Gerber, C.; Gimzewski, J. .; Drechsler, U.; Rothuizen, H.; Despont, M.; Vettiger, P.; Battiston, F. .; *et al.* A Cantilever Array-Based Artificial Nose. *Ultramicroscopy* **2000**, *82*, 1–9.

(88) Zhiyu Hu,, and; T. Thundat; R. J. Warmack. Investigation of Adsorption and Absorption-Induced Stresses Using Microcantilever Sensors. *J. Appl. Phys.* **2001**, *90*, 427–431.

(89) Savran, C. A.; Knudsen, S. M.; Ellington, A. D.; Manalis, S. R. Micromechanical Detection of Proteins Using Aptamer-Based Receptor Molecules. *Anal. Chem.* **2004**, *76*, 3194–3198.

(90) Grover, W. H.; Bryan, A. K.; Diez-Silva, M.; Suresh, S.; Higgins, J. M.; Manalis, S. R. Measuring Single-Cell Density. *Proc. Natl. Acad. Sci.* **2011**, *108*, 10992–10996.

(91) Burg, T. P.; Godin, M.; Knudsen, S. M.; Shen, W.; Carlson, G.; Foster, J. S.; Babcock, K.; Manalis, S. R. Weighing of Biomolecules, Single Cells and Single Nanoparticles in Fluid. *Nature* **2007**, *446*, 1066–1069.

(92) Etayash, H.; Khan, M. F.; Kaur, K.; Thundat, T. Microfluidic Cantilever Detects Bacteria and Measures Their Susceptibility to Antibiotics in Small Confined Volumes. *Nat. Commun.* **2016**, *7*.

(93) Khan, M. F.; Kim, S.; Lee, D.; Schmid, S.; Boisen, A.; Thundat, T. Nanomechanical Identification of Liquid Reagents in a Microfluidic Channel. *Lab. Chip* **2014**, *14*, 1302–1307.

(94) Fu, L.; Zhang, K.; Li, S.; Wang, Y.; Huang, T.-S.; Zhang, A.; Cheng, Z.-Y. In Situ Real-Time Detection of E. Coli in Water Using Antibody-Coated Magnetostrictive Microcantilever. *Sens. Actuators B Chem.* **2010**, *150*, 220–225.

(95) Shu, W.; Laue, E. D.; Seshia, A. A. Investigation of Biotin–streptavidin Binding Interactions Using Microcantilever Sensors. *Biosens. Bioelectron.* **2007**, *22*, 2003–2009.

(96) Psarra, E.; König, U.; Ueda, Y.; Bellmann, C.; Janke, A.; Bittrich, E.; Eichhorn, K.-J.; Uhlmann, P. Nanostructured Biointerfaces: Nanoarchitectonics of Thermoresponsive Polymer Brushes Impact Protein Adsorption and Cell Adhesion. *ACS Appl. Mater. Interfaces* **2015**, *7*, 12516–12529.

(97) Datar, R.; Kim, S.; Jeon, S.; Hesketh, P.; Manalis, S.; Boisen, A.; Thundat, T. Cantilever Sensors: Nanomechanical Tools for Diagnostics. *Mrs Bull.* **2009**, *34*, 449–454.

(98) Ndieyira, J. W.; Kappeler, N.; Logan, S.; Cooper, M. A.; Abell, C.; McKendry, R. A.; Aeppli, G. Surface-Stress Sensors for Rapid and Ultrasensitive Detection of Active Free Drugs in Human Serum. *Nat Nano* **2014**, *9*, 225–232.

(99) Ndieyira, J. W.; Watari, M.; Barrera, A. D.; Zhou, D.; Vögtli, M.; Batchelor, M.; Cooper, M. A.; Strunz, T.; Horton, M. A.; Abell, C.; *et al.* Nanomechanical Detection of Antibiotic–mucopeptide Binding in a Model for Superbug Drug Resistance. *Nat. Nanotechnol.* **2008**, *3*, 691–696.

(100) Zougagh, M.; Rios, A. Micro-Electromechanical Sensors in the Analytical Field. *Analyst* **2009**, *134*, 1274–1290.

(101) Samanta, D.; Sarkar, A. Immobilization of Bio-Macromolecules on Self-Assembled Monolayers: Methods and Sensor Applications. *Chem. Soc. Rev.* **2011**, *40*, 2567–2592.

(102) Gooding, J. J.; Ciampi, S. The Molecular Level Modification of Surfaces: From Self-Assembled Monolayers to Complex Molecular Assemblies. *Chem. Soc. Rev.* **2011**, *40*, 2704–2718.

(103) Seitz, O.; Fernandes, P. G.; Tian, R. H.; Karnik, N.; Wen, H. C.; Stiegler, H.; Chapman, R. A.; Vogel, E. M.; Chabal, Y. J. Control and Stability of Self-Assembled Monolayers under Biosensing Conditions. *J. Mater. Chem.* **2011**, *21*, 4384–4392.

(104) Legrange, J. D.; Markham, J. L.; Kurkjian, C. R. Effects of Surface Hydration on the Deposition of Silane Monolayers on Silica. *Langmuir* **1993**, *9*, 1749–1753.

(105) Dag Ruther; Tapas Sen; Daniel East; James Ian Bruce. Silicon, Silica and Its Surface Patterning/Activation with Alkoxy- and Amino-Silanes for Nanomedical Applications. *Nanomed.* **2011**, *6*, 281–300.

(106) Davis, F.; Higson, S. P. Structured Thin Films as Functional Components within Biosensors. *Biosens. Bioelectron.* **2005**, *21*, 1–20.

(107) Janet Petroski; Mei Chou; Carol Creutz. The Coordination Chemistry of Gold Surfaces: Formation and Far-Infrared Spectra of Alkanethiolate-Capped Gold Nanoparticles. *J. Organomet. Chem.* **2009**, *694*, 1138–1143.

(108) Ron, H.; Rubinstein, I. Self-Assembled Monolayers on Oxidized Metals. 3. Alkylthiol and Dialkyl Disulfide Assembly on Gold under Electrochemical Conditions. *J. Am. Chem. Soc.* **1998**, *120*, 13444–13452.

(109) George M. Whitesides; Paul E. Laibins. Wet Chemical Approaches to the Characterization of Organic Surfaces: Self-Assemled Monolayers, Wetting, and the Physical Organic Chemistry of the Solid-Liquid Interface. *Langmuir* **1990**, *6*, 87–96.

(110) Abraham Ulman. Formation and Structure of Self-Assembled Monolayers. *Chem. Rev.* **1996**, *96*, 1533–1554.

(111) Swapnil Kohale; Sara M Molina; Brandon L Weeks; Rajesh Khare; Loius J Hope-Weeks. Monitoring the Formation of Self-Assembled Monolayers of Alkanedithiols Using a Micromechanical Cantilever Sensor. *Langmuir* **2007**, *23*, 1258–1263.

(112) Bodapati, K. C.; Soudy, R.; Etayash, H.; Stiles, M.; Kaur, K. Design, Synthesis and Evaluation of Antimicrobial Activity of N-Terminal Modified Leucocin A Analogues. *Bioorg. Med. Chem.* **2013**, *21*, 3715–3722.

(113) Cotter, P. D.; Ross, R. P.; Hill, C. Bacteriocins - a Viable Alternative to Antibiotics? *Nat. Rev. Microbiol.* **2013**, *11*, 95–105.

(114) Drider, D.; Fimland, G.; Héchard, Y.; McMullen, L. M.; Prévost, H. The Continuing Story of Class IIa Bacteriocins. *Microbiol. Mol. Biol. Rev. MMBR* **2006**, *70*, 564–582.

(115) Derksen, D. J.; Stymiest, J. L.; Vederas, J. C. Antimicrobial Leucocin Analogues with a Disulfide Bridge Replaced by a Carbocycle or by Noncovalent Interactions of Allyl Glycine Residues. *J. Am. Chem. Soc.* **2006**, *128*, 14252–14253.

(116) Etayash, H.; Norman, L.; Thundat, T.; Kaur, K. Peptide-Bacteria Interactions Using Engineered Surface-Immobilized Peptides from Class IIa Bacteriocins. *Langmuir* **2013**, *29*, 4048–4056.

(117) Ascenzi, P.; Fasano, M. Allostery in a Monomeric Protein: The Case of Human Serum Albumin. *Biophys. Chem.* **2010**, *148*, 16–22.

(118) He, X.; Carter, D. Atomic-Structure and Chemistry of Human Serum-Albumin. *Nature* **1992**, *358*, 209–215.

(119) Sugio, S.; Kashima, A.; Mochizuki, S.; Noda, M.; Kobayashi, K. Crystal Structure of Human Serum Albumin at 2.5 Angstrom Resolution. *Protein Eng.* **1999**, *12*, 439–446.

(120) Kraghhansen, U. Structure and Ligand-Binding Properties of Human Serum-Albumin. *Dan. Med. Bull.* **1990**, *37*, 57–84.

(121) Ascenzi, P.; Bocedi, A.; Notari, S.; Fanali, G.; Fesce, R.; Fasano, M. Allosteric Modulation of Drug Binding to Human Serum Albumin. *Mini-Rev. Med. Chem.* **2006**, *6*, 483–489.

(122) Lacina, K.; Skladal, P.; James, T. D. Boronic Acids for Sensing and Other Applications - a Mini-Review of Papers Published in 2013. *Chem. Cent. J.* **2014**, *8*, 60.

(123) Kotsuchibashi, Y.; Agustin, R. V. C.; Lu, J.-Y.; Hall, D. G.; Narain, R. Temperature, pH, and Glucose Responsive Gels via Simple Mixing of Boroxole- and Glyco-Based Polymers. *Acs Macro Lett.* **2013**, *2*, 260–264.

(124) Ahmed, M.; Jawanda, M.; Ishihara, K.; Narain, R. Impact of the Nature, Size and Chain Topologies of Carbohydrate–phosphorylcholine Polymeric Gene Delivery Systems. *Biomaterials* **2012**, *33*, 7858–7870.

(125) Narain, R.; Armes, S. P. Synthesis of Low Polydispersity, Controlled-Structure Sugar Methacrylate Polymers under Mild Conditions without Protecting Group Chemistry. *Chem. Commun.* **2002**, 2776–2777.

(126) Narain, R.; Armes, S. P. Direct Synthesis and Aqueous Solution Properties of Well-Defined Cyclic Sugar Methacrylate Polymers. *Macromolecules* **2003**, *36*, 4675–4678.

(127) Dowlut, M.; Hall, D. G. An Improved Class of Sugar-Binding Boronic Acids, Soluble and Capable of Complexing Glycosides in Neutral Water. *J. Am. Chem. Soc.* **2006**, *128*, 4226–4227.

(128) Michel Godin; P. J. Williams; Vincent Tabard-Cossa; Olivier Laroche; L. Y. Beaulieu; R. B. Lennox; Peter Grutter. Surface Stress, Kinetics, and Structure of Alkanethiol Self-Assembled Monolayers. *Langmuir* **2004**, *20*, 7090–7096.

(129) Tabard-Cossa, V.; Godin, M.; Burgess, I. J.; Monga, T.; Lennox, R. B.; Grutter, P. Microcantilever-Based Sensors: Effect of Morphology, Adhesion, and Cleanliness of the Sensing Surface on Surface Stress. *Anal. Chem.* **2007**, *79*, 8136–8143.

(130) Headrick, J. J.; Sepaniak, M. J.; Lavrik, N. V.; Datskos, P. G. Enhancing Chemi-Mechanical Transduction in Microcantilever Chemical Sensing by Surface Modification. *Ultramicroscopy* **2003**, *97*, 417–424.

(131) Hongqing Pan; Yingming Xu; Sanhua Wu; Bailin Zhang; Jilin Tang. Molecular Interactions in Self-Assembly Monolayers on Gold-Coated Microcantilever Electrodes. *Nanotechnology* **2011**, *22*, 225503.

(132) Norman, L. L.; Badia, A. Microcantilevers Modified with Ferrocene-Terminated Self-Assembled Monolayers: Effect of Molecular Structure and Electrolyte Anion on the Redox-Induced Surface Stress. *J. Phys. Chem. C* **2011**, *115*, 1985–1995.

(133) Norman, L. L.; Badia, A. Redox Actuation of a Microcantilever Driven by a Self-Assembled Ferrocenylundecanethiolate Monolayer: An Investigation of the Origin of the Micromechanical Motion and Surface Stress. *J. Am. Chem. Soc.* **2009**, *131*, 2328–2337.

(134) Creager, S. E.; Rowe, G. K. Competitive Self-Assembly and Electrochemistry of Some Ferrocenyl-N-Alkanethiol Derivatives on Gold. *J. Electroanal. Chem.* **1994**, *370*, 203–211.

(135) Chapman, P. J.; Long, Z.; Datskos, P. G.; Archibald, R.; Sepaniak, M. J. Differentially Ligand-Functionalized Microcantilever Arrays for Metal Ion Identification and Sensing. *Anal. Chem.* **2007**, *79*, 7062–7068.

(136) Dutta, P.; Chapman, P. J.; Datskos, P. G.; Sepaniak, M. J. Characterization of Ligand-Functionalized Microcantilevers for Metal Ion Sensing. *Anal. Chem.* **2005**, *77*, 6601–6608.

(137) Cherian, S.; Mehta, A.; Thundat, T. Investigating the Mechanical Effects of Adsorption of Ca2+ Ions on a Silicon Nitride Microcantilever Surface. *Langmuir* **2002**, *18*, 6935–6939.

(138) Ji, H. F.; Finot, E.; Dabestani, R.; Thundat, T.; Brown, G. M.; Britt, P. F. A Novel Self-Assembled Monolayer (SAM) Coated Microcantilever for Low Level Caesium Detection. *Chem. Commun.* **2000**, 457–458.

(139) Costa, F.; Carvalho, I. F.; Montelaro, R. C.; Gomes, P.; Martins, M. C. L. Covalent Immobilization of Antimicrobial Peptides (AMPs) onto Biomaterial Surfaces. *Acta Biomater.* **2011**, *7*, 1431–1440.

(140) Khan, M. F.; Schmid, S.; Davis, Z. J.; Dohn, S.; Boisen, A. Fabrication of Resonant Micro Cantilevers with Integrated Transparent Fluidic Channel. *Microelectron. Eng.* **2011**, *88*, 2300–2303.

(141) Khan, M. F.; Schmid, S.; Larsen, P. E.; Davis, Z. J.; Yan, W.; Stenby, E. H.; Boisen, A. Online Measurement of Mass Density and Viscosity of pL Fluid Samples with Suspended Microchannel Resonator. *Sens. Actuators B Chem.* **2013**, *185*, 456–461.

(142) Gracias, K. S.; McKillip, J. L. A Review of Conventional Detection and Enumeration Methods for Pathogenic Bacteria in Food. *Can. J. Microbiol.* **2004**, *50*, 883–890.

(143) Sen, K.; Sinclair, J. L.; Boczek, L.; Rice, E. W. Development of a Sensitive Detection Method for Stressed E. Coli O157:H7 in Source and Finished Drinking Water by Culture-qPCR. *Environ. Sci. Technol.* **2011**, *45*, 2250–2256.

(144) Elizaquivel, P.; Sanchez, G.; Selma, M. V.; Aznar, R. Application of Propidium Monoazide-qPCR to Evaluate the Ultrasonic Inactivation of Escherichia Coli O157:H7 in Fresh-Cut Vegetable Wash Water. *Food Microbiol.* **2012**, *30*, 316–320.

(145) Lund, B. M.; O'Brien, S. J. The Occurrence and Prevention of Foodborne Disease in Vulnerable People. *Foodborne Pathog. Dis.* **2011**, *8*, 961–973.

(146) Schlech, W.; Lavigne, P.; Bortolussi, R.; Allen, A.; Haldane, E.; Wort, A.; Hightower, A.; Johnson, S.; King, S.; Nicholls, E.; *et al.* Epidemic Listeriosis - Evidence for Transmission by Food. *N. Engl. J. Med.* **1983**, *308*, 203–206.

(147) Radke, S. A.; Alocilja, E. C. A High Density Microelectrode Array Biosensor for Detection of E-Coli O157 : H7. *Biosens. Bioelectron.* **2005**, *20*, 1662–1667.

(148) He, L.; Deen, B. D.; Pagel, A. H.; Diez-Gonzalez, F.; Labuza, T. P. Concentration, Detection and Discrimination of Bacillus Anthracis Spores in Orange Juice Using

Aptamer Based Surface Enhanced Raman Spectroscopy. *Analyst* **2013**, *138*, 1657–1659.

(149) Mannoor, M. S.; Zhang, S.; Link, A. J.; McAlpine, M. C. Electrical Detection of Pathogenic Bacteria via Immobilized Antimicrobial Peptides. *Proc. Natl. Acad. Sci. U. S. A.* **2010**, *107*, 19207–19212.

(150) McAlpine, M. C.; Agnew, H. D.; Rohde, R. D.; Blanco, M.; Ahmad, H.; Stuparu, A. D.; Goddard, W. A.; Heath, J. R. Peptide-Nanowire Hybrid Materials for Selective Sensing of Small Molecules. *J. Am. Chem. Soc.* **2008**, *130*, 9583–9589.

(151) Wang, J.; Morton, M. J.; Elliott, C. T.; Karoonuthaisiri, N.; Segatori, L.; Biswal, S. L. Rapid Detection of Pathogenic Bacteria and Screening of Phage-Derived Peptides Using Microcantilevers. *Anal. Chem.* **2014**, *86*, 1671–1678.

(152) Etayash, H.; Jiang, K.; Thundat, T.; Kaur, K. Impedimetric Detection of Pathogenic Gram-Positive Bacteria Using an Antimicrobial Peptide from Class IIa Bacteriocins. *Anal. Chem.* **2014**, *86*, 1693–1700.

(153) Derksen, D. J.; Stymiest, J. L.; Vederas, J. C. Antimicrobial Leucocin Analogues with a Disulfide Bridge Replaced by a Carbocycle or by Noncovalent Interactions of Allyl Glycine Residues. *J. Am. Chem. Soc.* **2006**, *128*, 14252–14253.

(154) Bodapati, K. C.; Soudy, R.; Etayash, H.; Stiles, M.; Kaur, K. Design, Synthesis and Evaluation of Antimicrobial Activity of N-Terminal Modified Leucocin A Analogues. *Bioorg. Med. Chem.* **2013**, *21*, 3715–3722.

(155) Drider, D.; Fimland, G.; Hechard, Y.; McMullen, L. M.; Prevost, H. The Continuing Story of Class IIa Bacteriocins. *Microbiol. Mol. Biol. Rev.* **2006**, *70*, 564–+.

(156) Cotter, P. D.; Hill, C.; Ross, R. P. Bacteriocins: Developing Innate Immunity for Food. *Nat. Rev. Microbiol.* **2005**, *3*, 777–788.

(157) Kjos, M.; Nes, I. F.; Diep, D. B. Class II One-Peptide Bacteriocins Target a Phylogenetically Defined Subgroup of Mannose Phosphotransferase Systems on Sensitive Cells. *Microbiol.-Sgm* **2009**, *155*, 2949–2961.

(158) Ramnath, M.; Arous, S.; Gravesen, A.; Hastings, J. W.; Hechard, Y. Expression of mptC of Listeria Monocytogenes Induces Sensitivity to Class IIa Bacteriocins in Lactococcus Lactis. *Microbiol.-Sgm* **2004**, *150*, 2663–2668.

(159) Kjos, M.; Borrero, J.; Opsata, M.; Birri, D. J.; Holo, H.; Cintas, L. M.; Snipen, L.; Hernandez, P. E.; Nes, I. F.; Diep, D. B. Target Recognition, Resistance, Immunity and Genome Mining of Class II Bacteriocins from Gram-Positive Bacteria. *Microbiol.-Sgm* **2011**, *157*, 3256–3267.

(160) Majumdar, A. Bioassays Based on Molecular Nanomechanics. *Dis. Markers* **2002**, *18*, 167–174.

(161) Ji, H. F.; Yan, X. D.; Zhang, J.; Thundat, T. Molecular Recognition of Biowarfare Agents Using Micromechanical Sensors. *Expert Rev. Mol. Diagn.* **2004**, *4*, 859–866.

(162) Wu, G. H.; Datar, R. H.; Hansen, K. M.; Thundat, T.; Cote, R. J.; Majumdar, A. Bioassay of Prostate-Specific Antigen (PSA) Using Microcantilevers. *Nat. Biotechnol.* **2001**, *19*, 856–860.

(163) Desikan, R.; Armel, S.; Meyer, H. M.; Thundat, T. Effect of Chain Length on Nanomechanics of Alkanethiol Self-Assembly. *Nanotechnology* **2007**, *18*, 424028.

(164) Kim, D. J.; Weeks, B. L.; Hope-Weeks, L. J. Effect of Surface Conjugation Chemistry on the Sensitivity of Microcantilever Sensors. *Scanning* **2007**, *29*, 245–248.

(165) Tabard-Cossa, V.; Godin, M.; Burgess, I. J.; Monga, T.; Lennox, R. B.; Gruetter, P. Microcantilever-Based Sensors: Effect of Morphology, Adhesion, and Cleanliness of the Sensing Surface on Surface Stress. *Anal. Chem.* **2007**, *79*, 8136–8143.

(166) Ricciardi, C.; Castagna, R.; Ferrante, I.; Frascella, F.; Marasso, S. L.; Ricci, A.; Canavese, G.; Lore, A.; Prelle, A.; Gullino, M. L.; *et al.* Development of a Microcantilever-Based Immunosensing Method for Mycotoxin Detection. *Biosens. Bioelectron.* **2013**, *40*, 233–239.

(167) Fimland, G.; Blingsmo, O. R.; Sletten, K.; Jung, G.; Nes, I. F.; NissenMeyer, J. New Biologically Active Hybrid Bacteriocins Constructed by Combining Regions from Various Pediocin-like Bacteriocins: The C-Terminal Region Is Important for Determining Specificity. *Appl. Environ. Microbiol.* **1996**, *62*, 3313–3318.

(168) Kaur, K.; Andrew, L. C.; Wishart, D. S.; Vederas, J. C. Dynamic Relationships among Type IIa Bacteriocins: Temperature Effects on Antimicrobial Activity and

on Structure of the C-Terminal Amphipathic Alpha Helix as a Receptor-Binding Region. *Biochemistry (Mosc.)* **2004**, *43*, 9009–9020.

(169) Frank, R. The SPOT Synthesis Technique - Synthetic Peptide Arrays on Membrane Supports - Principles and Applications. *J. Immunol. Methods* **2002**, *267*, 13–26.

(170) Ahmed, S.; Mathews, A. S.; Byeon, N.; Lavasanifar, A.; Kaur, K. Peptide Arrays for Screening Cancer Specific Peptides. *Anal. Chem.* **2010**, *82*, 7533–7541.

(171) Soudy, R.; Ahmed, S.; Kaur, K. NGR Peptide Ligands for Targeting CD13/APN Identified through Peptide Array Screening Resemble Fibronectin Sequences. *Acs Comb. Sci.* **2012**, *14*, 590–599.

(172) Yoo, Y. K.; Chae, M.-S.; Kang, J. Y.; Kim, T. S.; Hwang, K. S.; Lee, J. H. Multifunctionalized Cantilever Systems for Electronic Nose Applications. *Anal. Chem.* **2012**, *84*, 8240–8245.

(173) Etayash, H.; Norman, L.; Thundat, T.; Stiles, M.; Kaur, K. Surface-Conjugated Antimicrobial Peptide Leucocin A Displays High Binding to Pathogenic Gram-Positive Bacteria. *Acs Appl. Mater. Interfaces* **2014**, *6*, 1131–1138.

(174) Jones, L. J.; Gray, M.; Yue, S. T.; Haugland, R. P.; Singer, V. L. Sensitive Determination of Cell Number Using the CyQUANT (R) Cell Proliferation Assay. *J. Immunol. Methods* **2001**, *254*, 85–98.

(175) Falsey, J. R.; Renil, M.; Park, S.; Li, S. J.; Lam, K. S. Peptide and Small Molecule Microarray for High Throughput Cell Adhesion and Functional Assays. *Bioconjug. Chem.* **2001**, *12*, 346–353.

(176) Veiseh, M.; Veiseh, O.; Martin, M. C.; Asphahani, F.; Zhang, M. Short Peptides Enhance Single Cell Adhesion and Viability on Microarrays. *Langmuir* **2007**, *23*, 4472–4479.

(177) Kaga, C.; Okochi, M.; Nakanishi, M.; Hayashi, H.; Kato, R.; Honda, H. Screening of a Novel Octamer Peptide, CNSCWSKD, That Induces Caspase-Dependent Cell Death. *Biochem. Biophys. Res. Commun.* **2007**, *362*, 1063–1068.

(178) Hilpert, K.; Hancock, R. E. W. Use of Luminescent Bacteria for Rapid Screening and Characterization of Short Cationic Antimicrobial Peptides Synthesized on Cellulose Using Peptide Array Technology. *Nat. Protoc.* **2007**, *2*, 1652–1660.

(179) Wang, Y. J.; Henz, M. E.; Gallagher, N. L. F.; Chai, S. Y.; Gibbs, A. C.; Yan, L. Z.; Stiles, M. E.; Wishart, D. S.; Vederas, J. C. Solution Structure of Carnobacteriocin B2 and Implications for Structure-Activity Relationships among Type IIa Bacteriocins from Lactic Acid Bacteria. *Biochemistry (Mosc.)* **1999**, *38*, 15438–15447.

(180) Gallagher, N. L. F.; Sailer, M.; Niemczura, W. P.; Nakashima, T. T.; Stiles, M. E.; Vederas, J. C. Three-Dimensional Structure of Leucocin A in Trifluoroethanol and Dodecylphophocholine Micelles: Spatial Location of Residues Critical for Biological Activity in Type IIa Bacteriocins from Lactic Acid Bacteria. *Biochemistry (Mosc.)* **1997**, *36*, 15062–15072.

(181) Wadhwani, P.; Strandberg, E.; van den Berg, J.; Mink, C.; Buerck, J.; Ciriello, R. A. M.; Ulrich, A. S. Dynamical Structure of the Short Multifunctional Peptide BP100 in Membranes. *Biochim. Biophys. Acta-Biomembr.* **2014**, *1838*, 940–949.

(182) Dannehl, C.; Gutsmann, T.; Brezesinski, G. Surface Activity and Structures of Two Fragments of the Human Antimicrobial LL-37. *Colloids Surf. B-Biointerfaces* **2013**, *109*, 129–135.

(183) Wu, G. H.; Ji, H. F.; Hansen, K.; Thundat, T.; Datar, R.; Cote, R.; Hagan, M. F.; Chakraborty, A. K.; Majumdar, A. Origin of Nanomechanical Cantilever Motion Generated from Biomolecular Interactions. *Proc. Natl. Acad. Sci. U. S. A.* **2001**, *98*, 1560–1564.

(184) Alvarez, M.; Carrascosa, L. G.; Zinoviev, K.; Plaza, J. A.; Lechuga, L. M. Biosensors Based on Cantilevers. In *Methods in Molecular Biology*; Rasooly, A.; Herold, K. E., Eds.; Alvarez, Mar; Inst Microelect Madrid, CIBER BBN, Madrid, Spain, 2009; Vol. 504, 51–71.

(185) Torun, O.; Boyaci, I. H.; Temur, E.; Tamer, U. Comparison of Sensing Strategies in SPR Biosensor for Rapid and Sensitive Enumeration of Bacteria. *Biosens. Bioelectron.* **2012**, *37*, 53–60.

(186) Bouguelia, S.; Roupioz, Y.; Slimani, S.; Mondani, L.; Casabona, M. G.; Durmort, C.; Vernet, T.; Calemczuk, R.; Livache, T. On-Chip Microbial Culture for the Specific Detection of Very Low Levels of Bacteria. *Lab. Chip* **2013**, *13*, 4024–4032.

(187) Lazcka, O.; Del Campo, F. J.; Munoz, F. X. Pathogen Detection: A Perspective of Traditional Methods and Biosensors. *Biosens. Bioelectron.* **2007**, *22*, 1205–1217.

(188) Sadik, O. A.; Aluoch, A. O.; Zhou, A. Status of Biomolecular Recognition Using Electrochemical Techniques. *Biosens. Bioelectron.* **2009**, *24*, 2749–2765.

(189) Fimland, G.; Eijsink, V. G. H.; Nissen-Meyer, J. Mutational Analysis of the Role of Tryptophan Residues in an Antimicrobial Peptide. *Biochemistry (Mosc.)* **2002**, *41*, 9508–9515.

(190) Solomon, E. I.; Lever, A. B. P. *Circular Dichroism and Linear Dichroism*; Wiley: New York, 2006.

(191) Santos, N. C.; Castanho, M. Fluorescence Spectroscopy Methodologies on the Study of Proteins and Peptides. On the 150 Th Anniversary of Protein Fluorescence. *Trends Appl. Spectrosc.* **2002**, *4*, 113–125.

(192) Jackson, M.; Mantsch, H. H. The Use and Misuse of FTIR Spectroscopy in the Determination of Protein Structure. *Crit. Rev. Biochem. Mol. Biol.* **1995**, *30*, 95–120.

(193) Schwalbe, H.; Rinnenthal, J. THERMODYNAMICS The World Is Flat. *Nat. Chem. Biol.* **2010**, *6*, 312–313.

(194) Diltemiz, S. E.; Hur, D.; Kecili, R.; Ersoz, A.; Say, R. New Synthesis Method for 4-MAPBA Monomer and Using for the Recognition of IgM and Mannose with MIP-Based QCM Sensors. *Analyst* **2013**, *138*, 1558–1563.

(195) Wang, D.; Tang, W.; Wu, X.; Wang, X.; Chen, G.; Chen, Q.; Li, N.; Liu, F. Highly Selective Detection of Single-Nucleotide Polymorphisms Using a Quartz Crystal Microbalance Biosensor Based on the Toehold-Mediated Strand Displacement Reaction. *Anal. Chem.* **2012**, *84*, 7008–7014.

(196) Tawil, N.; Sacher, E.; Mandeville, R.; Meunier, M. Strategies for the Immobilization of Bacteriophages on Gold Surfaces Monitored by Surface Plasmon Resonance and Surface Morphology. *J. Phys. Chem. C* **2013**, *117*, 6686–6691.

(197) Buchapudi, K. R.; Huang, X.; Yang, X.; Ji, H.-F.; Thundat, T. Microcantilever Biosensors for Chemicals and Bioorganisms. *Analyst* **2011**, *136*, 1539–1556.

(198) Iijima, M.; Somiya, M.; Yoshimoto, N.; Niimi, T.; Kuroda, S. Nano-Visualization of Oriented-Immobilized IgGs on Immunosensors by High-Speed Atomic Force Microscopy. *Sci. Rep.* **2012**, *2*, 790.

(199) Hu, Y.; Wang, K.; Zhang, Q.; Li, F.; Wu, T.; Niu, L. Decorated Graphene Sheets for Label-Free DNA Impedance Biosensing. *Biomaterials* **2012**, *33*, 1097–1106.

(200) Gruber, K.; Horlacher, T.; Castelli, R.; Mader, A.; Seeberger, P. H.; Hermann, B. A. Cantilever Array Sensors Detect Specific Carbohydrate-Protein Interactions with Picomolar Sensitivity. *Acs Nano* **2011**, *5*, 3670–3678.

(201) Mertens, J.; Tamayo, J.; Kosaka, P.; Calleja, M. Observation of Spermidine-Induced Attractive Forces in Self-Assembled Monolayers of Single Stranded DNA Using a Microcantilever Sensor. *Appl. Phys. Lett.* **2011**, *98*, 153704.

(202) Mader, A.; Gruber, K.; Castelli, R.; Hermann, B. A.; Seeberger, P. H.; Raedler, J. O.; Leisner, M. Discrimination of Escherichia Coli Strains Using Glycan Cantilever Array Sensors. *Nano Lett.* **2012**, *12*, 420–423.

(203) Yue, M.; Stachowiak, J. C.; Lin, H.; Datar, R.; Cote, R.; Majumdar, A. Label-Free Protein Recognition Two-Dimensional Array Using Nanomechanical Sensors. *Nano Lett.* **2008**, *8*, 520–524.

(204) Wu, G. H.; Ji, H. F.; Hansen, K.; Thundat, T.; Datar, R.; Cote, R.; Hagan, M. F.; Chakraborty, A. K.; Majumdar, A. Origin of Nanomechanical Cantilever Motion Generated from Biomolecular Interactions. *Proc. Natl. Acad. Sci. U. S. A.* **2001**, *98*, 1560–1564.

(205) Ricciardi, C.; Canavese, G.; Castagna, R.; Ferrante, I.; Ricci, A.; Marasso, S. L.; Napione, L.; Bussolino, F. Integration of Microfluidic and Cantilever Technology for Biosensing Application in Liquid Environment. *Biosens. Bioelectron.* **2010**, *26*, 1565–1570.

(206) Wee, K. W.; Kang, G. Y.; Park, J.; Kang, J. Y.; Yoon, D. S.; Park, J. H.; Kim, T. S. Novel Electrical Detection of Label-Free Disease Marker Proteins Using Piezoresistive Self-Sensing Micro-Cantilevers. *Biosens. Bioelectron.* **2005**, *20*, 1932–1938.

(207) Hansen, K. M.; Thundat, T. Microcantilever Biosensors. *Methods* **2005**, *37*, 57–64.

(208) Braun, T.; Ghatkesar, M. K.; Backmann, N.; Grange, W.; Boulanger, P.; Letellier, L.; Lang, H.-P.; Bietsch, A.; Gerber, C.; Hegner, M. Quantitative Time-Resolved Measurement of Membrane Protein-Ligand Interactions Using Microcantilever Array Sensors. *Nat. Nanotechnol.* **2009**, *4*, 179–185.

(209) Backmann, N.; Zahnd, C.; Huber, F.; Bietsch, A.; Plückthun, A.; Lang, H.-P.; Güntherodt, H.-J.; Hegner, M.; Gerber, C. A Label-Free Immunosensor Array Using Single-Chain Antibody Fragments. *Proc. Natl. Acad. Sci. U. S. A.* **2005**, *102*, 14587–14592.

(210) Maraldo, D.; Garcia, F. U.; Mutharasan, R. Method for Quantification of a Prostate Cancer Biomarker in Urine without Sample Preparation. *Anal. Chem.* **2007**, *79*, 7683–7690.

(211) Braun, T.; Backmann, N.; Vogtli, M.; Bietsch, A.; Engel, A.; Lang, H. P.; Gerber, C.; Hegner, M. Conformational Change of Bacteriorhodopsin Quantitatively Monitored by Microcantilever Sensors. *Biophys. J.* **2006**, *90*, 2970–2977.

(212) Ji, H.-F.; Gao, H.; Buchapudi, K. R.; Yang, X.; Xu, X.; Schulte, M. K. Microcantilever Biosensors Based on Conformational Change of Proteins. *Analyst* **2008**, *133*, 434–443.

(213) Siqueira, J. R.; Caseli, L.; Crespilho, F. N.; Zucolotto, V.; Oliveira, O. N. Immobilization of Biomolecules on Nanostructured Films for Biosensing. *Biosens. Bioelectron.* **2010**, *25*, 1254–1263.

(214) Yan, X.; Hill, K.; Gao, H.; Ji, H.-F. Surface Stress Changes Induced by the Conformational Change of Proteins. *Langmuir* **2006**, *22*, 11241–11244.

(215) Bashir, R.; Hilt, J. Z.; Elibol, O.; Gupta, A.; Peppas, N. A. Micromechanical Cantilever as an Ultrasensitive pH Microsensor. *Appl. Phys. Lett.* **2002**, *81*, 3091–3093.

(216) Ji, H. F.; Hansen, K. M.; Hu, Z.; Thundat, T. Detection of pH Variation Using Modified Microcantilever Sensors. *Sens. Actuators B-Chem.* **2001**, *72*, 233–238.

(217) Zhang, J.; Lang, H. P.; Yoshikawa, G.; Gerber, C. Optimization of DNA Hybridization Efficiency by pH-Driven Nanomechanical Bending. *Langmuir* **2012**, *28*, 6494–6501.

(218) Shaw, A. K.; Pal, S. K. Spectroscopic Studies on the Effect of Temperature on pH-Induced Folded States of Human Serum Albumin. *J. Photochem. Photobiol. B-Biol.* **2008**, *90*, 69–77.

(219) Stoney, G. G. The Tension of Metallic Films Deposited by Electrolysis. *Proc. R. Soc. Lond. Math. Phys. Eng. Sci.* **1909**, *82*, 172–175.

(220) Fragoso, A.; Laboria, N.; Latta, D.; O'Sullivan, C. K. Electron Permeable Self-Assembled Monolayers of Dithiolated Aromatic Scaffolds on Gold for Biosensor Applications. *Anal. Chem.* **2008**, *80*, 2556–2563.

(221) Frederix, F.; Bonroy, K.; Reekmans, G.; Laureyn, W.; Campitelli, A.; Abramov, M. A.; Dehaen, W.; Maes, G. Reduced Nonspecific Adsorption on Covalently Immobilized Protein Surfaces Using Poly(ethylene Oxide) Containing Blocking Agents. *J. Biochem. Biophys. Methods* **2004**, *58*, 67–74.

(222) Thakur, G.; Prashanthi, K.; Thundat, T. Directed Self-Assembly of Proteins into Discrete Radial Patterns. *Sci. Rep.* **2013**, *3*, 1923.

(223) Kiselev, M. A.; Gryzunov, Y. A.; Dobretsov, G. E.; Komarova, M. N. The Size of Human Serum Albumin Molecules in Solution. *Biofizika* **2001**, *46*, 423–427.

(224) Pico, G. A. Thermodynamic Features of the Thermal Unfolding of Human Serum Albumin. *Int. J. Biol. Macromol.* **1997**, *20*, 63–73.

(225) Sinha, S. S.; Mitra, R. K.; Pal, S. K. Temperature-Dependent Simultaneous Ligand Binding in Human Serum Albumin. *J. Phys. Chem. B* **2008**, *112*, 4884–4891.

(226) Michnik, A.; Michalik, K.; Kluczewska, A.; Drzazga, Z. Comparative DSC Study of Human and Bovine Serum Albumin. *J. Therm. Anal. Calorim.* **2006**, *84*, 113–117.

(227) Flora, K.; Brennan, J. D.; Baker, G. A.; Doody, M. A.; Bright, F. V. Unfolding of Acrylodan-Labeled Human Serum Albumin Probed by Steady-State and Time-Resolved Fluorescence Methods. *Biophys. J.* **1998**, *75*, 1084–1096.

(228) Wu, Y. Q.; Czarnik-Matusewicz, B.; Murayama, K.; Ozaki, Y. Two-Dimensional near-Infrared Spectroscopy Study of Human Serum Albumin in Aqueous Solutions: Using Overtones and Combination Modes to Monitor Temperature-Dependent Changes in the Secondary Structure. *J. Phys. Chem. B* **2000**, *104*, 5840–5847.

(229) Luong, T. Q.; Verma, P. K.; Mitra, R. K.; Havenith, M. Do Hydration Dynamics Follow the Structural Perturbation during Thermal Denaturation of a Protein: A Terahertz Absorption Study. *Biophys. J.* **2011**, *101*, 925–933.

(230) Mitra, R. K.; Sinha, S. S.; Pal, S. K. Hydration in Protein Folding: Thermal Unfolding/Refolding of Human Serum Albumin. *Langmuir* **2007**, *23*, 10224–10229.

(231) Baldwin, R. Temperature-Dependence of the Hydrophobic Interaction in Protein Folding. *Proc. Natl. Acad. Sci. U. S. A.* **1986**, *83*, 8069–8072.

(232) Cheung, M. S.; Garcia, A. E.; Onuchic, J. N. Protein Folding Mediated by Solvation: Water Expulsion and Formation of the Hydrophobic Core Occur after the Structural Collapse. *Proc. Natl. Acad. Sci. U. S. A.* **2002**, *99*, 685–690.

(233) Bellion, M.; Santen, L.; Mantz, H.; Haehl, H.; Quinn, A.; Nagel, A.; Gilow, C.; Weitenberg, C.; Schmitt, Y.; Jacobs, K. Protein Adsorption on Tailored Substrates: Long-Range Forces and Conformational Changes. *J. Phys.-Condens. Matter* **2008**, *20*, 404226.

(234) Saito, K.; Hamano, K.; Nakagawa, M.; Yugawa, K.; Muraoka, J.; Kuba, H.; Furukawa, K.; Azuma, T. Conformational Analysis of Human Serum Albumin and Its Non-Enzymatic Glycation Products Using Monoclonal Antibodies. *J. Biochem. (Tokyo)* **2011**, *149*, 569–580.

(235) Sota, H.; Hasegawa, Y.; Iwakura, M. Detection of Conformational Changes in an Immobilized Protein Using Surface Plasmon Resonance. *Anal. Chem.* **1998**, *70*, 2019–2024.

(236) Mannen, T.; Yamaguchi, S.; Honda, J.; Sugimoto, S.; Kitayama, A.; Nagamune, T. Observation of Charge State and Conformational Change in Immobilized Protein Using Surface Plasmon Resonance Sensor. *Anal. Biochem.* **2001**, *293*, 185–193.

(237) Gao, Y.; Li, X.; Guo, L.-H. Development of a Label-Free Competitive Ligand Binding Assay with Human Serum Albumin on a Molecularly Engineered Surface Plasmon Resonance Sensor Chip. *Anal. Methods* **2012**, *4*, 3718–3723.

(238) Gonon, F.; Buda, M.; Cespuglio, R.; Jouvet, M.; Pujol, J. Invivo Electrochemical Detection of Catechols in the Neostriatum of Anesthetized Rats - Dopamine or Dopac. *Nature* **1980**, *286*, 902–904.

(239) Keefe, K.; Zigmond, M.; Abercrombie, E. Invivo Regulation of Extracellular Dopamine in the Neostriatum - Influence of Impulse Activity and Local Excitatory Amino-Acids. *J. Neural Transm.-Gen. Sect.* **1993**, *91*, 223–240.

(240) Clark, J. J.; Sandberg, S. G.; Wanat, M. J.; Gan, J. O.; Horne, E. A.; Hart, A. S.; Akers, C. A.; Parker, J. G.; Willuhn, I.; Martinez, V.; *et al.* Chronic Microsensors for Longitudinal, Subsecond Dopamine Detection in Behaving Animals. *Nat. Methods* **2010**, *7*, 126-U58.

(241) Rao, P.; Rujikarn, N.; Luber, J.; Tyras, D. A Specific Sensitive Hplc Method for Determination of Plasma Dopamine. *Chromatographia* **1989**, *28*, 307–310.

(242) Woolley, A. T.; Lao, K. Q.; Glazer, A. N.; Mathies, R. A. Capillary Electrophoresis Chips with Integrated Electrochemical Detection. *Anal. Chem.* **1998**, *70*, 684–688.

(243) Fotopoulou, M. A.; Ioannou, P. C. Post-Column Terbium Complexation and Sensitized Fluorescence Detection for the Determination of Norepinephrine, Epinephrine and Dopamine Using High-Performance Liquid Chromatography. *Anal. Chim. Acta* **2002**, *462*, 179–185.

(244) Khan, A. F.; Brownson, D. A. C.; Randviir, E. P.; Smith, G. C.; Banks, C. E. 2D Hexagonal Boron Nitride (2D-hBN) Explored for the Electrochemical Sensing of Dopamine. *Anal. Chem.* **2016**, *88*, 9729–9737.

(245) Qi, L.; Thomas, E.; White, S. H.; Smith, S. K.; Lee, C. A.; Wilson, L. R.; Sombers, L. A. Unmasking the Effects of L-DOPA on Rapid Dopamine Signaling with an Improved Approach for Nafion Coating Carbon-Fiber Microelectrodes. *Anal. Chem.* **2016**, *88*, 8129–8136.

(246) Park, S. J.; Lee, S. H.; Yang, H.; Park, C. S.; Lee, C.-S.; Kwon, O. S.; Park, T. H.; Jang, J. Human Dopamine Receptor-Conjugated Multidimensional Conducting Polymer Nanofiber Membrane for Dopamine Detection. *Acs Appl. Mater. Interfaces* **2016**, *8*, 28897–28903.

(247) Zeng, Z.; Cui, B.; Wang, Y.; Sun, C.; Zhao, X.; Cui, H. Dual Reaction-Based Multimodal Assay for Dopamine with High Sensitivity and Selectivity Using Functionalized Gold Nanoparticles. *ACS Appl. Mater. Interfaces* **2015**, *7*, 16518–16524.

(248) Chen, C.-H.; Luo, S.-C. Tuning Surface Charge and Morphology for the Efficient Detection of Dopamine under the Interferences of Uric Acid, Ascorbic Acid, and Protein Adsorption. *Acs Appl. Mater. Interfaces* **2015**, *7*, 21931–21938.

(249) Guo, Z.; Seol, M.-L.; Kim, M.-S.; Ahn, J.-H.; Choi, Y.-K.; Liu, J.-H.; Huang, X.-J. Sensitive and Selective Electrochemical Detection of Dopamine Using an Electrode Modified with Carboxylated Carbonaceous Spheres. *Analyst* **2013**, *138*, 2683–2690.

(250) James, T. D.; Phillips, M. D.; Shinkai, S. Boronic Acids in Saccharide Recognition, RSC Publishing, **2006**.

(251) Floresco, S. B.; West, A. R.; Ash, B.; Moore, H.; Grace, A. A. Afferent Modulation of Dopamine Neuron Firing Differentially Regulates Tonic and Phasic Dopamine Transmission. *Nat. Neurosci.* **2003**, *6*, 968–973.

(252) Wang, Y.; Kotsuchibashi, Y.; Uto, K.; Ebara, M.; Aoyagi, T.; Liu, Y.; Narain, R. pH and Glucose Responsive Nanofibers for the Reversible Capture and Release of Lectins. *Biomater. Sci.* **2015**, *3*, 152–162.

(253) Pattnaik, P. Surface Plasmon Resonance - Applications in Understanding Receptor-Ligand Interaction. *Appl. Biochem. Biotechnol.* **2005**, *126*, 79–92.

(254) Matsui, J.; Akamatsu, K.; Hara, N.; Miyoshi, D.; Nawafune, H.; Tamaki, K.; Sugimoto, N. SPR Sensor Chip for Detection of Small Molecules Using Molecularly Imprinted Polymer with Embedded Gold Nanoparticles. *Anal. Chem.* **2005**, *77*, 4282–4285.

(255) Hansen, K. M.; Thundat, T. Microcantilever Biosensors. *Methods* **2005**, *37*, 57–64.

(256) Anker, J. N.; Hall, W. P.; Lyandres, O.; Shah, N. C.; Zhao, J.; Van Duyne, R. P. Biosensing with Plasmonic Nanosensors. *Nat. Mater.* **2008**, *7*, 442–453.

(257) Azmi, S.; Jiang, K.; Stiles, M.; Thundat, T.; Kaur, K. Detection of Listeria Monocyto Genes with Short Peptide Fragments from Class Ha Bacteriocins as Recognition Elements. *Acs Comb. Sci.* **2015**, *17*, 156–163.

(258) Dowlut, M.; Hall, D. G. An Improved Class of Sugar-Binding Boronic Acids, Soluble and Capable of Complexing Glycosides in Neutral Water. *J. Am. Chem. Soc.* **2006**, *128*, 4226–4227.

(259) Kumbhat, S.; Sharma, K.; Gehlot, R.; Solanki, A.; Joshi, V. Surface Plasmon Resonance Based Immunosensor for Serological Diagnosis of Dengue Virus Infection. *J. Pharm. Biomed. Anal.* **2010**, *52*, 255–259.

(260) Pei, J. H.; Tian, F.; Thundat, T. Glucose Biosensor Based on the Microcantilever. *Anal. Chem.* **2004**, *76*, 292–297.

(261) Matsumoto, A.; Ikeda, S.; Harada, A.; Kataoka, K. Glucose-Responsive Polymer Bearing a Novel Phenylborate Derivative as a Glucose-Sensing Moiety Operating at Physiological pH Conditions. *Biomacromolecules* **2003**, *4*, 1410–1416.

(262) Baldwin, J.; Claridge, T.; Derome, A.; Schofield, C.; Smith, B. B-11 Nmr-Studies of an Aryl Boronic Acid Bound to Chymotrypsin and Subtilisin. *Bioorg. Med. Chem. Lett.* **1991**, *1*, 9–12.

(263) Stewart, A. J.; Hendry, J.; Dennany, L. Whole Blood Electrochemiluminescent Detection of Dopamine. *Anal. Chem.* **2015**, *87*, 11847–11853.

(264) Yang, C.; Jacobs, C. B.; Nguyen, M. D.; Ganesana, M.; Zestos, A. G.; Ivanov, I. N.; Puretzky, A. A.; Rouleau, C. M.; Geohegan, D. B.; Venton, B. J. Carbon Nanotubes Grown on Metal Microelectrodes for the Detection of Dopamine. *Anal. Chem.* **2016**, *88*, 645–652.

(265) Njagi, J.; Chernov, M. M.; Leiter, J. C.; Andreescu, S. Amperometric Detection of Dopamine in Vivo with an Enzyme Based Carbon Fiber Microbiosensor. *Anal. Chem.* **2010**, *82*, 989–996.

(266) Feng, J.-J.; Guo, H.; Li, Y.-F.; Wang, Y.-H.; Chen, W.-Y.; Wang, A.-J. Single Molecular Functionalized Gold Nanoparticles for Hydrogen-Bonding Recognition and Colorimetric Detection of Dopamine with High Sensitivity and Selectivity. *ACS Appl. Mater. Interfaces* **2013**, *5*, 1226–1231.

(267) Po, T.; Steger, G.; Rosenbaum, V.; Kaper, J.; Riesner, D. Double-Stranded Cucumovirus Associated RNA 5: Experimental Analysis of Necrogenic and Non-Necrogenic Variants by Temperature-Gradient Gel Electrophoresis. *Nucleic Acids Res.* **1987**, *15*, 5069–5083.

(268) Myers, R. M.; Maniatis, T.; Lerman, L. S. [31] Detection and Localization of Single Base Changes by Denaturing Gradient Gel Electrophoresis. *Methods Enzymol.* **1987**, *155*, 501–527.

(269) Allison, L. A. *Fundamental Molecular Biology, 2nd Edition*; Wiley, 2011.

(270) High-Resolution DNA Melting Analysis for Simple and Efficient Molecular Diagnostics. *Pharmacogenomics* **2007**, *8*, 597–608.

(271) Herrmann, M. G.; Durtschi, J. D.; Bromley, L. K.; Wittwer, C. T.; Voelkerding, K. V. Amplicon DNA Melting Analysis for Mutation Scanning and Genotyping: Cross-Platform Comparison of Instruments and Dyes. *Clin. Chem.* **2006**, *52*, 494–503.

(272) Shimazaki, Y.; Tanaka, J.; Kohara, Y.; Kamahori, M.; Sakamoto, T. Parallel Evaluation of Melting Temperatures of DNAs in the Arrayed Droplets through the Fluorescence from DNA Intercalators. *Anal. Chem.* **2017**, *89*, 6305–6308.

(273) Wittwer, C. T. High-Resolution DNA Melting Analysis: Advancements and Limitations. *Hum. Mutat.* **2009**, *30*, 857–859.

(274) Rouleau, E.; Lefol, C.; Bourdon, V.; Coulet, F.; Noguchi, T.; Soubrier, F.; Bièche, I.; Olschwang, S.; Sobol, H.; Lidereau, R. Quantitative PCR High-Resolution Melting (qPCR-HRM) Curve Analysis, a New Approach to Simultaneously Screen Point Mutations and Large Rearrangements: Application to MLH1 Germline Mutations in Lynch Syndrome. *Hum. Mutat.* **2009**, *30*, 867–875.

(275) Lyubchenko, Y. L.; Gall, A. A.; Shlyakhtenko, L. S. Visualization of DNA and Protein-DNA Complexes with Atomic Force Microscopy. *Methods Mol. Biol. Clifton NJ* **2014**, *1117*, 367–384.

(276) Shu, W.; Liu, D.; Watari, M.; Riener, C. K.; Strunz, T.; Welland, M. E.; Balasubramanian, S.; McKendry, R. A. DNA Molecular Motor Driven Micromechanical Cantilever Arrays. *J. Am. Chem. Soc.* **2005**, *127*, 17054–17060.

(277) Pud, S.; Chao, S.-H.; Belkin, M.; Verschueren, D.; Huijben, T.; van Engelenburg, C.; Dekker, C.; Aksimentiev, A. Mechanical Trapping of DNA in a Double-Nanopore System. *Nano Lett.* **2016**, *16*, 8021–8028.

(278) Calderon, C. P.; Chen, W.-H.; Lin, K.-J.; Harris, N. C.; Kiang, C.-H. Quantifying DNA Melting Transitions Using Single-Molecule Force Spectroscopy. *J. Phys. Condens. Matter* **2009**, *21*, 034114.

(279) Tooley, M. H. *Electronic Circuits: Fundamentals and Applications*; Elsevier, 2006.

(280) Chaudhari, S.; Chaudhari, K.; Kim, S.; Khan, F.; Lee, J.; Thundat, T. Electrophoresis Assisted Time-of-Flow Mass Spectrometry Using Hollow Nanomechanical Resonators. *Sci. Rep.* **2017**, *7*.

(281) Khan, M. F.; Kim, S.; Lee, D.; Schmid, S.; Boisen, A.; Thundat, T. Nanomechanical Identification of Liquid Reagents in a Microfluidic Channel. *Lab. Chip* **2014**, *14*, 1302–1307.

(282) Wallace, R. B.; Shaffer, J.; Murphy, R. F.; Bonner, J.; Hirose, T.; Itakura, K. Hybridization of Synthetic Oligodeoxyribonucleotides to Phi Chi 174 DNA: The Effect of Single Base Pair Mismatch. *Nucleic Acids Res.* **1979**, *6*, 3543–3557.

(283) Breslauer, K. J.; Frank, R.; Blöcker, H.; Marky, L. A. Predicting DNA Duplex Stability from the Base Sequence. *Proc. Natl. Acad. Sci. U. S. A.* **1986**, *83*, 3746–3750.

(284) SantaLucia, John; Allawi, H. T.; Seneviratne, P. A. Improved Nearest-Neighbor Parameters for Predicting DNA Duplex Stability. *Biochemistry (Mosc.)* **1996**, *35*, 3555–3562.

(285) Manning, G. S. The Persistence Length of DNA Is Reached from the Persistence Length of Its Null Isomer through an Internal Electrostatic Stretching Force. *Biophys. J.* **2006**, *91*, 3607–3616.

(286) Tinland, B.; Pluen, A.; Sturm, J.; Weill, G. Persistence Length of Single-Stranded DNA. *Macromolecules* **1997**, *30*, 5763–5765.

(287) Yakovchuk, P.; Protozanova, E.; Frank-Kamenetskii, M. D. Base-Stacking and Base-Pairing Contributions into Thermal Stability of the DNA Double Helix. *Nucleic Acids Res.* **2006**, *34*, 564–574.

(288) Rychlik, W.; Spencer, W. J.; Rhoads, R. E. Optimization of the Annealing Temperature for DNA Amplification in Vitro. *Nucleic Acids Res.* **1990**, *18*, 6409–6412.

(289) Schildkraut, C.; Lifson, S. Dependence of the Melting Temperature of DNA on Salt Concentration. *Biopolymers* **1965**, *3*, 195–208.

(290) Owczarzy, R.; You, Y.; Moreira, B. G.; Manthey, J. A.; Huang, L.; Behlke, M. A.; Walder, J. A. Effects of Sodium Ions on DNA Duplex Oligomers: Improved Predictions of Melting Temperatures. *Biochemistry (Mosc.)* **2004**, *43*, 3537–3554.

(291) Fuchs, J.; Fiche, J.-B.; Buhot, A.; Calemczuk, R.; Livache, T. Salt Concentration Effects on Equilibrium Melting Curves from DNA Microarrays. *Biophys. J.* **2010**, *99*, 1886–1895.

(292) Baumann, C. G.; Smith, S. B.; Bloomfield, V. A.; Bustamante, C. Ionic Effects on the Elasticity of Single DNA Molecules. *Proc. Natl. Acad. Sci.* **1997**, *94*, 6185–6190.

(293) Fuchs, J.; Dell'Atti, D.; Buhot, A.; Calemczuk, R.; Mascini, M.; Livache, T. Effects of Formamide on the Thermal Stability of DNA Duplexes on Biochips. *Anal. Biochem.* **2010**, *397*, 132–134.

(294) Blake, R. D.; Delcourt, S. G. Thermodynamic Effects of Formamide on DNA Stability. *Nucleic Acids Res.* **1996**, *24*, 2095–2103.

(295) Sadhu, C.; Dutta, S.; Gopinathan, K. P. Influence of Formamide on the Thermal Stability of DNA. *J. Biosci.* **1984**, *6*, 817–821.

(296) Stehr, J.; Hrelescu, C.; Sperling, R. A.; Raschke, G.; Wunderlich, M.; Nichtl, A.; Heindl, D.; Kürzinger, K.; Parak, W. J.; Klar, T. A.; *et al.* Gold NanoStoves for Microsecond DNA Melting Analysis. *Nano Lett.* **2008**, *8*, 619–623.

(297) Knez, K.; Janssen, K. P. F.; Spasic, D.; Declerck, P.; Vanysacker, L.; Denis, C.; Tran, D. T.; Lammertyn, J. Spherical Nucleic Acid Enhanced FO-SPR DNA Melting for Detection of Mutations in Legionella Pneumophila. *Anal. Chem.* **2013**, *85*, 1734–1742.

(298) Stephenson, T.; Li, Z.; Olsen, B.; Mitlin, D. Lithium Ion Battery Applications of Molybdenum Disulfide (MoS2) Nanocomposites. *Energy Environ. Sci.* **2014**, *7*, 209–231.

(299) Gogotsi, Y. What Nano Can Do for Energy Storage. *ACS Nano* **2014**, *8*, 5369–5371.

(300) Grey, C. P.; Tarascon, J. M. Sustainability and in Situ Monitoring in Battery Development. *Nat Mater* **2017**, *16*, 45–56.

(301) Harks, P. P. R. M. L.; Mulder, F. M.; Notten, P. H. L. In Situ Methods for Li-Ion Battery Research: A Review of Recent Developments. *J. Power Sources* **2015**, *288*, 92–105.

(302) Gu, Q.; Kimpton, J. A.; Brand, H. E. A.; Wang, Z.; Chou, S. Solving Key Challenges in Battery Research Using In Situ Synchrotron and Neutron Techniques. *Adv. Energy Mater.* **2017**, 1602831–n/a.

(303) Griffin, J. M.; Forse, A. C.; Tsai, W.-Y.; Taberna, P.-L.; Simon, P.; Grey, C. P. In Situ NMR and Electrochemical Quartz Crystal Microbalance Techniques Reveal the Structure of the Electrical Double Layer in Supercapacitors. *Nat Mater* **2015**, *14*, 812–819.

(304) Wang, L.; Liu, D.; Yang, S.; Tian, X.; Zhang, G.; Wang, W.; Wang, E.; Xu, Z.; Bai, X. Exotic Reaction Front Migration and Stage Structure in Lithiated Silicon Nanowires. *ACS Nano* **2014**, *8*, 8249–8254.

(305) Huang, J. Y.; Zhong, L.; Wang, C. M.; Sullivan, J. P.; Xu, W.; Zhang, L. Q.; Mao, S. X.; Hudak, N. S.; Liu, X. H.; Subramanian, A.; *et al.* In Situ Observation of the Electrochemical Lithiation of a Single SnO2 Nanowire Electrode. *Science* **2010**, *330*, 1515–1520.

(306) BalkeN; JesseS; Morozovska, A. N.; EliseevE; Chung, D. W.; KimY; AdamczykL; Garcia, R. E.; DudneyN; Kalinin, S. V. Nanoscale Mapping of Ion Diffusion in a Lithium-Ion Battery Cathode. *Nat Nano* **2010**, *5*, 749–754.

(307) Lacey, S. D.; Wan, J.; Cresce, A.; Russell, S. M.; Dai, J.; Bao, W.; Xu, K.; Hu, L. Atomic Force Microscopy Studies on Molybdenum Disulfide Flakes as Sodium-Ion Anodes. *Nano Lett.* **2015**, *15*, 1018–1024.

Appendix

Appendix 1 Peptide Synthesis

Materials and Methods

Materials

1-hydroxybenzotriazole (HOBt), HCTU and the Fmoc amino acids were purchased from NovaBiochem (San Diego, CA) while CyQUANT and FITC dyes were obtained from Invitrogen (Eugene, Oregon, USA). Amino-PEG500 cellulose membrane derivatized with a polyethylene (PEG) purchased from (Intavis AG, Germany). N,N′-Diisopropylcarbodiimide (DIC), N,Ndimethylformamide (DMF), 1-Ethyl-3-(3-dimethylaminopropyl)-carbodiimide) (EDC), Nhydroxysuccinimide (NHS), N-methyl morpholine (NMM), trifluoroacetic acid (TFA), dimethyl sulfoxide (DMSO), piperidine and all other reagents were purchased from Sigma-Aldrich. All reagents and solvents were purchased analytical grade and used as received with no further purification. All experiments with bacteria were performed in biosafety level II cabinet.

Peptide Array Synthesis

Synthesis of peptides on PEG500 derivatised cellulose membrane was started by attaching first β-alanine residue (linker) to the cellulose membrane and subsequently peptides synthesized from the C-terminus. Fmoc protected amino acids (0.25 mM/mL) activated

with HOBt and DIC were spotted on the membrane in 60 nL aliquots per spot by a robotic syringe, yielding a peptide loading of 0.4 μmol/cm2. After coupling of the Fmoc amino acid, the membrane was removed from the platform of robotic system and treated with acetic anhydride (2%) to cap any free remaining amino groups. Deprotection of Fmoc of coupled amino acid was done by 20% piperidine in DMF. After deprotection, membrane was washed with DMF and IPA, air-dried and carefully repositioned on the robotic system to repeat the coupling cycles in order to complete the peptide sequence. At the end, all peptides were N-terminally acetylated. The final removal of side chain protecting groups was performed by treating the membrane with a cocktail of reagents, comprised of TFA (15mL), DCM (15 mL), triisopropylsilane (0.9 mL), and water (0.6 mL), for about 3 h. After extensive washing with DCM, DMF, and ethanol, the membrane was dried with cold air. Next, the cyclization of cysteine containing peptides was performed to form the disulfide bond. The membrane was incubated with 20% DMSO in water for 24 h at 4 °C, and finally overnight at room temperature. Subsequently, the membrane was washed with ethanol (3 ×3 min), dried, and stored in a sealed bag at -20 °C until use.

Peptide Array-Cell Binding Assay

Overnight grown bacterial culture was washed one time with PBS (50 mM Phosphate Buffer Saline) and diluted to 0.5 O.D utilizing the same buffer. Bacteria were labeled by taking diluted culture (100 μL, 0.5 O.D) and incubating with CyQUANT dye (40 μL, 1X) in dark and at room temperature for two hours. The cells were washed with PBS two times to remove free dye and re-suspended into 10 mL of same buffer. Before performing cell binding assay, peptide array membrane was incubated for 1 min in ethanol to avoid any

kind of hydrophobic aggregation, washed with PBS (2 times for 5 min each) and incubated again in PBS for 30 min. The peptide array membrane was incubated with the labeled bacterial cells (10 mL, 0.05 O.D) for 2 h in the dark color box with gentle shaking condition at room temperature. Subsequently, the peptide array membrane was washed extensively (3x or more with PBS, each washing 10 min) to remove loosely bound or unbound cells to the membrane. The net fluorescence intensity of each peptide spot was quantified using Kodak Molecular Imaging Software Version 4.0. An external standard peptide was used to calibrate the fluorescence intensity between scans performed on the same day and on different days. The results are presented as average fluorescence intensity of two duplicate peptide spots, two scans, and two different experiments. Membrane was regenerated after each cell-binding experiment. For membrane regeneration, the bound cells were removed by first washing with ethanol for 5 min, followed by treatment with 0.1 N HCl for 20 min. The peptide array membrane was then washed with DMF (4 × 20 min), ethanol (3 × 3 min), and finally dried in air. Each cell-binding experiment was repeated twice for same bacterial species.

Appendix 2 Characterization of HSA

CD Spectropolarimetery: The CD spectra were measured on an OLIS DSM 17 Circular dichroism instrument (OLIS Inc., Bogart, GA). Quartz cell of 0.02 cm path length was used to contain sample. The spectra were recorded in the far-UV region with wavelength between195 and 275 nm. The spectrum was recorded with five scan accumulations. The data was analyzed using CD pro software.

Attenuated total internal reflection –Infrared Spectroscopy (ATR-IR): A NEXUS 670 ATR-IR equipped with ZnSe crystal (Thermo Nicolet, Madison, WI, USA) was used. IR was equipped with mercury-cadmium-telluride detector cooled using liquid nitrogen. ATR-IR for the HSA was taken after putting the 2ml of 0.2 mg/ml sample on the ZnSe crystal and dried under nitrogen. The resolution was 4 cm-1 in total of 200 scans.

Dynamic Light scattering (DLS): DLS experiments were conducted on commercial apparatus ALV/CGS-3 compact Goniometer system (ALV, GmbH, Germany) at an angle of 90°. JDS Uniphase 22mW He-Ne laser, functioning at wavelength 632.8 nm was equipped with aALV-5000/EPP multi-tau digital correlator with channels. ALV/LSE-5003 light scattering electronics unit was used for stepper motor drive and for the limit switch control. Autocorrelation functions were collected 3 times for each sample solution and were examined by the CONTIN routine using the software provided by the vendor. Toluene was used as standard corrector for temperature and scattering.

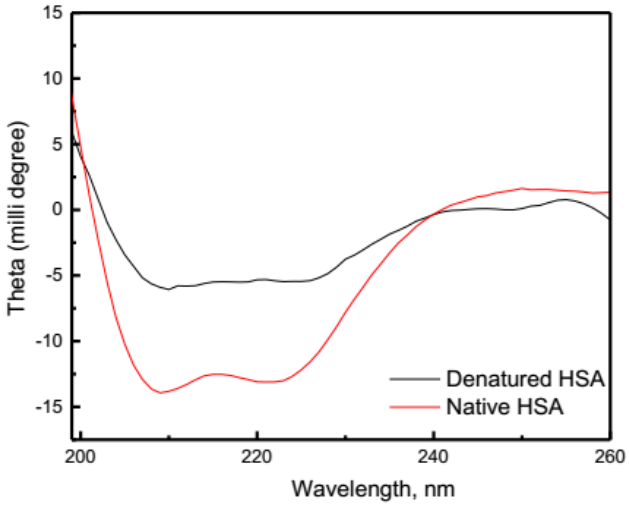

Figure A1. CD spectra of native and denatured HSA

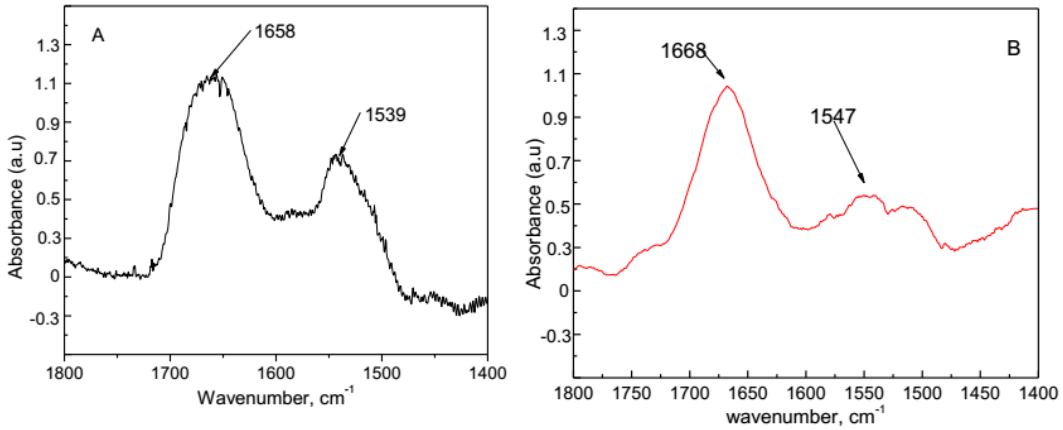

Figure A2. ATR-IR spectra of A) native HSA and B) denatured HSA.

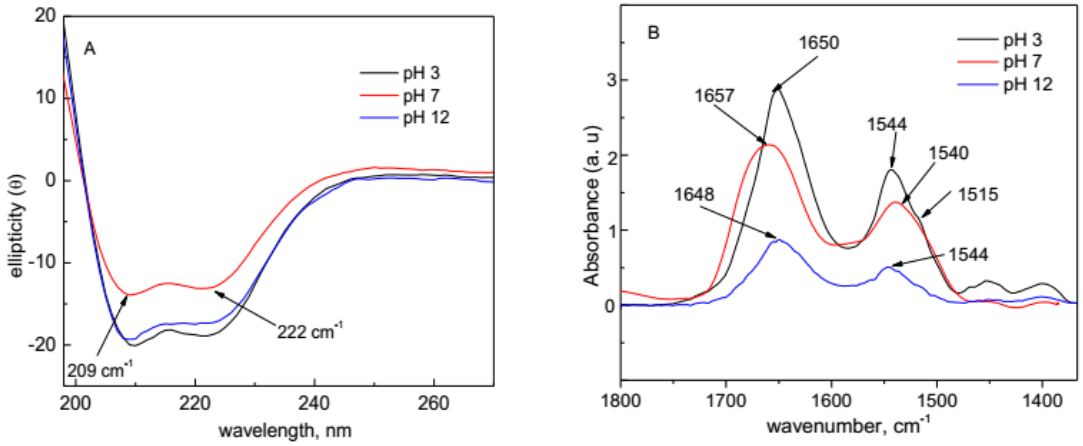

Figure A3. A) CD spectra of native HSA at pH 3, 7 and 12. B) ATR-IR spectra of native HSA atpH 3, 7 and 12.

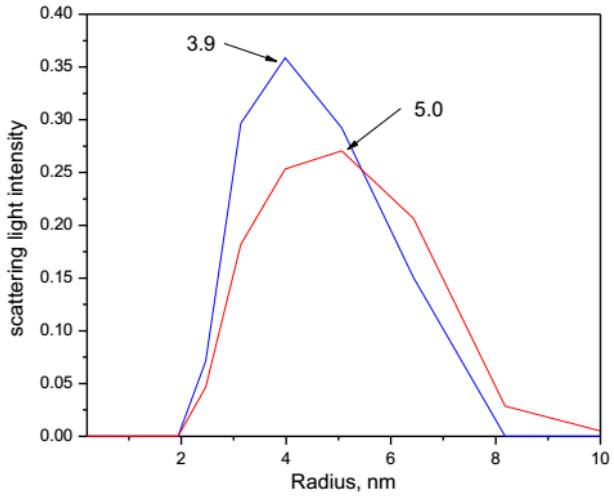

Figure A4. DLS spectra of native (blue) and denatured (red) HSA samples.